INSIGHTS INTO CORRELATED ELECTRON SYSTEMS FROM FIRST-PRINCIPLES QUANTUM MONTE CARLO

BY

BRIAN M. BUSEMEYER

DISSERTATION

Submitted in partial fulfillment of the requirements
for the degree of Doctor of Philosophy in Physics
in the Graduate College of the
University of Illinois at Urbana-Champaign, 2019

Urbana, Illinois

Doctoral Committee:

Professor Anthony J. Leggett, Chair
Assistant Professor Lucas K. Wagner, Director of Research
Assistant Professor Gregory MacDougall
Professor Harley T. Johnson

Abstract

Accurate first-principles calculations can provide valuable predictions for material-specific properties as well as simplified models for interpreting materials' behavior. However, the level of accuracy required is difficult to reach in systems where it is important to properly account for electron correlations. I report several benchmarks establishing that variational Monte Carlo (VMC) and fixed-node diffusion Monte Carlo (FN-DMC) are efficient enough to compute properties of realistic systems while significantly improving on the accuracy of more commonly-used first-principles approaches. For chemical reactions, FN-DMC can provide reaction barrier estimates that have reached "chemical accuracy," the accuracy threshold to predict room-temperature chemistry measurements. For the iron-based superconductor, FeSe, I report on quantum Monte Carlo calculations that accurately reproduce the structural properties, including the lattice constants and the equation-of-state. In FeSe, I also found a coupling between the structure, spin texture, and orbital occupation in the system that may be relevant to explain some of the unique properties of that system. To establish its predictive capabilities, I also utilize FN-DMC to make a prediction for the singlet-triplet gap of $MgTi_2O_4$, a spinel system relevant to the search for spin liquids. We found that the gap was larger than previous experiments have considered, and may explain why the singlet-triplet gap has not yet been observed in that system.

In addition to calculating material properties, I also leverage FN-DMC to characterize systems using simple models. In FeSe, starting from the assumption that Hund's coupling is important, I found a simple model that was able to explain how the electronic properties varied with spin texture. Using a downfolding procedure combined with FN-DMC and tools from data science, I analyzed the importance of a wide class of effective model terms in describing an Fe-Se diatomic molecule. The study determined that Hund's coupling was the most important interaction in this system, and quantified its importance relative to other terms. I also developed a new strategy for efficiently discovering low-energy states in the Hilbert space, an important input for developing low-energy effective models. I applied this strategy in H_2 in two geometries where a tight-binding model is accurate and where it breaks down, and I quantify the importance of interactions in the effective model. The results establish the accuracy of FN-DMC for correlated electron systems and

develop strategies for determining accurate effective lattice models from first-principles quantum Monte Carlo.

For my parents.

Acknowledgements

I would like to thank S. Lance Cooper and many others in the University of Illinois Physics Department for creating such a friendly, healthy research atmosphere here in Illinois. Their efforts helped make the environment at University of Illinois so collaborative, which is why I have come to know so many excellent people here.

I would like to thank the students and postdocs in our group from whom I have come to for help and learned many important things from. In particular, Shivesh Pathak, Kiel Williams, Huihuo Zheng, Raymond Clay, Awadhesh Narayan, Katharina Doblhoff-Dier, Hitesh Changlani, all were invaluable resources, of whom I was never afraid to ask "stupid questions" and learn smart ways of understanding them.

I also should thank the many classmates with who I have shared a lot of laughs and from who I learned a lot of physics outside my field. I especially want to the thank Matt Zhang. His talent for problem solving and unbridled optimism can conquer anything, and I learned not to be afraid to tackle unusual problems using what I know.

I want to thank my office mate and good friend, Paul Yang. From fundamentals of QMC to crackpot ideas for new methods, he is the ultimate resource for figuring it all out. His talent for research was also an inspiration, and I can tell we will be colleagues and friends well into the future.

I'd like to thank professor David Ceperley and my Ph.D. advisor, Lucas Wagner. David's knowledge and intuition have greatly accelerated my understanding of numerical methods and set an example for using them to accomplish great deeds. It'd be difficult to list everything I have learned from Lucas, so I will just say that Lucas has taught me what it means to be a good researcher and good mentor. His enthusiasm for research, expansive knowledge of science, methodical approach to solving problems, and effective ways of presenting science as fun and engaging are all lofty goals for me to reach.

I have to thank my parents, who taught me to be creative, engage in challenge problems, and be confident in my abilities. They are inspiring role models both as parents and scientists.

Most importantly, my amazing wife, Lily. Whenever things are difficult, her smile and her kindness washed all troubles away. She restores balance in my life and makes my life whole. She gives me the energy

and determination to be who I want to be. Her presence is an inseparable part of this work.

Finally, thanks to all my funding sources. I thank the NSF Graduate Research Fellowship for funding. This research is part of the Blue Waters sustained-petascale computing project, which is supported by the National Science Foundation (awards OCI-0725070 and ACI-1238993) and the state of Illinois. Blue Waters is a joint effort of the University of Illinois at Urbana-Champaign and its National Center for Supercomputing Applications. Computational resources were also provided by the Illinois Campus Cluster program and the Department of Energy INCITE program. I also gratefully acknowledge the Simons Foundation for funding.

Table of Contents

List of Tables . . . . . **ix**

List of Figures . . . . . **x**

List of abbreviations . . . . . **xv**

Common variable definitions . . . . . **xvi**

Chapter 1 Introduction **1**
1.1 First-principles calculations and materials design 1
1.2 Effective models from first-principles calculations 2
1.3 Outline of the dissertation 4
1.4 Summary of accomplishments 5

Chapter 2 Current state-of-the-art in first-principles methods **7**
2.1 Wave-function methods 7
2.1.1 Hartree-Fock and configuration interaction 7
2.1.2 Coupled cluster 10
2.1.3 Density matrix renormalization group (DMRG) and extensions 11
2.1.4 Variational Monte Carlo 12
2.1.5 Diffusion Monte Carlo 17
2.1.6 Auxiliary-field quantum Monte Carlo 26
2.2 Density functional theory 29
2.2.1 Hohenberg-Kohn existence theorem and Kohn-Sham density functional theory 29
2.2.2 The Kohn-Sham Hamiltonian: its usage and its theoretical meaning 31
2.2.3 Example applications and current challenges 32
2.3 Diagrammatic methods 33
2.3.1 GW approximation 34
2.3.2 Dynamical mean field theory 36
2.4 Pseudopotential approximation 39
2.5 Supplemental information: Hartree-Fock equations 40

Chapter 3 State-of-the-art in downfolding the first-principles Hamiltonian **42**
3.1 Constrained-RPA 43
3.2 Density matrix downfolding. 44
3.2.1 Proof of principles 45
3.2.2 Fitting energy functions that are linear in density-matrix elements 46
3.2.3 Examples of applications and current challenges 48

Chapter 4 Connecting methods into a calculation workflow **49**

Chapter 5 Reaction barriers for non-hydrogen transfer reactions . . . 50
5.1 Reaction barriers from first-principles . . . 50
5.2 Details of the calculations . . . 51
5.3 Results . . . 51
5.4 When are fixed-node errors large? . . . 55
5.5 Conclusions from barrier height study . . . 58

Chapter 6 Accurate FN-DMC calculations of FeSe . . . 60
6.1 Introduction to FeSe . . . 61
6.2 Details of the calculations . . . 62
6.3 Results . . . 63
6.3.1 Trial wave functions and ground state . . . 63
6.3.2 Crystal structure . . . 66
6.3.3 Interaction of structure and magnetism . . . 68
6.3.4 Optical excitations and magnetism . . . 71
6.3.5 Interaction of charge and orbitals with magnetism . . . 73
6.3.6 Hund's coupling and the connection to spin-charge coupling . . . 74
6.4 Conclusion for bulk-FeSe . . . 76
6.5 Supplemental information . . . 77
6.5.1 Convergence and validation . . . 77

Chapter 7 Low-energy description of FeSe molecule from first-principles . . . 82
7.1 Downfolding procedure . . . 83
7.2 Results . . . 84

Chapter 8 Prediction of the singlet-triplet gap of $MgTi_2O_4$ . . . 86
8.1 Nature of the ground state of $MgTi_2O_4$ . . . 86
8.2 Calculation details . . . 87
8.3 Results . . . 89
8.4 Conclusion for $MgTi_2O_4$ . . . 91
8.5 Supplemental information . . . 91

Chapter 9 Algorithm for the discovery of low-energy states . . . 93
9.1 Approaches to finding low-energy states . . . 93
9.2 Modifying the VMC objective function . . . 95
9.3 Application to H_2 . . . 95
9.3.1 H_2 with equilibrium bond length . . . 96
9.3.2 H_2 with stretched bond length . . . 96
9.3.3 Conclusions from constrained VMC study . . . 97

Chapter 10 Progress towards a first-principles understanding of correlated electron materials . . . 100

Chapter 11 References . . . 102

List of Tables

5.1 The non-hydrogen-transfer reactions [1] and their corresponding IDs. The transition states are labeled as TS01 to TS19, following Ref [2]. When + separates the reactants or products, the energies of each atom or molecule are calculated in separate DFT, HF, or DMC calculations, whereas when ... separates the reactants or products, all the reactants or all the products are simulated in the same calculation together although they are actually seperated in physical space. 52

6.1 FeSe optimal structural parameters with different computational methods. DFT calculations have been performed with the software package QUANTUMESPRESSO [3] using a 10x10x10 k-points mesh, an energy cutoff of 75 Ry and norm conserving pseudopotentials for both Fe and Se. The variational Monte Carlo VMC(opt) results are obtained at Gamma point only with the 16 f.u. FeSe supercell containing 32 atoms. 67

9.1 Parameters, goodness of fit, and first three eigenvalues relative to the ground state for all calculations presented in this chapter. Energies are in units of Ha. 96

List of Figures

2.1 A pedagogical example of how the off-diagonal of the 1-RDM characterizes the system. Consider if $|\phi_i\rangle$ orbitals represent s orbitals on each H atom, and the Hamiltonian for two H_2 molecules separated by a large distance is diagonalized in this basis. The ground state is an antisymmetrized product of two bonding orbitals: $|ab\rangle = (|a\rangle + |b\rangle)/\sqrt{2}$ and $|bc\rangle = (|c\rangle + |d\rangle)/\sqrt{2}$. In this case $\rho^{(1)}_{\uparrow,\mathrm{a,b}} = 1/2$ and $\rho^{(1)}_{\uparrow,\mathrm{a,c}} = 0$, characterizing the bonding in the system. This is because the up electron can be removed from (a) and placed into (b) holding all else fixed (not time-evolving the system, for example). There is no probability for the right H_2 to have three electrons, and so removing an electron from (a) and placing it on (c) has no amplitude: $\rho^{(1)}_{\uparrow,\mathrm{a,c}} = 0$. 15

2.2 Spin densities of FeSe magnetic spin textures at ambient pressure, (a) collinear, (b) collinear, 1 flip, (c) bicollinear, and (d) checkerboard. Four unit cells of a single iron layer are shown, divided by black lines. "Collinear, 1 flip" refers to flipping the spin of one iron per unit cell in the collinear configuration. Since four unit cells are shown above, there are four "flipped" iron moments shown in this plot. The larger red Se atoms lie above and below the plane and show significantly smaller spin density. Irons are smaller and blue, and lie within larger concentration of spin. The two colors of the isosurfaces denote density of up and down. . . . 24

2.3 Feynman diagrams representing Hedin's equations (2.56–2.60). Image from Ref. [4]. 35

5.1 The DMC total energy relative to the lowest energy among the three functionals. The error bars are statistical errors from DMC. 53

5.2 The error of forward and reverse reaction barrier heights, denoted by v_f and v_r, versus reaction ID as defined in Table 5.1. The error bars are insignificant and therefore neglected. The value of the missing point, v_r of HF for Reaction 1, is 41.14 kcal/mol. 54

5.3 (Top) The box-and-whisker plot of the barrier-height errors for each method. Each box ends at first (Q_1) and third (Q_3) quantiles. The horizontal line in each box represents the median. The whiskers extend to the farthest points within 1.5 times the difference between Q_1 and Q_3. Every point outside of this range is represented by a diamond and labeled by an ID number as defined in Table 5.1 followed by a character, r or f, which represents a forward or reverse reaction. (Bottom) The bar chart of the mean absolute error for each method. The DMC error bars denote statistical errors. 56

5.4 Approximate nodal error, measured by the energy difference between DMC(PBE0) and DMC(HF) plotted against the HOMO-LUMO gap, computed by PBE0. 57

5.5 Approximate nodal error, measured by the energy difference between DMC(PBE0) and DMC(HF) plotted against the energy difference between VMC(PBE0) and VMC(HF). 58

6.1 Spin densities of magnetic orderings at ambient pressure, (a) collinear, (b) collinear, 1 flip, (c) bicollinear, and (d) checkerboard. Four unit cells of a single iron layer are shown, divided by black lines. "Collinear, 1 flip" refers to flipping the spin of one iron per unit cell in the collinear configuration. Since four unit cells are shown above, there are four "flipped" iron moments shown in this plot. The larger red Se atoms lie above and below the plane and show significantly smaller spin density. Irons are smaller and blue, and lie within larger concentration of spin. The two colors of the isosurfaces denote density of up and down. . . . 62
6.2 Selection of experimental measurements from Margadonna *et al.* [5], Kumar *et al.* [6], and Millican *et al.* [7] of the selenium height, z_{Se}, as a function of pressure, along with corresponding QMC (left) and DFT (right) predictions. QMC(opt) refers to calculations done with a fully optimized Slater determinant, which was VMC for the paramagnetic state (open circles), and DMC for the collinear state (green diamonds). The fully-optimized QMC calculation is done at Γ-point only, but at a 16-f.u. supercell. The DMC(PBE0) points are at 8 f.u., but are twist averaged over 8 twist values, therefore should have compareable finite-size errors. More discussion of this comparison is available in the appendix. Accordingly, the ambient pressure DMC(PBE0) calculation agrees nearly within error bars with the fully optimized DMC(opt) calculation. 64
6.3 Pressure as a function of volume, computed through an equation-of-state fit to DMC(PBE0) data and from experiments by Margadonna *et al.* [5], Kumar *et al.* [6], and Millican *et al.* [7]. All points along the solid line come from the equation-of-state, and markers are added purely to distinguish the magnetic state. For the volumes considered here, regardless of spin ordering, $P(V)$ falls within the experimental spread. Inset displays corresponding bulk modulus in units of GPa for PBE0, DMC(PBE0), and the experiments considered. The bulk modulus is strongly coupled to the magnetic state, and for the collinear state, DMC(PBE0) demonstrates excellent agreement with all the experiments considered. Bulk moduli computed from PBE are between 7 and 9 GPa, and are much more insensitive to the magnetic ordering (see Supplemental Materials for tabulated values). Lattice constants used were those of Kumar[6]. 65
6.4 DMC(PBE0) energies as a function of volume and selenium height z_{Se} for three of the magnetic orderings. The solid vertical line represents the minimum of the collinear magnetic ordering, while the dashed vertical line represent the predicted crossing of the bicollinear and collinear energies. These two points converge as the pressure is increased, as shown on the far right. . 69
6.5 For each calculation (QMC, PBE, and PBE0): (Right) Total energies for 8 f.u. cell for various magnetic orderings, as a function of volume, choosing experimental [5] values of z_{Se}. (Left) Same as right, but choosing optimized values of z_{Se}. For the top QMC plots, energies are referenced to the collinear energy at around 77 Å^3. The DFT calculations are referenced to the z_{Se} minimum energy for that type of calculation. The DMC paramagnetic energies are $\sim$ 0.85 eV/f.u. higher than the reference collinear energy. 70
6.6 Gap as a function of twisted boundary conditions calculated within DMC(PBE0). For the stripe-like magnetic states, the gap is zero within statistical error. The unit cell is a 2×2 supercell, expanded in the x-y plane, shown as one of the four outlined boxes in each of the spin densities of Fig. 6.1. [Note: this figure has been updated from the published version to correct an mistake in the units of the gap.] 72

6.7 **(a)** Charge variance, in units of number of electrons squared for different magnetic orderings in the majority and minority spin channel, as a function of cell volume, illustrating that the minority spin channel is more mobile, and additionally that the checkerboard ordering's electrons are more constrained to a given iron site. **(b)** Magnetic moments inside each iron's Voronoi polyhedron. **(c)** Magnitude of on-site correlations, measured by $|\mathrm{Cov}(n^\uparrow, n^\downarrow)|/[\mathrm{Var}(n^\uparrow)\mathrm{Var}(n^\downarrow)]^{1/2}$. **(d)** Single-particle orbital occupations of the iron d-states, measured by the on-diagonal terms of the 1-RDM. Note checkerboard's charge density points mostly out of the iron plane, while the other orderings point mostly within the plane. **(e)** Hybridization of different orderings, as measured by an average of the off-diagonal elements of the 1-RDM, broken down by interactions between antiparallel (Antipar.) aligned irons and parallel (Par.). 72

6.8 Diagrams depicting the occupations of the d-orbitals of a reference iron, one of its neighbors with parallel net magnetic moment, and another neighbor with antiparallel magnetic moment. The minority channel is spin down for the top two, and is spin up for the last. The minority electron on the reference atom is most likely to hop to a neighbor, for example, the greyed out down electron on $d_{z^2-r^2}$. It may easily hop to its parallel neighbor, which may fill its $d_{x^2-y^2}$ orbital as suggested by the grey box. It may not hop to any of the orbitals of the antiparallel neighbor, since the down spin channel is filled. Any hopping from the reference iron to its antiparallel neighbor must occur in the spin-up channel, which consequently violates Hund's rule for the reference iron. 75

6.9 Convergence of DFT and DMC parameters. Axes labeled by $E - E_{\mathrm{min}}$ are energies relative to the minimum energy of the points in the subfigure. (a) Convergence of k-point grid for DFT calculations for the 8 f.u. cell. A $4 \times 4 \times 4$ grid was used for all these calculations. (b) Convergence of DMC(PBE0) basis set parameters for the 8 f.u. cell, at zero pressure. "Fe basis exp" and "Se basis exp" refer to the value of the smallest exponent in the basis. Values of around 0.26 and 0.2 were used for Fe and Se respectively. While in the latter case the total energy is decreasing, the energy differences are stable. (c) Finite size extrapolation for DMC(PBE0) at the largest and smallest volumes considered, twist averaging over 8 boundary conditions. Energy is relative to the collinear energy for each size. The two checkerboard lines reflect a finite size extrapolation in the $\hat{z}$ direction (upper line) and extrapolation in the x-y plane (lower line). The full extrapolation will likely be near the center of the two line endpoints. (d) Time step extrapolation for the DMC(PBE0) at 8 f.u. at the largest and smallest volumes considered. A value of 0.01 a.u. was adopted for all DMC(PBE0) calculations. (e) Finite size extrapolation for the DMC(opt) calculations, with periodic (PBC) and antiperiodic (APBC) boundary conditions, along with their average (Avg.). These benchmark calculations are performed in the paramagnetic phase and energies are corrected for one-body and two-body finite size errors. (f) Extrapolation of the lattice spacing used for the laplacian discretization for the LR-DMC, i.e. DMC(opt), calculations. These benchmark calculations are performed in the collinear phase. A value of 0.125 a.u. was adopted for all calculations. . 78

6.10 DMC optimization of exchange correlation functional for the DFT calculations. The exchange-correlation function depends on w as $E_{\mathrm{xc}}^{w}[n] = wE_{\mathrm{x}}^{\mathrm{HF}}[n] + (1-w)E_{\mathrm{x}}^{\mathrm{PBE}}[n] + E_{\mathrm{c}}^{\mathrm{PBE}}[n]$. Lines are a cubic spline interpolation as a guide to the eye. 79

6.11 Finite size extrapolation near $z_{\mathrm{Se}} = 1.42$ of the energy differences between collinear and checkerboard magnetic ordering for DMC(opt) (thick outline) an DMC(PBE0) (thin outline). DMC(opt) data points are averaged over periodic and fully antiperiodic boundary conditions, while DMC(PBE0) is averaged over 8 twists. The extrapolations are in agreement within statistical error. 79

7.1 (Left) Parameter values for each fit generated in the MP algorithm, labeled at the step where they are included in the model. A zero value indicates that parameter is not yet added to the model. The sign of J is consistent with Hund's rules, and the signs of $t_{\sigma,d}$ and $t_{\sigma,s}$ are consistent with Se being located in positive z with respect to Fe. (Right) RMS error of each model generated by MP as the algorithm includes parameters. The RMS error of the largest model considered was 0.61 eV. 83

8.1 Spin density contour plot for the spin states considered in this work. Up and down spin densities are represented as blue and red. Orange atoms with spin are Ti atoms, of the spinless atoms, the smaller brown atoms are O, and the white atoms are Mg. Bonds are drawn between dimerized Ti atoms, and bonds that exit the unit cell have no Ti atom on the end outside the cell, which is drawn with black lines. The diffusion Monte Carlo energies of the dimer and triplet state determine the model, and the "interdimer" states are used to test the accuracy of the model. 89

8.2 Energies of each state relative to the dimer state of Fig. 8.1 according to DMC and PBE0 as well as models fit to DMC and PBE0 data. The triplet energy difference is sufficient to fit the parameter in (8.1), with $J = 350(50)$ meV from DMC, for example. This makes the singlet-triplet gap 350(50) meV for this system. The interdimer states are predictions from the independent dimer model (8.1), and are used to test the predictability of the model. Because PBE0 reproduces the energy differences for the unpolarized, triplet, and interdimer state, PBE0 energies should be sufficient for interdimer 2–5, which are only used to probe the relevance of interdimer interactions. Due to computational constraints we did not also provide DMC energies for interdimer 2–5. The model predictions for the interdimer states agree quite well with (8.1), suggesting that the independent-dimer model is an accurate effective model for the spins in this system. 90

8.3 Spin density (top row) and charge density (ρ) relative to the unpolarized charge density $\rho_{\text{unpolarized}}$ (bottom row) through Ti pairs and their intermediate O. Dimer signifies the Ti atoms in the center form a nearest neighbor dimer pair in the structure. Inter-dimer signifies that the Ti atoms are nearest neighbors in the x-y plane. The dimer bond shows spin density typical for atoms interacting through superexchange, as well as an increase in hybridization between Ti and O within the dimer as compared to the unpolarized state. The interdimer bond shows no such signals of superexchange, in agreement with the model results. 91

8.4 (left) Energy vs. Brillouin zone sampling for the PBE0 calculations. The energies are shown relative to the largest number of kpoints ($6 \times 6 \times 6$), so that the left point is zero by definition. The error in the total energies is converged to the micro-eV scale, which is well below the scale of other errors in our work. (right) Timestep extrapolation for the DMC calculations was performed with two points at 0.01 and 0.02 timestep. These points were extrapolated to zero timestep. The timestep error in the energy difference is well within our statistical error. 92

9.1 PBE0 band structure of FeSe with the collinear spin texture. The bands feature an unphysical gap of over 2 eV, consistent with other hybrid functional calculations [8]. 94

9.2 States sampled by the constrained VMC algorithm by adjusting the hopping amplitude in H_2. Each point represents a VMC calculation with different λ specified by the color and marker. (a) By increasing λ, the VMC optimization shifts from the bonding (lower right) to antibonding (upper left) state. The t parameter of a tight-binding model, (9.4) with $U = 0$, is equal to the slope of the line. The state begins to shift when $\lambda \approx t = -0.296$ Ha, as this is the energy scale of changing the hopping amplitude. The R^2 of the fit is 0.996, signifying that the tight-binding model is a good fit for this system. (b) The same data, but plotted with respect to both descriptors of the Hubbard model. The projection on the back (matching (a)) and bottom planes are shown in grey. Although the plane traces a path in three dimensions, the plot is very linear with $\langle \hat{c}_1^\dagger \hat{c}_2 + \hat{c}_2^\dagger \hat{c}_1 \rangle$, meaning that a t-only model is sufficient for this system. The state in the middle of the curve nearly minimizes the expected double occupation on the sites. 97

9.3 Similar to Fig 9.2, states sampled by the constrained VMC algorithm by adjusting the hopping amplitude in stretched H_2. Each point represents a VMC calculation with different λ specified by the color and marker. (a) By increasing λ, the VMC optimization shifts from the ground to antibonding (upper left) state. Because the ground state is no longer the bonding state, decreasing λ moves the state from ground to bonding. The tight-binding fit (the solid line) is no longer a good model for the system, although with $R^2 = 0.864$, it captures most of the energy variation. The error of the fit is proportional to the double-occupation of the state that is sampled, which is why the error has positive curvature. (b) The same data, but plotted with respect to both descriptors of the Hubbard model. The projection on the back (matching (a)) and bottom planes are shown in grey. The energy scale is set to the same as Fig. 9.2 to emphasize the rapid decrease of t—the slope of the line in the $\langle \hat{c}_1^\dagger \hat{c}_2 + \hat{c}_2^\dagger \hat{c}_1 \rangle$ direction, which decreases exponentially with H–H distance. The Hubbard model fits these points with $R^2 \approx 0.999$, so the points all lie in a plane with slopes of non-negligible magnitude in two directions. 98

List of abbreviations

HF	Hartree-Fock
FCI	Full-configuration interaction
DFT	Density Functional Theory
QMC	Quantum Monte Carlo
VMC	Variational Monte Carlo
DMC	Diffusion Monte Carlo
AFQMC	Auxiliary field quantum Monte Carlo
FCIQMC	Full configuration interaction quantum Monte Carlo
RPA	Random Phase Approximation
DMFT	Dynamic mean field theory

Common variable definitions

N	number of electrons in the simulation.
M	number of time steps in projector Monte Carlo.
τ	imaginary time, it.
$\mathbf{r}$	a single electron coordinate.
$\mathbf{R}$	configuration of N electrons $\{\mathbf{r}_i\}_{i=1}^{N}$.
$\hat{H}$	first-principles Hamiltonian (1.1).
$\hat{T}$	kinetic energy operator, $-\frac{1}{2}\sum_{i=1}^{N}\nabla_i^2$ in atomic units.
$\hat{V}$	total potential energy operator, external and electron-electron interaction.
$\hat{H}_{\text{eff}}$	an effective Hamiltonian.
$V_{\text{eff}}(\mathbf{r})$	an effective external potential for a noninteracting model.
$\lvert\Psi_0\rangle$	exact ground state of $\hat{H}$.
$\lvert\Psi_{\text{T}}\rangle$	a trial function, usually Slater-Jastrow type.
$\lvert\Psi_{\text{FN}}\rangle$	the fixed-node DMC wave function.

Chapter 1

Introduction

1.1 First-principles calculations and materials design

The history of superconductivity is the perfect example of the unpredictable nature of electrons in materials. Superconductivity was first observed in the early 1900's, when conductivity was explained in classical terms. To test the notion that electron conduction was driven by classical thermal fluctuations, Onnes *et al.* developed new cooling techniques which enabled the first probe of mercury at liquid helium temperatures (0.3 K) [9]. Rather than seeing the resistivity increase, the resistivity suddenly dropped precisely to zero—something impossible to understand from the standpoint of classical mechanics. 56 years later, the theory of BCS superconductivity [10] was able to explain the phenomenon in mercury and many other superconductors using concepts from quantum mechanics. Early trends in superconductor discoveries suggested they were metals with high symmetry and no magnetism, and it was proposed that no superconductor would exist above roughly 30 K [11, 12]. The discoveries of cuprate superconductors [13] and iron-based superconductors [14, 15] (among others) would all break these trends, and many would break the proposed 30 K limit. The superconducting phases of these unconventional superconductors arise at or near conditions where the material is magnetic, often are doped from materials that are insulators or poor metals, and have quasi-two-dimensional structures. Like the first observation of superconductivity, progress in these unconventional superconductors has been in advance of theoretical predictions [16].

In these cases, a better understanding of how quantum mechanical properties of electrons drive materials' properties should accelerate the discovery of useful materials by enabling theory to guide experiment. Indeed, a quantum-mechanical theory of interacting electrons which is universally applicable to the low-temperature properties of materials *is already known.* It is the first-principles many-body Schrödinger equation [17]:

$$\hat{H} = \hat{T} + \hat{V} = \frac{1}{2}\sum_i \nabla_i^2 + \sum_{ij} \frac{1}{|\mathbf{r}_i - \mathbf{r}_j|} + \sum_{iI} V_{\text{ext}}(\mathbf{r}_i - \mathbf{a}_I), \tag{1.1}$$

Here, i, j index all electron coordinates, $\mathbf{r}_i$ represents electron positions, I and $\mathbf{a}_I$ are similar for the ions,

and V_{ext} is the external potential, usually representing the Coulomb interaction with the ions in a crystal. Miraculously, hidden within this relatively simple linear partial differential equation contains all the information required to derive much of the low-temperature phenomena of condensed matter physics and chemistry. Generalizations to relativistic effects such as spin-orbit coupling are also possible [18].

The first-principles equation (1.1) is general enough to describe phenomena from computer chips, to combustion, to biology, to superconductors, and yet is detailed enough to give material-specific information. For example, it can compute parameters required to predict the superconducting transition temperature of H_3S [19]. In H_3S, the theoretical prediction starting from first-principles calculations finds $T_c \approx 194$ K [20] and the highest measured experimental transition is close at 203 K. Unlike the unconventional superconductors, calculations motivated the experimental discoveries [19, 16]. First-principles calculations also currently used to guide designs of silicon or silicon alternatives to improve the efficiency of solar cells [21, 22], as well as discovering new ferroelectrics [23].

The fact that such a simple equation can derive all the diverse behaviors of electrons in solids should suggest that doing so is not always trivial. While simple to write down, (1.1) represents a coupled set of $3N$ equations, where N is the number of electrons necessary to describe, which needs to be extrapolated to the thermodynamic limit. Current methods can solve some realistic systems accurately enough to closely match experimental results, but they also fail in other cases. It is often difficult to calculate accurate properties for systems with localized d or f electrons, for example, many of the unconventional superconductors, as well as VO_2, NiO, MnO, and other transition metal oxide systems. Many technological applications, from medical (e.g. MRI), to energy [24, 25], to transportation [26], to research [27, 28] would benefit from superconductors with high transition temperatures and tunable materials' properties. Understanding unconventional superconductors may play an important role in this pursuit due to their unique properties. Transition metal compounds can also display important properties besides superconductivity. Perovskites containing transition metals exhibit colossal magnetoresistance, which have technological applications in, for example, disk drives [29]. Spinel systems with transition metals in frustrated lattices may give rise to uncommon quantum mechanical states, with possible applications to quantum computing [30]. Materials design for these systems would benefit from better access to accurate properties calculated from first-principles.

1.2 Effective models from first-principles calculations

A natural question emerges as to whether a simpler but less general model than (1.1) can sufficiently describe a material, in the expectation that the simpler model be solved more accurately. For example,

much of the early successful theories of electrons in materials, such as Drude theory [31], have been based on the **non-interacting approximation**: the assumption that electrons behave as though they experience no interactions at all. In this case, the $3N$ coupled equations are replaced by N 3-dimensional equations—a dramatic simplification which often makes the problem tractable. In certain cases, the origin of this phenomenon may be understood from from Laudau's Fermi-liquid theory. When it is possible to adiabatically connect the interacting system to a non-interacting model, there is a one-to-one mapping between non-interacting eigenstates and eigenstates of the interacting system. The result is that the excitations of the interacting system are describable by excitations of the non-interacting system with adjusted properties; these excitations are known as **quasiparticle excitations** [32].

Approximations which solve (1.1) directly by dropping electron interactions would be incredibly inaccurate. For example, consider an electrons on the surface of a neutral solid. Without electron-electron interaction, the electrons would incorrectly experience an enormous attractive interaction to the center of the solid. Instead, the effect of interactions need to be incorporated into the definition of the non-interacting problem. For many semiconductors and insulators, a noninteracting effective model can often describe many of the low-lying excitations, albeit with interactions accounted for by adjusting the external potential [33]. On the other hand, in transition metal oxides such as FeO, NiO, CoO, MnO, and other systems containing rare earth atoms, systems with partially-filled conduction bands are insulating [34, 35], something not explainable with a non-interacting model without breaking spin-symmetry. Violations of theoretical limits of Fermi liquid theory are also prevalent in the normal state of cuprate superconductors as well [36, 37]. In these situations, the system is not close to any known exactly solvable model.

Often, the one-band Hubbard model is referred to as the simplest model displaying strong correlation effects, effects that cannot be described by effective non-interacting models [35], but the extent to which a simple Hubbard model is a good model for a given material is difficult to evaluate [38]. Addressing these kinds of questions is also possible starting from (1.1). Already, first-principles calculations are widely used for interpretation of experiments based on providing noninteracting models that reasonably describe the system [39, 40]. One approach is testing predictions of interacting theories using first-principles results [41]. A more systematic approach is downfolding [42]: a computational process for determining models which can reproduce targeted features of (1.1). Finding the types of models that reproduce first-principles properties of correlated quantum materials, like superconductors, would build intuition and understanding of quantum mechanical systems far from the noninteracting limit. However, as discussed in Chapter 3, downfolding the first-principles Hamiltonian into a simple but accurate effective model is also an important unsolved problem.

1.3 Outline of the dissertation

My Ph.D. work has contributed to both aspects of first-principles calculations: (a) connections to experiments through benchmarking, interpreting experimental results, and making predictions for experiments and (b) connections to simplified models through downfolding. My focus has been developing benchmarks for the first-principles diffusion Monte Carlo method, and developing strategies for downfolding using it and variational Monte Carlo.

In Chapters 2 and 3, I overview state-of-the-art first-principles methods and downfolding methods. I discuss their fundamental assumptions, where they make approximations, give some examples of calculations, and summarize the current challenges. I have used four of these methods for work in my Ph.D.: Hartree-Fock, density functional theory, variational Monte Carlo, and diffusion Monte Carlo. For these four methods I have a more detailed theoretical discussion and literature review. Chapter 4 summarizes how the presented methods are used in most of the calculations.

I have performed several benchmarks of diffusion Monte Carlo, studying the limitations of the method due to the fixed-node approximation and other errors. In Chapter 5, in collaboration with an undergraduate, I compare the computation of reaction barrier heights from fixed-node diffusion Monte Carlo to experiment. The results achieved "chemical accuracy," or the accuracy required for making predictions for room-temperature chemical reactions. In Chapter 6, I report a diffusion Monte Carlo benchmark on the structural and magnetic properties of FeSe, an iron-based superconductor. In this compound, my collaborators and I found diffusion Monte Carlo reproduces lattice parameters and the equation-of-state, even when common density functional theory approaches fail.

I also develop strategies for developing simple models for correlated-electron systems. In Chapter 6, based on diffusion Monte Carlo calculations on FeSe, I report a relationship between the charge and spin of the system. I propose a simple model based on Hund's coupling which can explain the features seen in our calculations. In Chapter 7, I report diffusion Monte Carlo calculations on an FeSe diatomic molecule, and combined with downfolding and techniques from machine learning, determined a minimal effective model for the system. This technique provided a second, more quantitative verification of the importance of Hund's coupling in Fe-Se system, relative to other model terms. In Chapter 8, I applied a simple downfolding technique to $MgTi_2O_4$ to make a prediction for the singlet-triplet excitation energy. We found that experimental searches for this excitation were being conducted at a lower energy than our calculations suggest it should be found, which has motivated a new search for the excitation. In Chapter 9, I demonstrate a new technique we discovered, which allows for a systematic determination of the low-energy subspace of a system. Eigenstates within this low-energy subspace correspond to eigenstates of simpler lattice models, which can be solved to

greater accuracy.

In Chapter 10, I will review the importance of these results for advancing our capabilities for predictive calculations of materials' properties using theory.

1.4 Summary of accomplishments

To complete this work, I have accomplished the following:

- **Code development for the open-source package, QWalk [43]**. I developed a high-throughput python workflow package for performing density functional theory, variational Monte Carlo, and diffusion Monte Carlo calculations [44, 45]. This package includes scripts for interfacing QWalk with PySCF and CRYSTAL, two packages for performing other types of calculations. Two undergraduates have worked with me and utilized this code under my guidance to perform the benchmark studies of barrier heights and the convex hull of the Si-O system (the latter is ongoing).

- **Benchmark studies of diffusion Monte Carlo and downfolding techniques**. These include the molecular barrier heights, the structural properties of FeSe, and the prediction for singlet-triplet gap of $MgTi_2O_4$. Large-scale benchmark studies of non-hydrogen transfer reaction barriers using diffusion Monte Carlo were not available before this work. Our benchmark of FeSe was the first calculation of structural properties of an iron-based superconductor using diffusion Monte Carlo. The calculation of $MgTi_2O_4$ is the first first-principles prediction for the singlet-triplet gap in that system that I am aware of, and represents an important example of a first-principles prediction for a correlated-electron material conducted in advance of experimental verification.

- **Applying first-principles quantum Monte Carlo to understand strongly-correlated electrons**. In bulk FeSe, our work discovered evidence for spin-charge coupling in the system. This spin-charge was later discovered to correlate well with unconventional superconductivity [46]. We were able to explain these observations using a simple model depending on strong Hund's coupling. In the FeSe diatomic molecule, I tested the technique of orthogonal matching pursuit applied to a downfolding technique and utilized it to quantify the importance of different types of model interactions in that system. This approach defines a systematic procedure for stepping from simple, more inaccurate models to more complex, more accurate ones. We found that Hund's coupling was the more important term to include in the model, and could quantify its importance. Based on the difficulties with current strategies for downfolding, I also helped develop and test a new strategy for sampling

low-energy states. This technique should provide a more systematic procedure for downfolding with diffusion Monte Carlo in future calculations.

Papers associated with this work:

- Results on bulk FeSe are published in B. Busemeyer, M. Dagrada, S. Sorella, M. Casula, and L. K. Wagner, "Competing collinear magnetic structures in superconducting FeSe by first-principles quantum Monte Carlo calculations," *Phys. Rev. B*, **94**, 3,035108, (2016).

- Results on barrier heights are published in K. Krongchon, B. Busemeyer, and L. K. Wagner, "Accurate barrier heights using diffusion Monte Carlo," *The Journal of Chemical Physics*, **146**, 12, 124129, (2017).

- Results on FeSe diatomic molecules are published in H. Zheng, H. J. Changlani, K. T. Williams, B. Busemeyer, and L. K. Wagner, "From Real Materials to Model Hamiltonians With Density Matrix Downfolding," *Front. Phys.*, **6**, (2018).

- Results from $MgTi_2O_4$ are published in B. Busemeyer, G. J. MacDougall, and L. K. Wagner, "Prediction for the singlet-triplet excitation energy for the spinel $MgTi_2O_4$ using first-principles diffusion Monte Carlo," *Phys. Rev. B*, **99**, 8, 081118, (2019).

An additional report benchmarking diffusion Monte Carlo on the formation energy of Si-O compounds is currently in preparation.

Chapter 2

Current state-of-the-art in first-principles methods

I focus this review on zero-temperature approaches which have been applied to the first-principles Hamiltonian (1.1). These methods focus on determining properties of the ground state or a few of the lowest energy eigenstates of the electronic first-principles Hamiltonian. Because the Fermi energy of most materials is much larger than the thermal energy in the temperature ranges of interest, zero-temperature approaches are sufficient for most low-temperature electronic phenomena.

2.1 Wave-function methods

Wave function methods attempt to solve the exact first-principles Hamiltonian (1.1) in a subspace of the full Hilbert space. If the ground state or if the first few eigenstates of (1.1) lie within this subspace, then the methods will be exact. If these eigenfunctions can be expressed to a good approximation by elements of the subspace, the methods will be accurate, otherwise, they will incur large errors. Because they all share the same Hamiltonian, the resulting energies can often be made **variational**—they represent a strict upper-bound for the true energy of the system. By looking for the least upper bound to the energy, different wave function methods can be compared and any free parameters can be determined independently of experiment.

2.1.1 Hartree-Fock and configuration interaction

Basic definitions. Hartree-Fock solves for the ground state of the first-principles equation in the subspace of Slater determinants [47, 48]:

$$\Phi(\mathbf{R}) = \mathrm{Det}\left([\phi_i(\mathbf{r}_k)]\right) \equiv \mathrm{Det}\begin{pmatrix} \phi_1(\mathbf{r}_1) & \cdots & \phi_1(\mathbf{r}_N) \\ \vdots & \ddots & \vdots \\ \phi_N(\mathbf{r}_1) & \cdots & \phi_N(\mathbf{r}_N) \end{pmatrix}. \tag{2.1}$$

For nonrelativistic calculations, a wave function for up and down electrons together can be expressed as a product of determinants: $\mathrm{Det}\left([\phi_{\uparrow,i}(\mathbf{r}_j)]\right)\mathrm{Det}\left([\phi_{\downarrow,i}(\mathbf{r}_j)]\right)$, where $\phi_{\uparrow,i}(\mathbf{r}_j) = \phi_{\downarrow,i}(\mathbf{r}_j)$ in **restricted Hartee-**

Fock, and $\phi_{\uparrow,i}(\mathbf{r}_j) \neq \phi_{\downarrow,i}(\mathbf{r}_j)$ in **unrestricted Hartree-Fock**. The method determines the orbitals in $\mathrm{Det}\left([\phi_{\uparrow,i}(\mathbf{r}_j)]\right)\mathrm{Det}\left([\phi_{\downarrow,i}(\mathbf{r}_j)]\right)$ by solving the Hartree-Fock equations self-consistently:

$$(\hat{T} + V_{\mathrm{eff}}^{\mathrm{HF}}(\mathbf{r}))\phi_{\sigma_i,i}^{\sigma}(\mathbf{r}) = \varepsilon_i^{\sigma}\phi_{\sigma_i,i}(\mathbf{r}) \tag{2.2}$$

$$V_{\mathrm{eff}}^{\mathrm{HF}}(\mathbf{r}) = -\frac{1}{2}\nabla^2 + V_{\mathrm{ext}}(\mathbf{r}) + \sum_{j,\sigma_j}\int d\mathbf{r}'\frac{\phi_{\sigma_j,j}^*(\mathbf{r}')\phi_{\sigma_j,j}(\mathbf{r}')}{|\mathbf{r}-\mathbf{r}'|} - \sum_{j,\sigma_j}\int d\mathbf{r}'\frac{\phi_{\sigma_j,j}^*(\mathbf{r}')\phi_{\sigma_i,i}(\mathbf{r}')}{|\mathbf{r}-\mathbf{r}'|}\frac{\phi_{\sigma_j,j}(\mathbf{r})}{\phi_{\sigma_i,i}(\mathbf{r})} \tag{2.3}$$

These equations can be derived using the method of Lagrange multipliers on the expression for the energy of a Slater determinant (see §2.5). The first integral is known as the **Hartree potential**, and is the energy of the classical charge distribution $n(\mathbf{r}) = |\phi_{\sigma_j,j}(\mathbf{r})|^2$ interacting with the electron in orbital $\phi_{\sigma_i,i}(\mathbf{r})$. The second integral is known as the **exchange potential**, and represents the difference between the exact interaction potential and the classical Hartree potential for this wave function.

The eigenvalues in Hartree-Fock, ε_i, have a well-defined meaning through Koopman's theorem [49, 50]. Let $\hat{c}_k$ represent the destruction operator for an orbital from the Hartree-Fock equations. $\varepsilon_k - \varepsilon_l$ represents the energy of $\hat{c}_k^\dagger\hat{c}_l|\Phi(\mathbf{R})\rangle$: a Slater determinant formed by removing the electron from orbital ϕ_l and placing it in ϕ_k without adjusting the other orbitals. Intuitively, this will over-estimate excitation energies considering that the energy of the determinant may be lowered by allowing the other orbitals to adjust to the change in $V_{\mathrm{eff}}^{\mathrm{HF}}(\mathbf{r})$. This is also commonly found in practice [51, 52]. Replacing one orbital is a **singles excitation**, two is a **doubles excitation**, and so on.

Configuration interaction (CI) methods determine the lowest energy wave function of the form:

$$\Psi(\mathbf{R}) = \sum_i c_i\Phi_i(\mathbf{R}); \qquad \Phi_i(\mathbf{R}) = \mathrm{Det}\left([\phi_{i,j}(\mathbf{r}_k)]\right) \equiv \mathrm{Det}\begin{pmatrix} \phi_{i,1}(\mathbf{r}_1) & \cdots & \phi_{i,1}(\mathbf{r}_N) \\ \vdots & \ddots & \vdots \\ \phi_{i,N}(\mathbf{r}_1) & \cdots & \phi_{i,N}(\mathbf{r}_N) \end{pmatrix}. \tag{2.4}$$

Often $\phi_{i,j}(\mathbf{r}_k)$ are solutions from the Hartree-Fock equations, but these can also be optimized. The set of all determinants formed by excitations of the Hartree-Fock determinant is a basis for the N-body Hilbert space. Expressing the many-body Hamiltonian in this basis and exactly diagonalizing is the method known as **full configuration interaction (FCI)** [53]. The number of orbitals determined by the Hartree-Fock equations is N_{basis}, the number of single-particle basis functions used to solve the equations. The number of determinants in this basis is therefore $\binom{N_{\mathrm{basis}}}{N}$. To be complete, N_{basis} needs to extrapolated to infinity.

Many other post-Hartree-Fock methods can be described as selecting a subspace of the FCI basis in which to solve the Hamiltonian. For example, **complete active space (CAS)** chooses $N_{\mathrm{active}} < N$ orbitals from the first N orbitals and N_{virtual} orbitals from the rest, and only takes determinants that differ

by interchanging the occupation of those [53]. **Selected configuration interaction** methods use other various strategies to choose the determinants [54]. These methods scale combinatorially with the number of orbitals allowed to be used for excitations when generating determinants [54, 55].

Approximations. Slater determinants encode no correlation effects aside from the antisymmetry between two electrons of the same spin. Because of this, the energy of a wave function relative to the Hartree-Fock ground state energy is often referred to as the **correlation energy**. Hartree-Fock is exact for a non-interacting system, and normally provides a poor description when correlation effects are important.

Because each single Slater determinant encodes no correlations, combinations of determinants are required to describe correlations. Some types of correlations are easily captured by a few determinants; these are often called "non-dynamical" correlations in chemistry literature, and often arise from states composed of nearly degenerate orbitals [56]. Correlations in general may require many determinants, as can be seen by examples [55, 57, 58], or by a simple argument. Because the Coulomb repulsion in (1.1) has a singularity in the potential energy whenever $\mathbf{r}_i \to \mathbf{r}_j$, in this limit there must be a corresponding singularity in the kinetic energy to keep the total energy finite. This is known as the **cusp condition** [59] because it requires a cusp in the wave function when $\mathbf{r}_i \to \mathbf{r}_j$. Because each determinant encodes no correlations, its Laplacian at any point in space away from an ion is finite, and therefore an infinite number of determinants are required to produce a cusp. This is just one example of a property that exact eigenstates of $\hat{H}$ should have which is difficult to describe using few determinants; other correlations also might be important and also difficult to describe. Additional determinants also will be needed if the orbital set $\{\phi_{i,j}\}$ determined from Hartree-Fock is not optimal for the expansion when $c_i \neq 0$ for $i > 0$. If any method drops determinants that are important for describing any of these effects, large errors may result. The FCI method is only exact when N_{basis} can be extrapolated to infinity, which increases the computational requirements combinatorially fast.

Examples of applications. Hartree-Fock has been broadly applied to both molecules [53] and solids [60, 61], calculating properties such as cohesive energy, band gaps, and Compton profiles. Failures of Hartree-Fock are common, for instance, Hartree-Fock overestimates the band gaps of solid neon and argon by 4.0 eV and 4.4 eV, respectively [51]. The Hartree-Fock overestimates band-gap of Si by approximately 5.6 eV [62]. Hartree-Fock calculations of bond-distances of second-row diatomic molecules errs by roughly 0.1 Bohr and calculation of the binding energy can err by roughly 50%, or even fail to predict the binding of the molecule [63]. Post-Hartree-Fock methods can reach a high degree of accuracy for small molecules, for example, within mHa of the exact energy for molecules containing on the order of 10 electrons or fewer [58, 64]. Due to combinatorial scaling with system size, FCI can only be applied to systems roughly the size of H_2O or smaller [65]

Current challenges. While highly accurate solutions are possible in theory, it is difficult to reach the basis size, system size, and number of determinants required in correlated electron materials. For example, for an Fe_2S_2 cluster, a CAS on the important bonding orbitals would require 10^{16} determinants [57]. Choosing a subspace that is too small can drastically affect the accuracy of the method. A complete active space calculation performed on just the Fe d orbitals of the Fe_2S_2 cluster found and electron affinity of 1.1 eV, whereas the experimental estimate was 2.15 eV [55]. The number of determinants required to recover the same percentage of correlation energy scales exponentially with N [66]. In solids, wave functions with a fixed number of determinants also have a **size-extensivity** problem: their energy converges to the Hartree-Fock energy as N is extrapolated to the thermodynamic limit.

2.1.2 Coupled cluster

Basic definitions. **Coupled cluster** generates the wave function by applying the operator, $e^{\hat{C}}$ to the Hartree-Fock determinant, $|\Phi_0\rangle$. In the **coupled cluster with singles and doubles (CCSD)** approximation, $\hat{C} = \hat{C}_1 + \hat{C}_2$. $\hat{C}_1 = \sum_{ij} t_{ij} \hat{c}_i^\dagger c_j$ generates a linear combination of singles excitations of the Hartree-Fock determinant, and $\hat{C}_2 = \sum_{ijkl} t_{ijkl} c_i^\dagger c_j^\dagger c_k c_l$ generates a combination of the doubles excitations. Therefore, $e^{\hat{C}}|\Phi_0\rangle$ generates an infinite sum of determinants whose coefficients are the Taylor expansion coefficients of the exponential. A major advantage to this approach is coupled-cluster expansions do not have a size-extensivity problem [67]. Generalizations to triples, quadruples, and so on are generated similarly. Including triples is called CCSDT (T standing for triples); including quadruples is CCSDTQ, etc.

Approximations. This parameterization is only exact when $\hat{C}$ contains all orders of excitations. When $\hat{C} = \hat{C}_1$, for example, the estimate of the ground state will not deviate from Hartree-Fock, because $e^{\hat{C}}|\Phi_0\rangle$ is a determinant [68], and Hartree-Fock is already the lowest-energy Slater determinant. Evaluation of the energy of the wave function, $e^{\hat{C}}|\Phi_0\rangle$ is usually approximated in a way which is non-variational [67, 69]. For this reason, finding a lower energy in coupled cluster compared to another wave function approach does not necessarily imply coupled cluster is a better estimate of the ground state energy.

Examples of applications. Coupled cluster has been applied extensively to molecules and polymers [67, 69]. In the context of solids, CCSD has been applied in the case of diamond and silicon. In silicon, it finds the band gap within 0.02 eV of the experimental results, and in diamond, the error is on the order of 0.1 eV [70]. In both these calculations, errors from the basis set and k-points are still large compared to the scale of the gap, so it is unclear if better calculations will still be in agreement. It has also been applied to the study of H_2O absorption on BN and graphite [71] which matched diffusion Monte Carlo calculations on the same system [72] and found good agreement with experiment. CCSD has also been

applied to transition-metal-containing molecules with mixed results [73, 74, 75].

Current challenges. While requiring less computational resources than many post-Hartree-Fock methods, CCSD roughly scales with $N^2 N_{\text{unocc}}^4$ [67], where $N_{\text{unocc}} = N_{\text{basis}} - N$, which makes finite size and basis set convergence difficult. CCSDT scales with $N^3 N_{\text{unocc}}^5$ and CCSDTQ scales with $N^4 N_{\text{unocc}}^6$. For small system sizes, $N \sim 10$ and $N_{\text{unocc}} \sim 100$, CCSDT is a factor of 10^3 more computationally difficult than CCSD and CCSDTQ is a factor of 10^6 more difficult than CCSD. This makes it difficult to perform calculation much above the level of CCSD for larger systems. Even in molecules composed of s and p orbitals, corrections to CCSD can be on the order of 0.1 eV, compared to CCSDTQ or FCI [67]. In transition metals, errors of CCSD compared to CCSDT or CCSDTQ are often greater because the Hartree-Fock reference is a worse approximation when correlations are important.

In extended systems, CCSD scales with $N^2 N_{\text{unocc}}^4 N_k^4$, where N_k is the number of k-points sampled in the Brillouin zone [70]. Calculations also scale sharply in memory requirements: $N^2 N_{\text{unocc}}^4 N_k^3$ [70]. These issues make it very difficult to converge the basis set and level of approximation in large systems.

2.1.3 Density matrix renormalization group (DMRG) and extensions

Correlations in ground state wave functions are short-ranged for gapped Hamiltonians [76, 77, 78]. This implies that a large part of Hilbert space capable of describing long-range correlations are not needed for these ground state calculations. This observation is the concept behind density matrix renormalization group, an algorithm for optimizing matrix product states (MPS). MPS is another type of determinant expansion which is exceptionally well-suited to describe short-range correlations in one dimension.

Basic definitions. The MPS are defined as [77]:

$$|\Psi_{\text{MPS}}\rangle = \sum_{n_1,\ldots n_{\text{N}_{\text{basis}}}=0}^{2} \left(\prod_{i=1}^{N_{\text{basis}}} M_{n_i}^i \right) |n_1, ..., n_{N_{\text{basis}}}\rangle \tag{2.5}$$

The $|n_1, ..., n_{N_{\text{basis}}}\rangle$ refers to a Fock state; the Slater determinant of §2.1.1 is the expression of this state in the real-space basis. i indexes different basis set elements, for example a single-particle orbital basis. Matrix elements of $M_{n_i}^i$ are the variational parameters of the wave function. If $M_{n_i}^i$ are allowed to be any size, and N_{basis} is large enough, this parameterization can express any many-body wave function [77, 78]. Notice the one-dimensional structure of the states: every matrix corresponding to a basis element i directly multiples $i-1$ and $i+1$ only. The connection to renormalization group theory is not discussed here, but if interested, see Ref. [79].

Approximations. To create more compact but approximate states, DMRG relies on the singular value

decomposition. Any matrix, M, can be factorized via a singular value decomposition (SVD) into $M = UDV^\dagger$. The SVD has the property that keeping the largest N_{bond} elements of the diagonal matrix, D, and setting the rest to zero, then $UDV^\dagger$ represents the optimal rank-N_{bond} approximation of M. One version of the algorithm known as single-site DMRG uses singular-value decompositions to approximate matrices in (2.5) by keeping only at most N_{bond} of their singular values nonzero. N_{bond} is called the **bond dimension** of the matrix product state, and is a measure of the degree of correlation between the two sites. When $N_{\text{bond}} = 1$ the state represents an uncorrelated state [77, 78]. At larger values of N_{bond}, it can be shown that the correlations described by (2.5) between electrons within basis set element i and j drop exponentially with $i - j$ [77, 78].

Examples of applications. DMRG has been used extensively in one-dimensional and quasi-one-dimensional systems, where it can match exact methods. In N_2, the nitrogen binding curve matches FCI [80]. In Cr_2, the ground state energy matches FCI [81]. It has also been applied to larger molecules, where it was used to analyze the ground state properties and correlation functions between the sites [82]. DMRG was also applied to the Fe_2S_2 cluster referenced in §2.1.1, where it found new low-energy spin eigenstates not describable by a simple Heisenberg model [57]. It was also applied to the 1-D hydrogen chain, where the method matched many methods including FCI on the equation-of-state [83]. It is also sometimes applied to 2-d models, for example the one-band Hubbard model in 2-d [84].

Current challenges. Ground state wave functions of gapped Hamiltonians obey area law entanglement entropy, which implies correlations are short-ranged for these ground states [77, 78]. Excited states generally may not, which sometimes limits its use as an excited state or time-dependent method [77].

In two dimensions or more, the MPS can be constructed by choosing an ordering for the basis set. [76]. If the basis consists of localized orbitals in real space, this can be viewed as a kind of threading of a one-dimensional chain through the space [84]. In realistic calculations, practical orderings must be explored, and generally, placing bonding and antibonding orbitals near one another in the product is advantageous [76]. Because the correlations described at a fixed bond dimension drop exponentially with separation in the chain, the computational costs scale exponentially in each dimension higher than one [76, 77], which has limited its use in first-principles calculations in greater-than-one dimension.

2.1.4 Variational Monte Carlo

Variational Monte Carlo (VMC) [85, 86] can be summarized as using Monte Carlo integration to variationally optimize the parameters of a trial wave function, $|\Psi_{\text{T}}(\mathbf{P})\rangle$, where $\mathbf{P}$ is the vector of parameters for optimization. I will focus on energy minimization for concreteness, but other objective functions exist, such

as variance minimization [87] or the method discussed in Chapter 9. Standard numerical optimizations are sufficient for this task, but require access to the energy and potentially derivatives of the energy with respect to $\mathbf{P}$.

Monte Carlo integration for expectation values

A quantum mechanical expectation value can be cast as an expectation value of a probability distribution:

$$\langle \hat{H} \rangle = \int d\mathbf{R} \frac{\langle \Psi | \mathbf{R} \rangle \langle \mathbf{R} | \hat{H} | \Psi_{\mathrm{T}} \rangle}{\langle \Psi_{\mathrm{T}} | \Psi_{\mathrm{T}} \rangle} = \int d\mathbf{R} \ \frac{|\langle \mathbf{R} | \Psi_{\mathrm{T}} \rangle|^2}{\langle \Psi_{\mathrm{T}} | \Psi_{\mathrm{T}} \rangle} \frac{\langle \mathbf{R} | \hat{H} | \Psi_{\mathrm{T}} \rangle}{\langle \mathbf{R} | \Psi_{\mathrm{T}} \rangle} = \int d\mathbf{R} \ \mathcal{P}(\mathbf{R}) E_{\mathrm{L}}(\mathbf{R}). \tag{2.6}$$

Here, $\mathcal{P}(\mathbf{R}) = \frac{|\langle \mathbf{R} | \Psi_{\mathrm{T}} \rangle|^2}{\langle \Psi_{\mathrm{T}} | \Psi_{\mathrm{T}} \rangle}$ is the probability distribution of the $|\Psi_{\mathrm{T}}\rangle$ in real-space, and $E_{\mathrm{L}}(\mathbf{R}) = \frac{\langle \mathbf{R} | \hat{H} | \Psi_{\mathrm{T}} \rangle}{\langle \mathbf{R} | \Psi_{\mathrm{T}} \rangle}$ is a quantity referred to as the **local energy**. In probability theory, integrating to obtain an expectation value is equivalent to computing the sample mean of the distribution in the limit of infinite samples,

$$\langle \hat{H} \rangle = \int d\mathbf{R} \mathcal{P}(\mathbf{R}) E_{\mathrm{L}}(\mathbf{R}) = \lim_{N_w \to \infty} \frac{1}{N_w} \sum_{\mathbf{R} \in \mathcal{P}}^{N_w} E_{\mathrm{L}}(\mathbf{R}), \tag{2.7}$$

where the sum refers to taking N_w samples from the probability distribution $\mathcal{P}(\mathbf{R})$. The error due to the finite sampling can be estimated by the standard deviation of the mean, which is equal to $(\mathrm{Var}(E_{\mathrm{L}}(\mathbf{R}))/N_w)^{1/2}$, where $\mathrm{Var}(E_{\mathrm{L}}(\mathbf{R}))$ is the variance of $E_{\mathrm{L}}(\mathbf{R})$ over the samples. Sampling $\mathcal{P}(\mathbf{R})$ is done using a Metropolis Markov process [88].

Types of trial wave functions

I focus on Slater-Jastrow wave functions because they have been benchmarked in the context of QMC simulations, including correlated-electron systems [89]. These wave functions take the form

$$\Psi_{\mathrm{T}}(\mathbf{R}) = \Phi(\mathbf{R}) J(\mathbf{R}). \tag{2.8}$$

The first factor is a Slater determinant or sum of Slater determinants and the second factor is a Jastrow factor wave function, both discussed here.

Many-electron wave functions must be antisymmetric, and for this dissertation, the antisymmetric property is provided by the Slater determinant. The Slater determinant for a set of orbitals $\{\phi_i\}_{i=1}^{N}$ is defined

the same as in §2.1.1:

$$\Phi_0(\mathbf{R}) = \mathrm{Det}\left([\phi_i(\mathbf{r}_j)]\right) \equiv \mathrm{Det}\begin{pmatrix} \phi_1(\mathbf{r}_1) & \cdots & \phi_1(\mathbf{r}_N) \\ \vdots & \ddots & \vdots \\ \phi_N(\mathbf{r}_1) & \cdots & \phi_N(\mathbf{r}_N) \end{pmatrix}. \tag{2.9}$$

A weighted sum of Slater determinants is known as a **multi-Slater** wave function,

$$\Phi(\mathbf{R}) = \sum_k c_k \Phi_k(\mathbf{R}) = \sum_k c_k \mathrm{Det}\left([\phi_{\uparrow,k,\mathbf{r}_i}(\mathbf{r}_{\uparrow,j})]\right)\mathrm{Det}\left([\phi_{\downarrow,k,\mathbf{r}_i}(\mathbf{r}_{\downarrow,j})]\right), \tag{2.10}$$

where now $\phi_{\sigma,k,i}(\mathbf{r}) \neq \phi_{\sigma,l,i}(\mathbf{r})$. The orbitals may be provided by another method (such as Hartree-Fock or density functional theory), or they may be optimized. The strengths and weaknesses of Slater determinant expansions were discussed in §2.1.1.

The most important correlations between electrons occur at short range, which are nonexistent for the Slater determinant (aside from the exchange hole), and difficult to describe with few Slater determinants. The Jastrow factor can describe these local correlations, in addition to some long-range correlations, and also satisfy the **cusp condition** [59]. The form used in this work is known as a "two-body Jastrow factor":

$$J(\mathbf{R}) = e^{U(\mathbf{R})}; \qquad U(\mathbf{R}) = \sum_{iIk} c_k^{\mathrm{en}} a_k(r_{iI}) + \sum_{ijk} c_k^{\mathrm{ee}} b_k(r_{ij}), \tag{2.11}$$

where $r_{iI} = |\mathbf{r}_i - \mathbf{a}_I|$ and $r_{ij} = |\mathbf{r}_i - \mathbf{r}_j|$. The second sum of $U(\mathbf{R})$ allows for electrons to avoid one another at close range, and puts in the cusp condition [59] corresponding to the singularity in the Coulomb repulsion between two electrons. Often this second term suppresses the wave function near the ions, and the first sum of $U(\mathbf{R})$ corrects this [65]. The first sum is also used to satisfy the cusp condition corresponding to any singularities in the V_{ext}, which are present due when V_{ext} includes the Coulomb potential of the ions. The c_k are all variational parameters, except that c_0^{en} and c_0^{ee} is set to satisfy cusp conditions if required. For the results in this dissertation,

$$a_0 = b_0 = \frac{cp(r/r_{\mathrm{cut}})}{1+\gamma p(r/r_{\mathrm{cut}})}; \qquad p(x) = x - x^2 + x^3/3; \tag{2.12}$$

$$a_{k>0}(r) = b_{k>0}(r) = \frac{1 - z(r/r_{\mathrm{cut}})}{1+\beta_k z(r/r_{\mathrm{cut}})}; \qquad z(x) = x^2(6 - 8x + 3x^2). \tag{2.13}$$

The a_0 and b_0 terms create a discontinuity in the gradient of magnitude c, while γ is a variational parameter. The $k > 0$ the functions are used to describe correlations in the wave function, and β_k will all be variational

Figure 2.1: A pedagogical example of how the off-diagonal of the 1-RDM characterizes the system. Consider if $|\phi_i\rangle$ orbitals represent s orbitals on each H atom, and the Hamiltonian for two H_2 molecules separated by a large distance is diagonalized in this basis. The ground state is an antisymmetrized product of two bonding orbitals: $|ab\rangle = (|a\rangle + |b\rangle)/\sqrt{2}$ and $|bc\rangle = (|c\rangle + |d\rangle)/\sqrt{2}$. In this case $\rho^{(1)}_{\uparrow,\mathrm{a,b}} = 1/2$ and $\rho^{(1)}_{\uparrow,\mathrm{a,c}} = 0$, characterizing the bonding in the system. This is because the up electron can be removed from (a) and placed into (b) holding all else fixed (not time-evolving the system, for example). There is no probability for the right H_2 to have three electrons, and so removing an electron from (a) and placing it on (c) has no amplitude: $\rho^{(1)}_{\uparrow,\mathrm{a,c}} = 0$.

parameters. This particular form forces the Jastrow function to go smoothly to zero at $r = r_{\mathrm{cut}}$ [90]. For systems with periodic boundary conditions, r_{cut} is set low enough to avoid correlations that are longer than the supercell size.

Quantities available from VMC

The routine outlined in §2.1.4 discusses how to evaluate $\langle \hat{H} \rangle$ for a given trial wave function, but the method generalizes to other observables. The one-body reduced density matrix is a particularly important observable which demonstrates how observables besides the energy are calculated. A simple way to define the **one-body reduced density matrix (1-RDM)** is $\rho^{(1)}_{\sigma,ij} = \langle \Psi_0 | \hat{c}^\dagger_{\sigma,i} \hat{c}_{\sigma,j} | \Psi_0 \rangle$. $\hat{c}_{\sigma,i}$ represents the destruction operator for an electron of spin σ acting on a one-body orbital, $|\phi_i\rangle$. The diagonal of the matrix represents the occupation of the orbital in the ground state. One way of understanding the off-diagonal of the 1-RDM is as the instantaneous-time limit of the one-body Green function in a basis: $G_{\sigma ij}(t) = \langle \Psi_0 | \hat{c}^\dagger_{\sigma,i} e^{-t\hat{H}} \hat{c}_{\sigma,j} | \Psi_0 \rangle$. This measures the amplitude for removing an electron in $|\psi_i\rangle$, evolving the system for a time t, then placing it back in $|\phi_j\rangle$. Consider the pedagogical example in Fig. 2.1; as reasoned in the caption, the off-diagonal is larger between two orbitals that are hybridized in a bonding orbital. The off-diagonal of the 1-RDM is thus useful for characterizing bonding in the system.

Similar to (2.16), the strategy is to convert the quantum expectation value into a expectation in proba-

bility:

$$\langle \hat{c}^\dagger_{\sigma,i} c_{\sigma,j} \rangle = \int d\mathbf{R} \frac{|\langle \mathbf{R}|\Psi_\mathrm{T}\rangle|^2}{\langle \Psi_\mathrm{T}|\Psi_\mathrm{T}\rangle} \frac{\langle \mathbf{R}|\hat{c}^\dagger_{\sigma,i}\hat{c}_{\sigma,j}|\Psi_\mathrm{T}\rangle}{\langle \mathbf{R}|\Psi_\mathrm{T}\rangle} \tag{2.14}$$

Now there is an additional complication in that $\langle \mathbf{R}|\hat{c}^\dagger_i \hat{c}_j|\Psi_\mathrm{T}\rangle$ is nonlocal; it depends on the value of the wave function throughout space.

$$\langle \mathbf{R}|\hat{c}^\dagger_i \hat{c}_j|\Psi_\mathrm{T}\rangle = \int d\mathbf{R}' \ \langle \mathbf{R}|\hat{c}^\dagger_{\sigma,i}\hat{c}_{\sigma,j}|\mathbf{R}'\rangle\langle \mathbf{R}'|\Psi_\mathrm{T}\rangle = \sum_{a=1}^{N} \int d\mathbf{r}'_a \ \phi^*_i(\mathbf{r}_a)\phi_j(\mathbf{r}'_a)\langle \mathbf{R}'_a|\Psi_\mathrm{T}\rangle, \tag{2.15}$$

where $\mathbf{R}'_a$ is the same as $\mathbf{R}$ except that $\mathbf{r}_a$ (the a-th coordinate) is replaced by $\mathbf{r}'_a$. The last equality follows because the matrix element of $\langle \mathbf{R}|\hat{c}^\dagger_i \hat{c}_j|\mathbf{R}'\rangle$ is nonzero only when $\mathbf{R}$ and $\mathbf{R}'$ differ by one coordinate. Now the sampling will require an additional integration, which can be incorporated into the Monte Carlo integration:

$$\langle \hat{c}^\dagger_{\sigma,i}\hat{c}_{\sigma,j}\rangle = \sum_{a=1}^{N} \int d\mathbf{R} d\mathbf{r}'_a \frac{|\Psi_\mathrm{T}(\mathbf{R})|^2}{\langle \Psi_\mathrm{T}|\Psi_\mathrm{T}\rangle} \frac{\phi^*_i(\mathbf{r}_a)\phi_j(\mathbf{r}'_a)\Psi_\mathrm{T}(\mathbf{R}'_a)}{\Psi_\mathrm{T}(\mathbf{R})} \tag{2.16}$$

An efficient sampling probability for this new coordinate is $f(\mathbf{r}'_a) \propto \sum_i |\phi_i(\mathbf{r}'_a)|^2$ [91].

The **two-body reduced density matrix (2-RDM)** is another important quantity, and it is defined as $\rho^{(2)}_{\sigma\eta ijkl} = \langle \Psi_0|\hat{c}^\dagger_{\sigma i}\hat{c}^\dagger_{\eta j}\hat{c}_{\sigma k}\hat{c}_{\eta j}|\Psi_0\rangle$. This is accessible from VMC using a similar derivation, but involving two additional electron coordinates [91]. This quantity measures static correlations between electrons in the system. For instance, $\rho^{(2)}_{\uparrow\downarrow iiii} = \langle \Psi_0|\hat{c}^\dagger_{\uparrow i}\hat{c}^\dagger_{\downarrow i}\hat{c}_{\uparrow i}\hat{c}_{\downarrow i}|\Psi_0\rangle = \langle \Psi_0|\hat{n}_{\uparrow i}\hat{n}_{\downarrow i}|\Psi_0\rangle$ represents the expected double occupation of an orbital, which appears as the interaction term in the Hubbard model. Two-body spin correlations are also expressible as combinations of elements of the two-body density matrix, for instance,

$$\hat{S}_i \cdot \hat{S}_j = \hat{S}_{i,x}\hat{S}_{j,x} + \hat{S}_{i,y}\hat{S}_{j,y} + \hat{S}_{i,z}\hat{S}_{j,z} = \hat{S}_{i,+}\hat{S}_{j,-} + \hat{S}_{i,-}\hat{S}_{j,+} + \hat{S}_{i,z}\hat{S}_{j,z} \tag{2.17}$$

$$= \frac{1}{2}\left(\hat{c}^\dagger_{\uparrow i}\hat{c}_{\downarrow i}\hat{c}^\dagger_{\downarrow j}\hat{c}_{\uparrow j} + \hat{c}^\dagger_{\downarrow i}\hat{c}_{\uparrow i}\hat{c}^\dagger_{\uparrow j}\hat{c}_{\downarrow j}\right) + \frac{1}{4}(\hat{n}_{\uparrow i} - \hat{n}_{\downarrow i})(\hat{n}_{\uparrow j} - \hat{n}_{\downarrow j}) \tag{2.18}$$

$$\langle \hat{S}_i \cdot \hat{S}_j\rangle = \frac{1}{2}\left(\rho^{(2)}_{\uparrow\downarrow ijji} + \rho^{(2)}_{\downarrow\uparrow ijji}\right) + \frac{1}{4}\left(\rho^{(2)}_{\uparrow\downarrow ijij} + \rho^{(2)}_{\downarrow\uparrow ijij} - \rho^{(2)}_{\uparrow\uparrow ijij} - \rho^{(2)}_{\downarrow\downarrow ijij}\right) \tag{2.19}$$

where $\hat{S}_{i,\pm} = \hat{S}_x \pm i\hat{S}_y$ are the spin raising and lowering operators.

Applications and current challenges

The accuracy of VMC is intimately linked to the parameterization of $\Psi_\mathrm{T}(\mathbf{R};\mathbf{P})$. The space of wave functions formed by all possible parameter values of $\Psi_\mathrm{T}(\mathbf{R};\mathbf{P})$ is a subspace of the full Hilbert space. Both ground [85,

86] and excited state [92, 93] calculations are possible. Similar to the post-Hartree-Fock methods, if the eigenstate of interest is far from this subspace, there will be errors. For realistic systems it is often difficult to find parameterizations that are efficient to evaluate while also being capable of describing states of interest [94]. Accurate wave functions may require thousands to tens of thousands of parameters to be optimized [95, 96], and increasing numbers of parameters tends to make optimization more difficult [95]. Recently, artificial neural networks have been used as variational wave functions [97], however, applications to large or realistic systems as well as wave functions with signs or complex numbers, such as fermionic wave functions, is still difficult [98].

Nonetheless efficiently-optimized wave functions can still recover a large proportion of the correlation energy, and when used as a starting point for diffusion Monte Carlo, improve the energy and variance of the diffusion Monte Carlo result. For example, in second-row atoms and dimers, efficient parameterizations can recover 70–90% of the correlation energy, depending on the system and the parameterization [94]. Running diffusion Monte Carlo with these as a starting point increases the captured correlation energy to 90–95%.

2.1.5 Diffusion Monte Carlo

Diffusion Monte Carlo (DMC) is a type of projector Monte Carlo and is the central method employed in my Ph.D. work. Projector Monte Carlo methods access eigenstate properties by applying the operator $e^{-\tau\hat{H}}$ for large τ [65]. As discussed in the FCI method of §2.1.1, expanding eigenstates in a determinant basis is prohibitively difficult, due to the exponentially large Hilbert space. Instead projector Monte Carlo methods focus on computing expectation values and do not attempt to expand the eigenstates in a basis [99]. The derivation I outline is based on Ref. [65] and Ref. [99].

DMC focuses on computing the expectation values of eigenstates by sampling real-space coordinates, $\mathbf{R}$. Let $|\Psi_{\mathrm{T}}\rangle$ be a trial function with an analytic representation. We can act $\hat{H}$ on $|\Psi_{\mathrm{T}}\rangle$ in a manner similar to §2.1.4 because the analytical form is known. Let $\{|\Psi_i\rangle\}_{i=1}^{\infty}$ be the eigenstates of $\hat{H}$, where $|\Psi_0\rangle$ is the ground state. Because $\hat{H}$ is hermitian, the mixed expectation value accesses the energy of the eigenstate: $\langle\Psi_i|\hat{H}|\Psi_{\mathrm{T}}\rangle = E_i\langle\Psi_i|\Psi_{\mathrm{T}}\rangle$. For illustration, consider a calculation of the ground state energy, and let $\langle\Psi_0|\Psi_{\mathrm{T}}\rangle \neq 0$. Expressing the mixed expectation value in the real-space basis,

$$E_0 = \frac{\langle\Psi_0|\hat{H}|\Psi_{\mathrm{T}}\rangle}{\langle\Psi_0|\Psi_{\mathrm{T}}\rangle} = \frac{\int d\mathbf{R}\ \Psi_0^*(\mathbf{R})\Psi_{\mathrm{T}}(\mathbf{R})E_{\mathrm{L}}(\mathbf{R})}{\int d\mathbf{R}\ \Psi_0^*(\mathbf{R})\Psi_{\mathrm{T}}(\mathbf{R})}, \tag{2.20}$$

where $E_{\mathrm{L}}(\mathbf{R}) = \hat{H}\Psi_{\mathrm{T}}(\mathbf{R})/\Psi_{\mathrm{T}}(R)$—the same as in §2.1.4. The form of this integral is similar to the integral (2.16) appearing in VMC (§2.1.4), except that $|\Psi_{\mathrm{T}}(\mathbf{R})|^2$ is replaced by $\Psi_0^*(\mathbf{R})\Psi_{\mathrm{T}}(\mathbf{R})$. Similar to VMC,

this integral can be computed using Monte Carlo sampling. Information about $\Psi_0(\mathbf{R})$ is computed using imaginary-time evolution.

Imaginary-time evolution

Acting the operator, $e^{-\tau\hat{H}}$, on a trial wave function, $|\Psi_{\mathrm{T}}\rangle$, determines the lowest-energy eigenstate with nonzero overlap with $|\Psi_{\mathrm{T}}\rangle$:

$$|\Psi_{\mathrm{T}}\rangle = \sum_{i=0}^{\infty} |\Psi_i\rangle\langle\Psi_i|\Psi_{\mathrm{T}}\rangle; \qquad\qquad e^{-\tau\hat{H}}|\Psi_{\mathrm{T}}\rangle \sim e^{-\tau E_m}|\Psi_m\rangle\langle\Psi_m|\Psi_{\mathrm{T}}\rangle \tag{2.21}$$

in the limit of large τ, where m is the smallest m such that $\langle\Psi_m|\Psi_{\mathrm{T}}\rangle \neq 0$. $e^{-\tau\hat{H}}$ is also the Green function of the Schrödinger equation equation when time is imaginary [65, 100]: $t \to i\tau$,

$$-\partial_\tau \Psi(\mathbf{R},\tau) = \hat{H}\Psi(\mathbf{R},\tau) \qquad\qquad \Longleftrightarrow \qquad\qquad \Psi(\mathbf{R},\tau) = \int dR'\ G(\mathbf{R},\mathbf{R}',\tau)\Psi(\mathbf{R}',0), \tag{2.22}$$

where $G(\mathbf{R},\mathbf{R}',\tau) = \langle\mathbf{R}|e^{-\tau\hat{H}}|\mathbf{R}'\rangle$ is the **imaginary-time Green function** in the real-space basis. To summarize, propagation in imaginary time has the effect of exponentially suppressing high-energy states. Under the assumption $\langle\Psi_{\mathrm{T}}|\Psi_0\rangle \neq 0$, then (2.21) expressed in the real-space basis implies

$$\Psi_0(\mathbf{R}_1) = \lim_{\tau\to\infty} e^{\tau E_0}\langle\Psi_0|\Psi_{\mathrm{T}}\rangle^{-1} \int d\mathbf{R}_2 \langle\mathbf{R}_1|e^{-\tau\hat{H}}|\mathbf{R}_2\rangle\Psi_{\mathrm{T}}(\mathbf{R}_2). \tag{2.23}$$

The prefactor, $e^{\tau E_0}\langle\Psi_0|\Psi_{\mathrm{T}}\rangle^{-1}$, will cancel in the ratio of (2.20). The only important still-unknown quantity is $G(\mathbf{R}_1,\mathbf{R}_2,\tau) = \langle\mathbf{R}_1|e^{-\tau\hat{H}}|\mathbf{R}_2\rangle$.

The Trotter formula [101] applied on this expression gives

$$\langle\mathbf{R}_1|e^{-\tau\hat{H}}|\mathbf{R}_2\rangle = \langle\mathbf{R}_1|e^{-\tau\hat{V}}e^{-\tau\hat{T}}|\mathbf{R}_2\rangle + \mathcal{O}(\tau[\hat{T},\hat{V}]) \tag{2.24}$$

$$= e^{-\tau V(\mathbf{R}_1)}\langle\mathbf{R}_1|e^{-\tau\hat{T}}|\mathbf{R}_2\rangle + \mathcal{O}(\tau[\hat{T},\hat{V}]), \tag{2.25}$$

assuming $\hat{V}$ is diagonal in the real-space basis (e.g. for Coulomb interactions).

$$\langle\mathbf{R}_1|e^{-\tau\hat{T}}|\mathbf{R}_2\rangle = G_{\mathrm{D}}(\mathbf{R}_1,\mathbf{R}_2,\tau) = (2\pi\tau)^{3/2}\exp\{-(\mathbf{R}_1-\mathbf{R}_2)^2/(2\tau)\}$$

represents the Green function for the diffusion equation. This is the origin of the name "diffusion Monte Carlo." This might be expected because the imaginary-time Schrödinger equation (2.35) with $\hat{V} \to 0$ is

exactly the diffusion equation.

The expression (2.24) is not useful yet, because in the limit $\tau \to \infty$ the error of the Trotter break-up goes to infinity. Let $\tau = M\Delta\tau$, where M is a large integer. $\Delta\tau$ will be known as the **time step**.

$$\langle \mathbf{R}_1 | e^{-\tau \hat{H}} | \mathbf{R}_M \rangle = \langle \mathbf{R}_1 | (e^{-\Delta\tau \hat{H}})^M | \mathbf{R}_M \rangle = \int dR_2 ... dR_{M-1} \prod_{i=1}^{M-1} \langle \mathbf{R}_i | e^{-\Delta\tau \hat{H}} | \mathbf{R}_{i+1} \rangle \tag{2.26}$$

$$= \int dR_2 ... dR_{M-1} \prod_{i=1}^{M-1} \left[e^{-\tau V(\mathbf{R}_i)} G_{\mathrm{D}}(\mathbf{R}_i, \mathbf{R}_{i+1}, \Delta\tau) \right] + \mathcal{O}(\Delta\tau [\hat{T}, \hat{V}]). \tag{2.27}$$

The limit where $\Delta\tau \to 0$ will now converge to the exact propagation. We reach the $\tau \to \infty$ limit by taking $M \to \infty$.

Collecting these results, the expression for ground state wave function is

$$\Psi_0^*(\mathbf{R}_1) = \int d\mathbf{R}_2 ... d\mathbf{R}_M \prod_{i=1}^{M-1} \left[e^{-\tau V(\mathbf{R}_i)} G_{\mathrm{D}}(\mathbf{R}_i, \mathbf{R}_{i+1}, \Delta\tau) \right] \Psi_{\mathrm{T}}^*(\mathbf{R}_M) \tag{2.28}$$

The product, $\prod_i G_{\mathrm{D}}(\mathbf{R}_i, \mathbf{R}_{i+1})$, the probability density of Brownian particle taking a path $\mathbf{R}_1 \to \mathbf{R}_2 \to \cdots \to \mathbf{R}_M$ in 3-N dimensional space—a $3MN$-dimensional configuration.

Applying this formula to (2.20),

$$E_0 = \frac{\int d\mathbf{R}\ \Psi_0^*(\mathbf{R}) \Psi_{\mathrm{T}}(\mathbf{R}) E_{\mathrm{L}}(\mathbf{R})}{\int d\mathbf{R}\ \Psi_0^*(\mathbf{R}) \Psi_{\mathrm{T}}(\mathbf{R})} = \frac{\int d\mathbf{R}_1 ... d\mathbf{R}_M\ \mathcal{P}(\mathbf{R}_1, ..., \mathbf{R}_M) W(\mathbf{R}_1, ..., \mathbf{R}_M) E_L(\mathbf{R}_M)}{\int d\mathbf{R}_1 ... d\mathbf{R}_M\ \mathcal{P}(\mathbf{R}_1, ..., \mathbf{R}_M) W(\mathbf{R}_1, ..., \mathbf{R}_M)} \tag{2.29}$$

$$\mathcal{P}(\mathbf{R}_1, ..., \mathbf{R}_M) = \prod_{i=1}^{M-1} G_{\mathrm{D}}(\mathbf{R}_i, \mathbf{R}_{i+1}, \Delta\tau) \tag{2.30}$$

$$W(\mathbf{R}_1, ..., \mathbf{R}_M) = \Psi_{\mathrm{T}}(\mathbf{R}_1) \Psi_{\mathrm{T}}^*(\mathbf{R}_M) \prod_{i=1}^{M-1} e^{-\tau V(\mathbf{R}_i)}. \tag{2.31}$$

In this form, the numerator and denominator represent expectation values of $W(\{\mathbf{R}_i\}) E_{\mathrm{L}}(\mathbf{R}_M)$ and $W(\{\mathbf{R}_i\})$, respectively, over the probability distribution $\mathcal{P}(\{\mathbf{R}_i\})$ of Brownian paths going from $\mathbf{R}_1$ to $\mathbf{R}_M$. This can be sampled with a set of walkers executing Brownian diffusion dynamics [65], and thus converted into a ratio of sample means:

$$E_0 \approx \frac{\sum_{\{\mathbf{R}_i\} \in B} W(\mathbf{R}_1, ..., \mathbf{R}_M) E_{\mathrm{L}}(\mathbf{R}_j)}{\sum_{\{\mathbf{R}_i\} \in B} W(\mathbf{R}_1, ..., \mathbf{R}_M)} \tag{2.32}$$

B is a set of Brownian paths with Gaussian random steps of variance $\Delta\tau$.

There are two problems with the current approach. (a) A numerical instability occurs when the weights, $W(\mathbf{R}_1, ..., \mathbf{R}_M)$, average to zero. This happens for antisymmetric $\Psi_{\mathrm{T}}(\mathbf{R})$, which I discuss in the next section.

(b) The variance of the weights, $W(\{\mathbf{R}_i\})$, is extremely large because $V(\mathbf{R}_i)$ contains Coulomb singularities, making this algorithm useless for most practical calculations. A simple modification to the routine to utilize importance sampling will resolve this problem.

Sign problem and fixed-node approximation

The expression for the energy (2.20) has a problem when $\int d\mathbf{R}_1, ...d\mathbf{R}_M P(\{\mathbf{R}_i\})W(\{\mathbf{R}_i\}) = 0$, because the denominator approaches zero in the limit of infinite samples. In fact, both numerator and denominator approach zero, and their ratio remains finite, approaching E_0. Small fluctuations in either the numerator or the denominator will cause wild changes in their ratio, and the variance of this process increases exponentially with the system size [100]. This is an instance of a **sign problem** which can occur in stochastic methods.

There are important cases where the average sign is not zero. For example, if the $\Psi_{\mathrm{T}}(\mathbf{R})$ no nodes (e.g. zeros), then it will never change sign. It is straightforward to see that

$$W(\mathbf{R}_1, ..., \mathbf{R}_M) = \Psi_{\mathrm{T}}(\mathbf{R}_1)\Psi^*_{\mathrm{T}}(\mathbf{R}_M) \prod_{i=1}^{M-1} e^{-\tau V(\mathbf{R}_i)} \geq 0$$

and therefore cannot average to zero. In this case, E_0 is the energy of the bosonic ground state, $\Psi_0(\mathbf{R}) = \Psi_{\mathrm{B}}(\mathbf{R})$, which also has no nodes. For this reason, DMC can be made exact for bosonic ground states [100].

In the case of a fermionic $\Psi_{\mathrm{T}}(\mathbf{R})$, then evaluating (2.20) has the **fermion sign problem**, because fermionic wave functions are antisymmetric [100]. The sign of $W(\mathbf{R}_1, ..., \mathbf{R}_M)$ is equal to the sign of the product, $\Psi_{\mathrm{T}}(\mathbf{R}_1)\Psi_{\mathrm{T}}(\mathbf{R}_M)$. In the limit of infinite M, the positions of $\mathbf{R}_1$ and $\mathbf{R}_M$ become uncorrelated, and thus $\langle\Psi_{\mathrm{T}}(\mathbf{R}_1)\Psi_{\mathrm{T}}(\mathbf{R}_M)\rangle = \langle\Psi_{\mathrm{T}}(\mathbf{R}_1)\rangle\langle\Psi_{\mathrm{T}}(\mathbf{R}_M)\rangle = 0 \cdot 0$. To compute the energy of a fermionic state, $\Psi_{\mathrm{T}}(\mathbf{R})$ must have fermion symmetry, because $\hat{H}$ commutes with the particle-permutation operator, and hence $e^{-\tau\hat{H}}$ cannot change the particle symmetry of $\Psi_{\mathrm{T}}(\mathbf{R})$.

One way to ensure that $\Psi_{\mathrm{T}}(\mathbf{R}_1)\Psi_{\mathrm{T}}(\mathbf{R}_M) \geq 0$ is to reject all walker steps that cross a node (or zero) of the trial wave function. This is known as the **fixed-node approximation**, because it implies the projected wave function computed with this constraint, $|\Psi_{\mathrm{FN}}\rangle \propto e^{-\tau\hat{H}}|\Psi_{\mathrm{T}}\rangle$, will have the same nodes as $|\Psi_{\mathrm{T}}\rangle$. $|\Psi_{\mathrm{FN}}\rangle$ is called the **fixed-node wave function**. Three important properties hold for this approximation:

(a) $E_{\mathrm{FN}} = \langle\Psi_{\mathrm{FN}}|\hat{H}|\Psi_{\mathrm{FN}}\rangle/\langle\Psi_{\mathrm{FN}}|\Psi_{\mathrm{FN}}\rangle \geq E_0$.

(b) E_{FN} is the lowest energy wave function with the same nodes as Ψ_{T}.

(c) In the case that $|\Psi_{\mathrm{T}}\rangle$ has the same nodes as $|\Psi_0\rangle$ (but may differ away from the nodes), $|\Psi_{\mathrm{FN}}\rangle = |\Psi_0\rangle$.

Because these are important for interpreting the results in this dissertation, I will outline a rough proof of

these properties [102].

Consider replacing the external potential energy in $\hat{H}$ with

$$V'_{\rm ext}(\mathbf{R}) = \begin{cases} V_{\rm ext}(\mathbf{R}) & \mathbf{R} \in P_+ = \{\mathbf{R}|\Psi_T(\mathbf{R}) \geq 0\} \\ \infty & \mathbf{R} \notin P_+ \end{cases} \tag{2.33}$$

Let this modified Hamiltonian be $\hat{H}_+$. Walkers that cross the nodes of $\Psi_T(\mathbf{R})$ int the exact algorithm all contribute zero weight, and so there is no sign problem. The wave function that results from the projection under this operator is $\Psi_+(\mathbf{R}) \sim e^{-\tau \hat{H}_+}\Psi_{\rm T}(\mathbf{R})$, and is the ground state of $\hat{H}_+$.

$\Psi_+(\mathbf{R})$ is zero for $\mathbf{R} \notin P_+$. Let $\Psi_{\rm FN}(\mathbf{R}) = \Psi_+(\mathbf{R})$ for $\mathbf{R} \in P_+$, but enforce particle antisymmetry for $\mathbf{R} \notin P_+$. For instance $\Psi_{\rm FN}((\mathbf{r}_1, \mathbf{r}_2)) = -\Psi_{\rm FN}((\mathbf{r}_2, \mathbf{r}_1))$ for $N = 2$. This is equal to the fixed-node wave function corresponding to $\Psi_{\rm T}(\mathbf{R})$. Because $\Psi_{\rm FN}(\mathbf{R})$ is an antisymmetric wave function in the Hilbert space of $\hat{H}$, the fixed-node energy, $E_{\rm FN} = \langle \Psi_{\rm FN}|\hat{H}|\Psi_{\rm FN}\rangle \geq E_0$, the ground-state energy of $\hat{H}$. This proves (a). Because $|\Psi_+\rangle$ is also the ground state of $\hat{H}_+$ and any wave function with the same nodes as $|\Psi_{\rm T}\rangle$ is a valid wave function for $\hat{H}_+$ with the correct boundary conditions on the nodal surface, $|\Psi_{\rm FN}\rangle$ is the minimum energy wave function among these, proving (b).

Assume $\Psi_T(\mathbf{R})$ has the same nodes as $\Psi_0(\mathbf{R})$, the ground state of $\hat{H}$. Due to the linearity of $\hat{H}$, because $\hat{H}_+ = \hat{H}$ within P_+ and because $\Psi_{\rm FN}(\mathbf{R}) = \Psi_0(\mathbf{R}) = 0$ on the boundary, $\Psi_{\rm FN}(\mathbf{R}) = \Psi_0(\mathbf{R})$ in P^+ by the uniqueness theorem for partial differential equations. By particle antisymmetry they also also equal for all $\mathbf{R}$. By this reasoning, when the nodes of $\Psi_{\rm T}(\mathbf{R})$ are exact, then $\Psi_{\rm FN}(\mathbf{R}) = \Psi_0(\mathbf{R})$ and $E_{\rm FN} = E_0$. This proves (c).

Practical necessities: importance sampling and managing walker weights

Importance sampling is imperative for practical calculations because it removes singularities in the walker weights and drastically reduces nodal crossings which must be killed or rejected. Returning to the mixed expectation value,

$$E_0 = \frac{\langle \Psi_0|\hat{H}|\Psi_{\rm T}\rangle}{\langle \Psi_0|\Psi_{\rm T}\rangle} = \frac{\int d\mathbf{R}\ \Psi_0^*(\mathbf{R})\Psi_{\rm T}(\mathbf{R})E_{\rm L}(\mathbf{R})}{\int d\mathbf{R}\ \Psi_0^*(\mathbf{R})\Psi_{\rm T}(\mathbf{R})} = \frac{\int d\mathbf{R}\ f_0(\mathbf{R})E_{\rm L}(\mathbf{R})}{\int d\mathbf{R}\ f_0(\mathbf{R})}, \tag{2.34}$$

where $f_0(\mathbf{R}) = \Psi_0(\mathbf{R})\Psi_{\rm T}(\mathbf{R})$ is the **mixed distribution**. The following function converges to the mixed-distribution in the limit of large imaginary time: $f(\mathbf{R}, \tau) = \Psi_{\rm T}(\mathbf{R})\Psi^*_{\rm T}(\mathbf{R}, \tau)$, where $\Psi_{\rm T}(\mathbf{R}, 0) = \Psi_{\rm T}(\mathbf{R})$. By

multiplying (2.35) by $\Psi_{\mathrm{T}}(\mathbf{R})$,

$$\Psi^*(\mathbf{R},\tau) = \int d\mathbf{R}'\ G(\mathbf{R},\mathbf{R}',\tau)\Psi^*(\mathbf{R}',0) \implies f(\mathbf{R},\tau) = \int d\mathbf{R}'\ G(\mathbf{R},\mathbf{R}',\tau)\frac{\Psi_{\mathrm{T}}(\mathbf{R})}{\Psi_{\mathrm{T}}(\mathbf{R}')}|\Psi_{\mathrm{T}}(\mathbf{R}')|^2 \tag{2.35}$$

$$= \int d\mathbf{R}'\ \tilde{G}(\mathbf{R},\mathbf{R}',\tau)f(\mathbf{R}',0), \tag{2.36}$$

where $\tilde{G}(\mathbf{R},\mathbf{R}',\tau) = G(\mathbf{R},\mathbf{R}',\tau)\Psi_{\mathrm{T}}(\mathbf{R})/\Psi_{\mathrm{T}}(\mathbf{R}')$ is the **importance-sampled Green function**, which evolves $f(\mathbf{R},\tau)$ in imaginary time. Notice that $\tilde{G}$ is larger than G for moves $\mathbf{R}' \to \mathbf{R}$ that increase the value of Ψ_{T}. The differential equation corresponding to $\tilde{G}$ can be derived similarly, by multiplying the imaginary time Schrödinger equation by $\Psi_{\mathrm{T}}(\mathbf{R})$ and rearranging terms. Doing this yields [100]:

$$-\partial_\tau f(\mathbf{R},\tau) = (-\frac{1}{2}\nabla^2 + \nabla\cdot\mathbf{v}_{\mathrm{Q}}(\mathbf{R}) + \mathbf{v}_{\mathrm{Q}}(\mathbf{R})\cdot\nabla + E_{\mathrm{L}}(\mathbf{R}))f(\mathbf{R},\tau), \tag{2.37}$$

where $\mathbf{v}_{\mathrm{Q}}(\mathbf{R}) = \nabla\Psi_{\mathrm{T}}(\mathbf{R})/\Psi_{\mathrm{T}}(\mathbf{R})$. The terms containing $\mathbf{v}_{\mathrm{Q}}(\mathbf{R})$ represent a drift term in the diffusion equation [100]. The Trotter break-up to approximate this term is similar to the steps I took for G, and it results in the following approximation of $\tilde{G}$ [100]:

$$f_0(\mathbf{R}_1) = \int d\mathbf{R}_1 ... d\mathbf{R}_M \prod_{i=1}^{M-1}\left[e^{-\tau E_{\mathrm{L}}(\mathbf{R}_i)}\tilde{G}_{\mathrm{D}}(\mathbf{R}_i,\mathbf{R}_{i+1},\Delta\tau)\right] f(\mathbf{R}_M,0); \tag{2.38}$$

$$\tilde{G}_{\mathrm{D}}(\mathbf{R}_i,\mathbf{R}_{i+1},\tau) = (2\pi\tau)^{3/2}\exp\{-(\mathbf{R}_i - \mathbf{R}_{i+1} + \mathbf{v}_{\mathrm{Q}}(\mathbf{R}))^2/(2\tau)\}. \tag{2.39}$$

$\tilde{G}_{\mathrm{D}}$ is the Green function for the diffusion equation with a drift term proportional to $\mathbf{v}_{\mathrm{Q}}(\mathbf{R})$. Rather than pure Brownian motion, the walkers will drift towards regions of large $\Psi_{\mathrm{T}}(\mathbf{R})$.

The final Monte Carlo integral with importance sampling is

$$E_0 = \frac{\int d\mathbf{R}\ f_0(\mathbf{R})E_{\mathrm{L}}(\mathbf{R})}{\int d\mathbf{R}\ f_0(\mathbf{R})} = \frac{\int d\mathbf{R}_1 ... d\mathbf{R}_M\ \tilde{\mathcal{P}}(\mathbf{R}_1,...,\mathbf{R}_M)\tilde{W}(\mathbf{R}_1,...,\mathbf{R}_M)E_L(\mathbf{R}_M)}{\int d\mathbf{R}_1 ... d\mathbf{R}_M\ \tilde{\mathcal{P}}(\mathbf{R}_1,...,\mathbf{R}_M)\tilde{W}(\mathbf{R}_1,...,\mathbf{R}_M)} \tag{2.40}$$

$$\approx \frac{\sum_{\{\mathbf{R}_i\}\in\tilde{B}}\tilde{W}(\mathbf{R}_1,...,\mathbf{R}_M)E_{\mathrm{L}}(\mathbf{R}_j)}{\sum_{\{\mathbf{R}_i\}\in\tilde{B}}\tilde{W}(\mathbf{R}_1,...,\mathbf{R}_M)}; \tag{2.41}$$

$$\tilde{\mathcal{P}}(\mathbf{R}_1,...,\mathbf{R}_M) = \prod_{i=1}^{M-1}\tilde{G}(\mathbf{R}_{i+1},\mathbf{R}_i,\Delta\tau)|\Psi_{\mathrm{T}}(\mathbf{R}_1)|^2 \tag{2.42}$$

$$\tilde{W}(\mathbf{R}_1,...,\mathbf{R}_M) = \prod_{i=1}^{M-1} e^{-\tau E_{\mathrm{L}}(\mathbf{R}_i)}. \tag{2.43}$$

$\tilde{B}$ is now a set of paths whose initial position, $\mathbf{R}_1$, are sampled from $|\Psi_{\mathrm{T}}(\mathbf{R}_1)|^2$ and execute drifted diffusion according to $\mathbf{v}_{\mathrm{Q}}(\mathbf{R}_i)$. While integral is equal to the non-importance-sampled version (2.29) when evaluated

exactly, there are two major practical advantages to importance-sampled DMC. (a) The weights are now $e^{-\tau E_{\mathrm{L}}(\mathbf{R}_i)}$ at each step. If $\Psi_{\mathrm{T}}(\mathbf{R})$ satisfies the cusp conditions, the Coulomb singularities cancel out between the $\hat{T}$ and $\hat{V}$ parts of $\hat{H}$, dramatically reducing the variance of the weights. Additionally, in the limit that $\Psi_{\mathrm{T}}(\mathbf{R})$ is exactly an eigenstate, $\Psi_i(\mathbf{R})$, then $E_{\mathrm{L}}(\mathbf{R}) = E_i$, a constant. Therefore if $\Psi_{\mathrm{T}}(\mathbf{R})$ is a reasonable approximation to an eigenstate, the variance of weights will be much more reduced. (b) As walkers approach a node of $\Psi_{\mathrm{T}}(\mathbf{R})$, $\mathbf{v}_{\mathrm{Q}}(\mathbf{R}) = \nabla\Psi_{\mathrm{T}}(\mathbf{R})/\Psi_{\mathrm{T}}(\mathbf{R})$ diverges away from the node, and therefore, node crossings are much more rare compared to random Brownian motion. Because the time step is finite, some walkers will still cross a node occasionally, and these moves need to be rejected. [100].

Although the variance of the weights is greatly reduced by importance sampling, because the weight of walker is a product of many random numbers, the variance of the walker weights is still very large [99]. A few walkers will be generating most of the important weight for the final average, and many of the walkers will be contributing essentially nothing, but nonetheless consume computational resources for their propagation. Instead, a birth/death process is used to redistribute the weights and keep the variance of the weights low. The set of walkers with weight larger than some number (1.8 for QWalk [90, 43]) are selected for branching. Each larger walker with weight w_1 and position $\mathbf{R}_1$ are matched with the walker with lowest weight, w_2, at position $\mathbf{R}_2$ that has not been branched for this step. With probability $p = w_1/(w_1 + w_2)$, the walker at $\mathbf{R}_2$ is killed and a new walker is born at $\mathbf{R}_1$ with weight $(w_1 + w_2)/2$. The walker already at $\mathbf{R}_1$ has its weight set to $(w_1 + w_2)/2$ as well. With probability $1 - p$, the walker at $\mathbf{R}_1$ is killed and a similar birth occurs at $\mathbf{R}_2$. This particular approach keeps the number of walkers fixed, which improves parallelization, while ensuring that the walker weights do not grow larger than 1.8.

A second issue is that the sum of the walker weights will grow or decline depending on the energy of the trial wave function [65]. To control the total sum of the walker weights and keep it from growing or shrinking as the propagation progresses, a constant, E_{ref} is added to the local energy and adjusted to keep the total weight reasonably constant [65, 90]. This can be interpreted as keeping the norm of $\Psi_{\mathrm{T}}(\mathbf{R}, \tau)$ constant as $\tau \to \infty$ [65].

Fixed-node and excited states

Although the fixed-node approximation usually contributes error to ground state properties, it also gives control over the projected wave function, $|\Psi_{\mathrm{FN}}\rangle$. If $\Psi_{\mathrm{T}}(\mathbf{R})$ is approximately an excited state, then $\Psi_{\mathrm{FN}}(\mathbf{R})$ can be a close approximations of that eigenstate [103]. It is also possible to design $\Psi_{\mathrm{FN}}(\mathbf{R})$ with certain spin textures. For example, consider Fig. 2.2. $\Psi_{\mathrm{T}}(\mathbf{R})$ was constructed from Kohn-Sham wave functions with different patterns of stripes or checkerboard spin density on the iron sites. After applying fixed-node

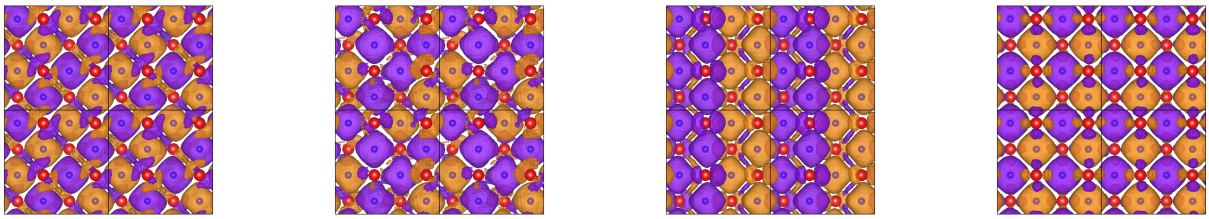

(a) (b) (c) (d)

Figure 2.2: Spin densities of FeSe magnetic spin textures at ambient pressure, (a) collinear, (b) collinear, 1 flip, (c) bicollinear, and (d) checkerboard. Four unit cells of a single iron layer are shown, divided by black lines. "Collinear, 1 flip" refers to flipping the spin of one iron per unit cell in the collinear configuration. Since four unit cells are shown above, there are four "flipped" iron moments shown in this plot. The larger red Se atoms lie above and below the plane and show significantly smaller spin density. Irons are smaller and blue, and lie within larger concentration of spin. The two colors of the isosurfaces denote density of up and down.

diffusion Monte Carlo to each of those states, the spin density of those states kept the same pattern, but lowered the overall energy of the state.

However, it is difficult to determine if the $\Psi_{\mathrm{T}}(\mathbf{R})$ nodes are a good guess for the state of interest. Because $\Psi_{\mathrm{T}}(\mathbf{R})$ may not be orthogonal to the ground state, no variational principle exists to systematically choose parameters for target states. Nonetheless, in practice, DMC estimations of excited state energies successfully reproduce experimental results in a variety of examples. Optical gap calculations are possible using diffusion Monte Carlo by using singles excitations of Kohn-Sham wave functions to define nodes of a trial function [89, 103, 104]. Models fit to spin excitations have also been used to compute properties which match experiment [105, 106, 107, 41].

Quantities available from DMC

For observables that commute with $\hat{H}$, the derivation for the DMC estimate is easily generalized from §2.1.5, similar to the generalization presented in §2.1.4. The mixed expectation value does not equal the expectation value for an $\hat{O}$ such that $[\hat{O}, \hat{H}] \neq 0$:

$$\lim_{\tau\to\infty} \frac{\langle\Psi_{\mathrm{T}}|\hat{O}e^{-\tau\hat{H}}|\Psi_{\mathrm{T}}\rangle}{\langle\Psi_{\mathrm{T}}|e^{-\tau\hat{H}}|\Psi_{\mathrm{T}}\rangle} = \frac{\langle\Psi_{\mathrm{T}}|\hat{O}|\Psi_0\rangle}{\langle\Psi_{\mathrm{T}}|\Psi_0\rangle} \neq \frac{\langle\Psi_0|\hat{O}|\Psi_0\rangle}{\langle\Psi_0|\Psi_0\rangle} \tag{2.44}$$

This is known as the **mixed estimator**, which is a good estimate of the ground state expectation value when $\Psi_{\mathrm{T}}(\mathbf{R})$ is close to the true ground state, $\Psi_0(\mathbf{R})$. It is not an exact estimate because $\hat{O}$ may map $|\Psi_0\rangle$ to eigenstates of higher energies which have nonzero overlap with $|\Psi_{\mathrm{T}}\rangle$.

There are two methods of correcting the mixed-estimator error, computing the **extrapolated estimator** [108] and a related projection algorithm known as reptation Monte Carlo [109]. Reptation Monte Carlo

essentially performs the projection on both sides: $\lim_{\tau\to\infty}\langle\Psi_{\mathrm{T}}|e^{-\tau\hat{H}}\hat{O}e^{-\tau\hat{H}}|\Psi_{\mathrm{T}}\rangle/\langle\Psi_{\mathrm{T}}|e^{-2\tau\hat{H}}|\Psi_{\mathrm{T}}\rangle$ which requires additional computational resources.

In this dissertation, only the extrapolated estimator is utilized. If the trial function is close to the ground state in the sense that $|\Psi_0\rangle = |\Psi_{\mathrm{T}}\rangle + \varepsilon|\tilde{\Psi}_{\mathrm{T}}\rangle$, where all wave functions are normalized and ε is a small number, then

$$\langle\Psi_{\mathrm{T}}|\hat{O}|\Psi_0\rangle = \langle\Psi_{\mathrm{T}}|\hat{O}|\Psi_{\mathrm{T}}\rangle + \varepsilon\langle\Psi_{\mathrm{T}}|\hat{O}|\tilde{\Psi}_{\mathrm{T}}\rangle; \tag{2.45}$$

$$\langle\Psi_0|\hat{O}|\Psi_0\rangle = \langle\Psi_{\mathrm{T}}|\hat{O}|\Psi_{\mathrm{T}}\rangle + 2\varepsilon\mathrm{Re}\left[\langle\Psi_{\mathrm{T}}|\hat{O}|\tilde{\Psi}_{\mathrm{T}}\rangle\right] + O(\varepsilon^2). \tag{2.46}$$

Fixed-node or fixed-phase DMC calculations here fix either the sign or the phase of the wave function, so $\mathrm{Re}\left[\langle\Psi_{\mathrm{T}}|\hat{O}|\tilde{\Psi}_{\mathrm{T}}\rangle\right] = \langle\Psi_{\mathrm{T}}|\hat{O}|\tilde{\Psi}_{\mathrm{T}}\rangle$. In that case, taking a combination to cancel the first-order error,

$$\langle\Psi_0|\hat{O}|\Psi_0\rangle = 2\langle\Psi_{\mathrm{T}}|\hat{O}|\Psi_0\rangle - \langle\Psi_{\mathrm{T}}|\hat{O}|\Psi_{\mathrm{T}}\rangle + O(\varepsilon^2). \tag{2.47}$$

Applications and current challenges

Examples of applications. These methods generally scale efficiently with the number of electrons, but have a relatively large computer time requirement compared to other methods that scale the same. For instance, DMC scales as N^3, the same as density functional theory (see §2.2), but a reasonable run of DMC on a primitive cell of Si is roughly 100 times longer than the same for DFT with PBE. However, Monte Carlo methods are highly parallelizable, and well-suited for modern supercomputers [65, 90]. Thus, as systems of interest become more complex and supercomputers have gained more processors, quantum Monte Carlo algorithms have become important first-principles methods [89].

In the literature, there are benchmarks of the energies of atomic systems [110, 111, 112, 113], small molecules including transition metals [114, 115, 116, 117, 118], and large benchmark studies have been performed on the G1 set of molecules [119, 120] and the G2 set of molecules [121]. Atomic studies find agreement with experiments on order of 0.23 kcal/mol for ionization potentials, on order of 2.3 kcal/mol for electron affinity, and around 1-3 kcal/mol for atomization energies, depending on the accuracy of the trial wave function. They also find that DMC recovers 90-99% of the correlation energy, depending on the accuracy of the VMC starting point. Noncovalent interaction energies were found to agree with coupled-cluster calculations within 0.1 kcal/mol. In most cases, energy differences roughly within so-called chemical accuracy of 1 kcal/mol are attainable.

Diffusion Monte Carlo has also been studied in the context of solids [122, 105, 107, 123, 124, 41, 125]).

This includes a study of H_2O absorption on graphene, which was able to match the experimental water contact angle within statistical uncertainty [72] In FeO and NiO, DMC computes the matches experiment within a few percent in lattice constants, cohesive energy, and bulk modulus [126, 127, 122]. In MnO, DMC computed the correct ordering of two ZnO polymorphs, which is not always correctly predicted by methods such as density functional theory (§2.2) [128]. Several cuprate superconductors have been studied with FN-DMC, finding good agreement with experimental phonon frequencies, optical gaps, and effective exchange couplings [107, 123]. By studying different spin orderings, FN-DMC characterized the doped hole-doped ground state of a cuprate to be a spin polaron [124].

Current challenges. Although DMC scales relatively well with system size, the computational costs of simulating the small energy scales and large length scales required for a phenomenon such as superconductivity are still prohibitively large for the first-principles Hamiltonian [89]. Additionally, most experiments access quantities that depend on excited state properties, whereas diffusion Monte Carlo is primarily a ground-state method. Because DMC energies are variational, the error from incorrect nodes in the starting wave function can be variationally determined. However, it is difficult to know the precise magnitude of the error without a exact calculation as a reference.

Many of these issues can potentially be addressed using density matrix downfolding, described in §3.2. In that approach, the fixed-node error is not as important because eigenstates are not required. The method produces accurate effective models that may be solved to find excited state properties, and may be extended to larger length scales to probe additional properties. Density matrix downfolding has only recently been developed, and strategies for developing accurate models are still in development. In Chapter 9, I develop a new strategy for applying this approach to correlated electron systems.

The spectral function can also be computed by computing the real-time correlation function of the ground state. Because $e^{-\tau \hat{H}}$ is formally equivalent to evolving the system in imaginary time, by using analytic continuation [129], it is possible to compute the real-time correlation function from the trajectory during the projection process. However, the analytic continuation operation is numerically unstable to errors, and because these methods always generate some stochastic errors, the results can be very noisy [129].

2.1.6 Auxiliary-field quantum Monte Carlo

Auxiliary-field quantum Monte Carlo [68] is similar to DMC in that it utilizes imaginary-time propagation to extract properties of the ground-state wave function. It shares many of the strengths and weaknesses of DMC but with some important differences that I will discuss.

Basic definitions. AFQMC starts by expressing the Hamiltonian in a basis of single-particle orbitals,

such as plane-waves or Gaussian-type orbitals. Written in second-quantized notation:

$$\hat{H} = \hat{H}_1 + \hat{H}_2 = \sum_{ij} t_{ij} \hat{c}_i^\dagger \hat{c}_j + \sum_{ijkl} V_{ijkl} \hat{c}_i^\dagger \hat{c}_j^\dagger \hat{c}_k \hat{c}_l. \tag{2.48}$$

As discussed in §2.1.1, the ground state can be represented in the basis of determinants formed from Hartree-Fock orbitals, which are all mutually orthogonal. Similarly, the ground state of $\hat{H}$ can be written as a weighted sum of nonorthogonal determinants:

$$|\Psi_0\rangle = \sum_i \alpha_i |\Phi_i\rangle \qquad\qquad \langle \Phi_i | \Phi_j \rangle \neq \delta_{ij}, \tag{2.49}$$

where the orbitals are not from Hartree-Fock. The advantage of relaxing the condition of orthogonality is that the additional variational freedom can potentially reduce the number of determinants required to compute properties of the ground state. Another useful property of the subspace of nonorthogonal determinants is that for any determinant, $|\Phi\rangle$,

$$\hat{B}|\Phi\rangle = |\Phi'\rangle; \qquad\qquad \hat{B} = \exp\left\{ \sum_{ij} U_{ij} \hat{c}_i^\dagger \hat{c}_j \right\}, \tag{2.50}$$

where U is a square matrix, and $|\Phi'\rangle$ is another determinant which may not be orthogonal to $|\Phi\rangle$ [68]. Acting operators of the form $\hat{B}$ on any element in the subspace of nonorthogonal determinants does not leave that subspace.

The imaginary time propagator, $\hat{G} = e^{-\tau \hat{H}}$ from (2.35), can be transformed into a sum of integrals of operators in the form of $\hat{B}$ in (2.50) [68]. This is done using the Trotter break-up from §2.1.5 and a Hubbard-Stratonovich transformation. $e^{-\tau \hat{H}_1}$ in (2.48) is already of the form of $\hat{B}$. $\hat{H}_2 = \sum_{ijkl} V_{ijkl} \hat{c}_i^\dagger \hat{c}_j^\dagger \hat{c}_k \hat{c}_l$ can be expressed as:

$$\hat{H}_2 = \frac{1}{2} \sum_\gamma \lambda_\gamma \hat{v}_\gamma^2 \qquad\qquad e^{-\frac{\Delta\tau}{2} \lambda_\gamma \hat{v}_\gamma^2} = \int \frac{dx}{(2\pi)^{1/2}} e^{-\frac{1}{2}x^2} e^{x(-\Delta\tau \sum_\gamma \lambda_\gamma \hat{v}_\gamma)^{1/2}} \tag{2.51}$$

where $\hat{v}_\gamma$ are one-body operators, and the x is an auxiliary field from the Hubbard-Stratonovich transformation [68]. λ_γ and $\hat{v}_\gamma$ can be determined with various strategies, but for a general basis, it is possible to determine them via a Cholesky decomposition [68].

Like DMC in (2.20), the ground state energy can be computed using the mixed expectation value:

$$E_0 = \frac{\langle \Psi_{\mathrm{T}} | \hat{H} | \Psi_0 \rangle}{\langle \Psi_{\mathrm{T}} | \Psi_0 \rangle} = \frac{\int d\mathbf{x}_1 ... d\mathbf{x}_M \langle \Psi_{\mathrm{T}} | \hat{H} \prod_{i=1}^{M} \left[p(\mathbf{x}_i) \hat{B}(\mathbf{x}_i) \right] | \Psi_{\mathrm{T}} \rangle}{\int d\mathbf{x}_1 ... d\mathbf{x}_M \langle \Psi_{\mathrm{T}} | \prod_{i=1}^{M} \left[p(\mathbf{x}_i) \hat{B}(\mathbf{x}_i) \right] | \Psi_{\mathrm{T}} \rangle}, \tag{2.52}$$

where M is the number of time steps from the Trotter break-up, similar to DMC. $p(\mathbf{x}_i) \geq 0$ and $B(\mathbf{x}_i)$ take various forms depending on the form of the transformations, see Ref. [68] for examples. $|\Psi_{\mathrm{T}}\rangle$ is often a Slater determinant (although other forms are possible [68]), so that $\hat{B}(\mathbf{x}_1)...\hat{B}(\mathbf{x}_M)|\Psi_{\mathrm{T}}\rangle = |\Phi(\mathbf{x}_1, ..., \mathbf{x}_M)\rangle$, another Slater determinant. The algorithm will thus initialize walkers representing $|\Psi_{\mathrm{T}}\rangle$ in the basis of $\hat{H}$ in 2.48, evolve them by applying $\hat{B}(\mathbf{x}_i)$ and accumulating weights $p(\mathbf{x}_i)$, then average over the resulting determinants' overlap with $\langle \Psi_{\mathrm{T}}|$.

From this form it is clear that if $\langle \Psi_{\mathrm{T}} | \Phi(\mathbf{x}_1, ..., \mathbf{x}_M) \rangle < 0$ or complex for some $\mathbf{x}_1, ..., \mathbf{x}_M$, a problem similar to the sign problem in DMC will appear, as the walkers have signs or phases that average to zero due to symmetry [130]. Reminiscent of the fixed-node approximation, there is a **constrained path approximation** [131], which enforces $\langle \Psi_{\mathrm{T}} | \Phi(\mathbf{x}_1, ..., \mathbf{x}_M) \rangle$ to be the same sign or phase as $|\Psi_{\mathrm{T}}\rangle$. Unlike the fixed-node constraint, this approximation is not variational without additional computational effort [130]. The reason for this stems from the fact that determinants with positive overlap with $|\Psi_{\mathrm{T}}\rangle$ are not orthogonal to determinants with negative overlap with $|\Psi_{\mathrm{T}}\rangle$. This differs from FN-DMC: regions where Ψ_{T} changes sign represent orthogonal subspaces of configuration space.

Approximations. Many of the same approximations used in AFQMC are analogous to approximations in DMC. Timestep error, for example, appears due to the Trotter breakup of $\hat{H}_1$ and $\hat{H}_2$, and is extrapolated to zero similarly to DMC.

The constrained path approximation is significantly different from the fixed-node approximation in other ways, however [130]. For example, there are cases where the sign structure of $\langle \Psi_{\mathrm{T}} | \Phi(\mathbf{x}_1, ..., \mathbf{x}_M) \rangle$ can be incorrect, while AFQMC is still exact, including any noninteracting Hamiltonian and the one-band half-filled Hubbard model [130]. If non-variational estimates of the energy are used, parameters in Ψ_{T} cannot be variationally optimized. Instead, a self-consistent procedure can be utilized to reduce the dependence on the choice of trial wave function [132].

Examples of applications. AFQMC has computed accurate ground state properties for effective lattice Hamiltonians [84, 133, 134, 135], and it can be made exact for the half-filled Hubbard model [135]. AFQMC has also been applied to accurately determine the spectral function in lattice models [136]. It can also compute the fundamental gap in solids, for example Si, diamond, and ZnO, where it is within errorbars of experiment [137]. In NiO, the correct equilibrium volume was computed within AFQMC [138].

Current challenges. AFQMC faces many of the same challenges as DMC. Like DMC, AFQMC scales as N^3–N^4 [139]. Access to excited state properties is limited because it is fundamentally a ground state method. Access the to real-time dynamics through analytical continuation may require sophisticated techniques to control the error [136].

In addition to these issues, AFQMC has some additional issues that should be considered. When a Slater determinant is used as the trial function, it cannot satisfy the cusp conditions for the electron-electron interaction. This condition is usually satisfied in FN-DMC with the Jastrow factor, which expresses correlation in real space and generally cannot be expressed as a single determinant. The Hamiltonian of AFQMC is expressed in a single-particle orbital basis, which must be converged to the complete limit. FN-DMC operates in the complete basis set limit. Despite these additional considerations, while not guaranteed, in many cases AFQMC can achieve more accurate results than FN-DMC [130].

2.2 Density functional theory

Rather than computing the correct many-body wave function, Density functional theory (DFT) focuses on computing the correct ground state density of the many-body Schrödinger equation. This is a dramatic simplification: compared to the $3N$-dimensional eigenstates, the density of a system of N electrons is always a 3-dimensional function, $n(\mathbf{r})$. The excellent balance of efficiency and accuracy of density functional theory has made it an essential component of first-principles methodology.

2.2.1 Hohenberg-Kohn existence theorem and Kohn-Sham density functional theory

The foundation of DFT is the Hohenberg-Kohn theorems [140, 141]. They guarantee that the ground state density, $n_0(\mathbf{r})$ is sufficient to determine all properties of a system. They also prove the existence of a functional $F[n(\mathbf{r})]$ such that $F[n(\mathbf{r})] \geq E_0$ and $F[n(\mathbf{r})] = E_0$ if and only if $n(\mathbf{r}) = n_0(\mathbf{r})$. The exact form of this functional is unknown and still an area of active research [2, 142]. Nonetheless, the existence of the exact functional has motivated many approximate energy functionals, and variationally optimizing electron densities for a given functional has lead to the broadly successful method known as DFT.

Although the total functional $F[n(\mathbf{r})]$ is unknown, practical approximations have been developed through Kohn-Sham density functional theory. Kohn-Sham DFT posits that the ground state density can be computed as the ground state density of an auxiliary noninteracting model with some effective potential $V_{\text{eff}}(\mathbf{r})$. There is no general guarantee that this is true, but it nonetheless motivates some useful approximations. The

problem of approximating the exact energy functional, $F[n(\mathbf{r})]$ is converted to finding an accurate effective potential, $V_{\text{eff}}(\mathbf{r})$.

The Hartree-Fock effective potential, $V_{\text{eff}}^{\text{HF}}(\mathbf{r})$ from (2.2), is one possible functional, but because a Slater determinant cannot represent the ground state in every interacting system, it is clear that some modification is necessary. The kinetic energy, Hartree potential, and external (ionic) potential in $V_{\text{eff}}^{\text{HF}}(\mathbf{r})$ represent large contributions to the energy. Let $V_{\text{eff}}(\mathbf{r}) = V_{\text{ion}}(\mathbf{r}) + V_{\text{Hartree}}(\mathbf{r}) + V_{\text{xc}}(\mathbf{r})$, where $V_{\text{xc}}(\mathbf{r})$ is to correct the final energy for exchange and correlation effects. Because the long-range interactions are accounted for by $V_{\text{ion}}(\mathbf{r})$ and $V_{\text{Hartree}}(\mathbf{r})$, it is reasonable to approximate $V_{\text{xc}}(\mathbf{r})$ as a function that depends on the density or derivatives of the density at $\mathbf{r}$ [143]. This is the origin of many well-known DFT functionals. The local density approximation (LDA) approximates $V_{\text{xc}}(\mathbf{r}) = v_{\text{LDA}}(n(\mathbf{r}))$ as the same as the homogeneous electron gas at density $n(\mathbf{r})$. The $v_{\text{LDA}}(\mathbf{r})$ for the homogeneous electron gas was fit to diffusion Monte Carlo calculations performed by David Ceperley and Berni Alder in 1980 [144]. The family of GGA functionals add a dependence on the gradients of the density to the LDA, and are either fit to other sources of data [145, 2] or made to satisfy exact theoretical constraints, as in the PBE functional [146]. Collecting these pieces together, the auxiliary Hamiltonian is

$$(\hat{T} + V_{\text{eff}}(\mathbf{r}))\phi_{\sigma_i,i}^{\sigma}(\mathbf{r}) = \varepsilon_i^{\sigma}\phi_{\sigma_i,i}(\mathbf{r}) \tag{2.53}$$

$$V_{\text{eff}}(\mathbf{r}) = -\frac{1}{2}\nabla^2 + V_{\text{ext}}(\mathbf{r}) + \sum_{j,\sigma_j}\int d\mathbf{r}'\frac{\phi_{\sigma_j,j}^{*}(\mathbf{r}')\phi_{\sigma_j,j}(\mathbf{r}')}{|\mathbf{r}-\mathbf{r}'|} + V_{\text{xc}}(\mathbf{r}) \tag{2.54}$$

Hybrid functionals average the exchange approximation from a DFT functional, $V_{\text{x}}(\mathbf{r})$, with the exchange potential from the Hartree-Fock equations (2.2). For example, the PBE0 hybrid functional [147] is $V_{\text{xc}}^{\text{PBE0}}(\mathbf{r}) = V_{\text{c}}^{\text{PBE}}(\mathbf{r}) + 0.75V_{\text{x}}^{\text{PBE}}(\mathbf{r}) + 0.25V_{\text{x}}^{\text{HF}}(\mathbf{r})$, with $V_{\text{x}}^{\text{HF}}(\mathbf{r})$ representing the exchange term in the $V_{\text{eff}}^{\text{HF}}(\mathbf{r})$. The exchange potential is no longer a local functional of the density, and in practice, computing this exchange term requires significantly more computational effort. Hybrid functionals are often much more accurate than the local functionals they are based on [142], and this is often attributed to the cancellation of **self-interaction error** [148]. This error is best illustrated by a system with one electron, which has nonzero Hartree interaction energy despite there being no two electrons to interact. In Hartree-Fock the exchange term exactly cancels the self-interaction error, and hence, mixing some Hartree-Fock exchange can improve the results in DFT.

One critical difference from Hartree-Fock is that $V_{\text{xc}}(\mathbf{r})$ must be chosen for the calculation. The **Kohn-Sham orbitals**, which are the one-body solutions to the Kohn-Sham equations (2.53), are commonly used to form the orbital set for the Slater-type part of $\Psi_{\text{T}}(\mathbf{R})$ in QMC calculations. In this dissertation, $V_{\text{xc}}(\mathbf{r})$

is chosen by variationally optimizing the energy for a QMC run using these orbitals as input. There is no variational principle for comparing DFT functionals within DFT, and choosing the $V_{\text{xc}}(\mathbf{r})$ approximation is sometimes treated similarly to a free parameter for performing DFT calculations [142, 145, 149, 150].

2.2.2 The Kohn-Sham Hamiltonian: its usage and its theoretical meaning

The eigenvalues and eigenvectors of the Kohn-Sham Hamiltonian (2.53) are used extensively to interpret material properties, as well as used for constructing many-body wave functions for further use. Band structures from DFT are simply the eigenvalues of the Kohn-Sham Hamiltonian and are compared to experiments. For example, DFT band structures are compared to density of states measurements from angle-resolved photoemission spectroscopy (ARPES) [40, 39]. The ground state energy can be used to calculate structural properties, such as the formation energy [149]. Forces from DFT can be used for crystal structure optimization [151, 152]. The determinant of Kohn-Sham eigenstates is a valid many-body wave function in the Hilbert space of $\hat{H}$, and thus can be used as components in trial functions for first-principles QMC [89]. The Kohn-Sham determinant is also used to compute observables such as densities [41, 142], or even topological quantities such as the polarization [153] or the Chern number [154].

It is important to understand what theoretical basis exists for these interpretations. If the Kohn-Sham *ansatz* is correct and the $V_{\text{xc}}(\mathbf{r})$ is exact, then the Hohenberg-Kohn theorem implies that the ground state density and ground state energy for a given crystal structure are exact. In this circumstance, observables directly accessible from the energy and the density are also exact, such as the forces on the atoms used for a structure optimization. However, even in this hypothetical circumstance, all properties derived from the Kohn-Sham determinant or Kohn-Sham eigenvalues will have no guarantee of accuracy. Properties like band structures and polarization have no guarantee of accuracy *even in this exact case* [143]. The only guarantee of the Kohn-Sham auxiliary Hamiltonian is that it produces the exact ground-state density of the system.

One way of interpreting the solutions to the Kohn-Sham Hamiltonian is by viewing the Kohn-Sham Hamiltonian as an effective noninteracting model. Studying properties of Kohn-Sham eigenvalues or orbitals is studying the properties of solutions to this model, rather than solutions to the true Hamiltonian, $\hat{H}$. The Kohn-Sham bands represent the energy of singles excitations: $\hat{c}_k^\dagger \hat{c}_q |\Phi_{\text{KS}}\rangle$, keeping all orbitals fixed, where $\Phi_{\text{KS}}(R)$ is the determinant of Kohn-Sham orbitals and energy is measured using $\hat{T} + V_{\text{eff}}(\mathbf{r})$. The Kohn-Sham model can be remarkably accurate in many cases, particularly simple metals and insulators. The model naturally breaks down when where correlation effects are important and incorrectly modeled by $V_{\text{xc}}(\mathbf{r})$ [89], such as in systems with localized d or f electrons.

Note that when a DFT band structure does not match experimental electron dispersion, the source of the

discrepancy is not always clear. The inaccuracy of DFT band structure is sometimes interpreted to mean the system is "strongly correlated," [39] meaning that no noninteracting model exists that can describe the system [155]. However, inaccuracy of DFT with a given $V_{\text{xc}}(\mathbf{r})$ is only the statement that a particular noninteracting model is not accurate: the Kohn-Sham model for the system. Instead, some downfolding methods may address whether any good noninteracting model exists, such as the method described in §3.2.

2.2.3 Example applications and current challenges

Examples of applications. Density functional theory is by far the most commonly used method for first-principles calculations. The method boasts a large set of successes, particularly in semiconductors and simple metals [33], and has been applied to large numbers of materials [156] and used to predict the existence of new materials [157]. It is used to fit classical potentials for classical simulations of molecular dynamics [158]. Besides this direct use, it is commonly used to generate the starting point for other methods. For instance, DFT can generate part of the initial wave function which are optimized though first-principles quantum Monte Carlo methods [89]. The GW method (see §2.3.1) often uses DFT to provide the initial density and Green function. LDA+DMFT utilizes DFT to provide an approximate local Hamiltonian to solve [159]. Additionally, other methods almost always compare to DFT to measure their accuracy and computational efficiency.

DFT has been applied to essentially every material that has been studied with first-principles methods. I focus on a few examples of correlated electron materials, as this is the main focus of this dissertation. In VO_2, standard density functionals incorrectly finds a metallic state for the ground state in the low-temperature structure [160]. In MnO, FeO, CoO, and NiO, DFT errors using GGA to calculate the gap are approximately 70% of the experimental values or else completely gapless [161]. Magnetic moments from several DFT functionals were in reasonable agreement for MnO and FeO but too small by roughly 20% of experiment [161]. In the cuprates, properties such as the gap are sensitive to the exchange correlation functional, and common functionals do not compute accurate phonon spectra [162, 163, 164, 107]. In the context of iron-based superconductors, spin-unpolarized LDA can achieve the qualitatively correct Fermi surface topology, but the magnitude of the band width is a factor of 4 to 16 too large, depending on the band [39].

Current challenges. The form of $V_{\text{eff}}(\mathbf{r})$ must be chosen, and there is no way to determine the accuracy of one approximate form verses another without appealing to experiment or other calculations. This ambiguity is sometimes dealt with by choosing simple or commonly-used functionals from the literature [165]. Other times, functional choices may be fit to experimental results and then used in similar systems [149,

145, 32]. Recently, it has been shown that fitting experimental energies too closely can lead to incorrect predictions for the ground state density [142]. As discussed above, the results are sometimes sensitive to the choice in functional, so for simple properties like energy gaps, the results can be tuned by trying many functionals and choosing the desired result.

Because the Kohn-Sham equations have no theoretical grounding as an approximation to the system, properties derived from the band structures of DFT are often unreliable [143]. This is some part of the reason DFT is known to predict incorrect band gaps, band widths, effective masses, and other properties reliant on the Kohn-Sham equations being an accurate representation of the system.

2.3 Diagrammatic methods

Diagrammatic methods solve a simplified Hamiltonian exactly and compute properties of the first-principles Hamiltonian as corrections to the these results. They tend to focus on the single-particle Green function, $G(x_1, x_2) = \langle \Psi | T[c(x_1)c^\dagger(x_2)] | \Psi \rangle$, where $x_i = (t_i, \mathbf{r}_i)$ are time and space coordinates, $|\Psi\rangle$ is the ground state of the system, $T[\cdot]$ denotes that $t_1 < t_2$. Assume the Hamiltonian can be written $\hat{H} = \hat{H}_0 + \hat{H}_{\text{hard}}$, where $\hat{H}_0$ is solvable, and its Green function is G_0. G, the Green function for $\hat{H}$, can be written as a correction to G_0 in a Dyson equation [166]:

$$G(\omega) = (G_0(\omega)^{-1} + \Sigma(\omega))^{-1} \implies G(\omega) = G_0(\omega) + G_0(\omega)\Sigma(\omega)G(\omega) \tag{2.55}$$

$\Sigma(\omega)$ is called the **self energy** and ω is the frequency. Once the Green function and self energy are approximated closely enough, properties such as response functions or the spectral function can be computed from them [167]. One advantage of diagrammatic approaches is that they can access these experimentally relevant quantities.

When the solvable Hamiltonian is a noninteracting Hamiltonian, G_0 is the Green function for a system of noninteracting electrons, which is known [4]. In this case, (2.55) is formally equivalent to solving Hedin's

equations [4]:

$$\Sigma_{\rm xc}(x_1,x_2) = \int d^4x_3 d^4x_4 \; iG(x_1,x_4)W(x_1,x_3)\Gamma(x_4,x_2,x_3) \tag{2.56}$$

$$W(x_1,x_2) = V_c(x_1-x_2) + \int d^4x_3 d^4x_4 \; v_c(x_1,x_3)P(x_3,x_4)W(x_4,x_2) \tag{2.57}$$

$$P(x_1,x_2) = -i\int d^4x_3 d^4x_4 G(x_1,x_3)G(x_4,x_1)\Gamma(x_3,x_4,x_2) \tag{2.58}$$

$$\Gamma(x_1,x_2,x_3) = \delta(x_1-x_2)\delta(x_1-x_3) + \int d^4x_4 d^4x_5 d^4x_6 d^4x_7 \frac{\delta\Sigma_{\rm xc}(x_1,x_2)}{\delta G(x_4,x_5)} G(x_4,x_6)G(x_7,x_5)\Gamma(x_6,x_7,x_3) \tag{2.59}$$

$$G(x_1,x_2) = G_0(x_1,x_2) + \int d^4x_3 d^4x_4 \; G_0(x_1,x_3)\Sigma(x_3,x_4)G(x_4,x_2) \tag{2.60}$$

where $x_i = (\mathbf{r}_i, t)$ represent space-time coordinates, $\Sigma(x_1,x_2) = V_{\rm Hartree}(\mathbf{r}_1-\mathbf{r}_1)+\Sigma_{\rm xc}(x_1,x_2)$ and $V_{\rm Hartree}(\mathbf{r}) = \int d^3\mathbf{r}' \; n(\mathbf{r}')/|\mathbf{r}-\mathbf{r}'|$. Hedin's equations break the problem down into parts that have physical interpretations: W represents the screened interaction potential, P represents the polarizability, and $\Sigma_{\rm xc}$ represents the part of the self-energy due to exchange and correlation effects. These integral equations can be diagrammatically represented using Feynman diagrams, as represented in Fig. 2.3. Γ is referred to as a vertex because it connects a polarization line with two Green function lines in the corresponding diagram.

Hedin's equations (2.56–2.60) each depend on a quantity specified by another equation. The strategy is generally to make an approximation to some of the quantities and use the equations to compute the other quantities. The equations can be made self-consistent by using the equations to compute the first approximated quantities, and continue doing so in a loop until the quantities no longer change.

2.3.1 GW approximation

Basic definitions. To make the problem soluble, the GW approximation assumes $\Gamma = \delta(x_1-x_2)\delta(x_2-x_3)$ in (2.59). This implies the equation for the polarizability becomes $P(x_1,x_2) = -iG(x_1,x_2)G(x_2,x_1)$. This is equivalent to making the **random phase approximation (RPA)** [168, 169, 170] for the reducible polarizability [4]. The self energy (2.56) becomes $\Sigma_{\rm xc}(x_1,x_2) = iG(x_1,x_2)W(x_1,x_2)$, which is the origin of the name **GW approximation**. Now, starting with an approximate form for the Green function, such as the Green function from the Kohn-Sham equations of a DFT calculation, the method can (a) calculate the polarization from $P(x_1,x_2) = -iG(x_1,x_2)G(x_2,x_1)$; (b) calculate the screened interaction from (2.57); (c) calculate self-energy from $\Sigma_{\rm xc}(x_1,x_2) = iG(x_1,x_2)W(x_1,x_2)$. Stopping here is known as **one-shot GW**, sometimes referred to as G_0W_0. Calculating G from (2.60) and continuing until reaching self-consistency is known as **self-consistent GW**. Other more intricately defined levels of self-consistency are also used, for

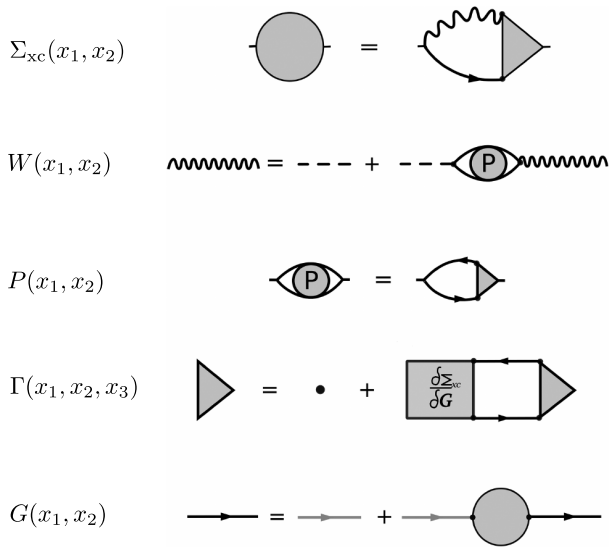

Figure 2.3: Feynman diagrams representing Hedin's equations (2.56–2.60). Image from Ref. [4].

example **quasi-particle self-consistent GW (QSGW)** [171].

Approximations. Approximating the irreducible polarizability using the RPA is an uncontrolled approximation. It is equivalent to taking a non-interacting approximation to the electron-hole correlation function [172]. The RPA has been successful in computing long-range optical plasmonic properties [173], such as in graphite [174] and graphene [175]. However, in some systems, electron-hole correlations are significant, such as LiH, where the predicted RPA optical spectrum differs significantly from experiment. [176]. Corrections to this approach are normally termed **vertex corrections**, and commonly utilize the Bethe-Salpeter equation to incorporate electron-hole interactions. [177, 178].

Stopping before reaching self-consistency implies that Hedin's equations are not correctly solved. Counterintuitively, this usually results in *more accurate* results compared to experiment, as discussed below. This also means one-shot GW may have a significant dependence on the DFT functional used to produce the initial Green function [179].

Examples of applications. The one-shot GW and QSGW approximations have achieved most notable success in describing quasi-particle excitations in main-group semiconductors and insulators. In Si, Ge, and LiCl, one-shot GW computes the fundamental gap within 5% of the experiment, a dramatic improvement over the LDA starting point which is used (errors range from from 30% to 90% of experiment, all underestimated) [180]. In *s*- and *p*-electron compounds, one-shot GW generally finds quasiparticle gaps to within a few tenths of an eV of experiment, while QSGW can improve the agreement further [171]. Interestingly,

there are some cases where a QSGW results gets worse results, for example diamond in Ref. [171]. When combined with vertex corrections from the Bethe-Salpeter equation, GW can reproduce optical absorption peaks in $MoSe_2$ and WSe_2 within roughly 0.02 eV [181]. One-shot GW can reproduce the optical spectrum of Si near the Fermi level as well, but fails to describe the plasmon peak structures without further vertex corrections [182]. On the other hand, partially self-consistent GW can reproduce the spectrum of VO_2 reasonably well, including a sharp plasmon peak near 1.3 eV [183] which is also seen in experiment at 1.2 eV [184].

Achieving full self-consistency is rarely done in practical calculations, in part due to the computational expense, and in part because results may become less accurate [185, 186]. For example, in the homogeneous electron gas, fully self-consistent GW achieves the most accurate ground state energy, but more inaccurate quasiparticle lifetime and quasiparticle dispersion [58]. This is attributed to the error of the vertex approximation becoming more significant as the self-consistent loop proceeds [186, 178].

In other transition metal materials, use of non-fully-self-consistent GW is problematic due to sensitivity of the starting point. Gaps in transition metal oxides exhibit errors of 10-30%, and are more sensitive to the approximations in GW [187]. In Fe_2O_3, the band gaps are sensitive to the level of self-consistency and the kind of density functional theory used for the starting Green function [179]. In MnO, FeO, CoO, and NiO, DFT errors using GGA to calculate the gap are more approximately 70% of the experimental values or else completely gapless. One-shot GW starting from these wave functions only reduces the error to roughly 50% of the experimental result or more and fails to open a gap in the gapless states [161].

Current challenges. Given the mixed successes and failures of the GW approximation, it is clear that it is difficult to predict when RPA will be a sufficient approximation for transition metal systems. Non-fully-self-consistent GW also inherits much of the uncertainty of choosing the DFT exchange-correlation potential, because the results are sensitive to this choice, and again, there is no procedure for choosing $V_{\text{eff}}(\mathbf{r})$ independently of experiment. Fully self-consistent GW is often less accurate than one-shot GW, and vertex corrections that can alleviate it problems are computationally complex and are also not guaranteed to be sufficient.

2.3.2 Dynamical mean field theory

Intuitively, the difficulty of GW in transition metal systems can be traced back to the derivation of (2.55). If $\hat{H}_{\text{hard}}$ contains many large terms, then $\Sigma(\omega)$ is difficult to approximate because it makes significant changes to the noninteracting Green function [188]. For electrons inside the d shells of a transition metal, interactions with other electrons are important. The concept behind single-site DMFT is to make the solvable

Hamiltonian, $\hat{H}_0$, the d and/or f shells of one atom, which is small enough to solve with numerically exact methods. The states outside this single site are considered as a bath, and are treated as noninteracting states. The Σ_{aux} for this single-site calculation is used to approximate the Σ for the one-particle Green function.

Basic definitions. In practice, DMFT is usually applied to downfolded lattice-Hamiltonians, so to simplify discussion, I will assume an accurate lattice model has been determined for the system.

Starting with (2.55), in the case when G_0 is the non-interacting Green function, $(\omega - \varepsilon_k)^{-1}$, then the Dyson equation takes the from [188]

$$G_k(\omega) = [\omega - \varepsilon_k - \Sigma_k(\omega)]^{-1}. \qquad G_i(\omega) = \frac{1}{N_k}\sum_k G_k(\omega) \tag{2.61}$$

where G_i is the green function of a single site, computed by averaging over the k-dependent single-particle Green functions. Single-site DMFT makes two approximations to evaluate Σ_k for this equation: (a) $\Sigma_k(\omega)$ is restricted to matrix elements between orbitals on a single site only, e.g. has no k dependence; (b) $\Sigma(\omega)$ is the same as the $\Sigma_{\text{aux}}(\omega)$ of the orbitals interacting on a single site and coupled to a bath. Different levels of approximation in DMFT occur depending on the type of auxiliary system defined, for instance, how many orbitals are included on the site and in the bath.

The method enters a self-consistent loop wherein an approximate form for Σ is guessed (e.g. $\Sigma = 0$), the auxiliary system is solved using exact diagonalization or accurate quantum Monte Carlo techniques, Σ_k for the lattice is approximated as Σ_{aux} from the calculation, G_k solved using (2.55), the bath is updated in the auxiliary system, and so on until self-consistency [188].

Approximations. There are at least three important approximations in single-site DMFT: the k-independent $\Sigma_k(\omega)$ replacement, the calculation of Σ_{aux}, and the lattice model or method of localization. The k-independence can be improved by **cluster DMFT**, which extends this idea to auxiliary systems with multiple sites [159]. The calculation of $\Sigma_{\text{aux}}(\omega)$ depends on, for example, the number of bath states included. If the number of bath states increases until it matches the full Hilbert space of the system, this error will also go to zero.

To make an accurate separation of $\Sigma(\omega)$ into matrix elements between sites and on a single site, usually some downfolding approach is required to derive accurate effective interactions that are short-ranged [159]. Discussion of this technique and the errors inherent in it is left to Chapter 3. However, it is relevant to this discussion that a **double-counting correction** is added to compensate for errors in the cRPA downfolding method. Similar to the exchange-correlation functional in DFT, this correction must be chosen based on

some external input, and it is often chosen to better match with experiment [189, 190].

Examples of applications. DMFT has been applied broadly to materials with d and/or f electrons. In metallic iron and nickel, it successfully reproduces the temperature dependence of the magnetic moment and magnetic susceptibility [191]. In the iron-based superconductors, DMFT has been broadly able to reproduce spectra of ARPES, and has characterized the importance of Hund's coupling in describing the multi-orbital physics of the iron atoms [192, 193, 194, 195]. In these systems, a Hund's coupling, J, is required, and generally needs to be estimated from agreement with experiment. In $SrRuO_3$ and $CaRuO_3$, DMFT calculations were performed using parameters that were chosen such that the resulting DMFT calculation gave reasonable agreement with experiment, then the resulting model was used to interpret the materials [196, 197]. The main result was that strong Hund's coupling was important for an adequate description of the material. In $SrMnO_3$ and $LaNiO_3$, the results were again somewhat sensitive to parameter choices for the model, but with the correct selection of parameter, the experimental spectrum was reproduced [198, 190]. In the heavy-fermion material, $CeIrIn_5$, the DMFT calculations fit to an LDA-downfolded model was able to reproduce the magnetic part of the resistivity vs. temperature and the de Haas-van Alphen frequencies [199]. The effective masses from DMFT were found to be on order of 1000 times the effective mass predicted by the LDA bands used to build the model.

There are also cases where single-site DMFT is insufficient to describe the correlations. In VO_2, with single-site DMFT an insulating low-temperature state only appears when U is increased to unphysically high levels, however a cluster of two sites was able to capture the insulating phase [200]. Describing d-wave superconductivity in the cuprates also requires a cluster expansion [201, 202].

Current challenges. From many of the examples, it is clear that a large uncertainty of this method is due to difficulty in downfolding models of transition metal systems using DFT alone. Even when parameters are not chosen outright to match experiment, the double-counting correction functions similarly to adjusting free parameters in a model. When adjusting free parameters in this way, it remains unclear if the resulting model is truly a faithful representation of the system: whether is it is unique and whether it can extrapolate to all the systems or properties it is supposed to describe.

Uncertainty in the double-counting correction can be eliminated using GW, but as discussed in §2.3.1, it is unclear that GW can give a proper description of transition metals, particularly beyond quasiparticle spectra. Haule has also proposed a method of removing double-counting corrections, but nonetheless requires defining a set of projectors to localize the effective interactions, and needs to be converged to a basis-independent limit [203].

Because the exact calculation of $\Sigma_{\text{aux}}(\omega)$ requires exponentially scaling methods, it is usually difficult to

go beyond just a few sites. This makes it difficult to converge the approximation to the cluster size and the size of the bath. Correlations that extend more than a few sites will be nearly impossible in this approach, and these correlations need to be treated with a different approximate approach, for instance, GW [159].

2.4 Pseudopotential approximation

Several of the methods presented here benefit from approximating the Hamiltonian by a pseudopotential. Pseudopotentials allow for more accurate treatment of the valence electrons of heavier atoms by removing core electrons and adjusting the potential to compensate. Rewriting the first-principles equation (1.1),

$$H = \frac{1}{2}\sum_i \nabla_i^2 + \sum_{ij}\frac{1}{|\mathbf{r}_i - \mathbf{r}_j|} + \sum_{iI} V_{\text{ext}}(\mathbf{r}_i - \mathbf{a}_I), \tag{2.62}$$

where r_i are electron coordinates and a_I are nuclei coordinates. In the **all-electron** case,

$$V_{\text{ext}}(|\mathbf{r}_i - \mathbf{a}_I|) = \sum_{i,I}\frac{Z_I}{|\mathbf{r}_i - \mathbf{a}_I|}, \tag{2.63}$$

where Z_I is the atomic number of the ion, and all the electrons in the material are simulated. We employ pseudopotentials from M. Burkatzki, C. Filippi, and M. Dolg (**BFD pseudopotentials**) [204, 205], which are of the form:

$$V_{\text{ext}}(\mathbf{r}_i - \mathbf{a}_I) = V_{\text{loc}}(|\mathbf{r}_i - \mathbf{a}_I|) + \sum_{l=0}^{l_{\max}} V_l(|\mathbf{r}_i - \mathbf{a}_I|)\hat{P}_{l,I}, \tag{2.64}$$

where $\hat{P}_{l,I}$ projects the wave function onto the spherical harmonics of degree l on each atom I. The form of V_{loc} and V_{l} are

$$V_{\text{loc}}(r) = -\frac{Z_I^{\text{eff}}}{r} + \frac{Z_I^{\text{eff}}}{r}e^{-\alpha r^2} + \frac{Z_I^{\text{eff}}}{r}\alpha r e^{-\beta r^2} + \gamma e^{-\delta r^2}, \qquad V_l(r) = \zeta e^{-\eta r^2}. \tag{2.65}$$

$Z_I^{\text{eff}} = Z_I - Z_I^{\text{core}}$ where Z_I^{core} is the number of electrons removed from the calculation. All Greek letters are parameters that are optimized for a given atom. In the case of BFD, they are optimized to match energies of configurations within Hartree-Fock, which is accurate for core electrons, where kinetic and ionic potential energy contributions dominate the correlation energy. In the limit that $r \to 0$, the potential behaves quadratically, which eases numerical difficulties of representing the wave function near the nucleus [204]. The resulting pseudopotentials are benchmarked by comparing atomic spectra, molecular binding energies,

and vibrational frequencies with correlated-electron methods [204, 205]. Other benchmarks show that when compressing bonds sufficiently much, the accuracy of this approach may break down, but for the ranges of bond lengths of interest to us, the pseudopotential is very accurate compared to experiment and all-electron CCSD(T) [206, 207].

The accuracy of the pseudopotentials for quantum Monte Carlo depends on the number of electrons removed from the calculation [206]. We utilize "small core" pseudopotentials for transition metals, which generally keeps one full shell of electrons which are lower energy than the valence shell. For example, in iron, we keep $3s^2 3p^6 4s^2 5d^6$, with $Z_{\text{eff}} = 16$, and so each iron contributes 16 electrons to the system in the neutral case.

In the case that $V_l(r) \neq 0$, then $E_{\text{L}}(\mathbf{R})$ of §2.1.4 and §2.1.5 depends on the wave function value in more than a single point. In VMC, this can be handled as explained in §2.1.4, with an additional integral over electron coordinates. In diffusion Monte Carlo, §2.1.5, this can cause a complication in (2.24) when computing $\langle R_i | e^{\hat{V}_l} | R_{i+1} \rangle$, which may be negative. Even if $\Psi_{\text{T}}(\mathbf{R}_1)\Psi_{\text{T}}(\mathbf{R}_M) \geq 0$, $W(\{\mathbf{R}_i\})$ may change sign. This can be handled using the localization approximation [208], which is non-variational, or T-moves [209], which is variational but increases timestep error.

2.5 Supplemental information: Hartree-Fock equations

Let $\langle R|\Phi\rangle = \text{Det}\left([\phi_i(r_j)]\right)$. I suppress spin degree of freedom for simplicity.

I approach it via the method of Lagrange multipliers. I vary the $\phi_i^*(r)$ subject to the constraints $\langle \phi_i | \phi_i \rangle = 1$. Basic theory of Lagrange multipliers within functional analysis implies that if

$$\frac{\delta \langle \Phi | \hat{H} | \Phi \rangle}{\delta \phi^*} - \sum_i \varepsilon_i \frac{\delta \langle \phi_i | \phi_i \rangle}{\delta \phi^*} = 0, \tag{2.66}$$

then the energy of $|\Phi\rangle$ is minimized subject to the normalization constraint. ε_i are the Lagrange multipliers, but can be interpreted as the orbital energies. Evaluating the functional derivative,

$$\frac{\delta \langle \Phi | \hat{H} | \Phi \rangle}{\delta \phi^*} = \sum_i \int dr \delta\phi_i^*(r) \left(\hat{T} + V_{\text{ext}}(r) \right) \phi_i(r) \tag{2.67}$$

$$+ \frac{1}{2} \sum_{ij} \int dr dr' \frac{\delta\phi_i^*(r)\phi_j^*(r')\phi_i(r)\phi_j(r')}{|r - r'|} + \frac{1}{2} \sum_{ij} \int dr dr' \frac{\phi_i^*(r)\delta\phi_j^*(r')\phi_i(r)\phi_j(r')}{|r - r'|} \tag{2.68}$$

$$- \frac{1}{2} \sum_{ij} \int dr dr' \frac{\delta\phi_i^*(r)\phi_j^*(r')\phi_j(r)\phi_i(r')}{|r - r'|} - \frac{1}{2} \sum_{ij} \int dr dr' \frac{\phi_i^*(r)\delta\phi_j^*(r')\phi_j(r)\phi_i(r')}{|r - r'|} \tag{2.69}$$

The right side two-body terms are identical to the left side up to renaming the summation index and

integration variables.

$$\frac{\delta\langle\Phi|\hat{H}|\Phi\rangle}{\delta\phi^*} = \sum_i \int dr\delta\phi_i^*(r)\left(\hat{T}+\hat{V}_{\text{ext}}\right)\phi_i(r) \tag{2.70}$$

$$+\sum_{ij}\int drdr'\frac{\delta\phi_i^*(r)\phi_j^*(r')\phi_i(r)\phi_j(r')}{|r-r'|} - \sum_{ij}\int drdr'\frac{\delta\phi_i^*(r)\phi_j^*(r')\phi_j(r)\phi_i(r')}{|r-r'|} \tag{2.71}$$

$$= \sum_i \int dr\delta\phi_i^*(r)\left\{\left(\hat{T}+\hat{V}_{\text{ext}}\right)+\sum_j\int dr'\frac{\phi_j^*(r')\phi_i(r)\phi_j(r')}{|r-r'|} - \sum_j\int dr'\frac{\phi_j^*(r')\phi_j(r)\phi_i(r')}{|r-r'|}\right\} \tag{2.72}$$

Thus,

$$\sum_i \int dr\delta\phi_i^*(r)\left\{\left(\hat{T}+\hat{V}_{\text{ext}}\right)\phi_i(r)+\sum_j\int dr'\frac{\phi_j^*(r')\phi_i(r)\phi_j(r')}{|r-r'|} - \sum_j\int dr'\frac{\phi_j^*(r')\phi_j(r)\phi_i(r')}{|r-r'|} - \varepsilon_i\phi_i(r)\right\} = 0 \tag{2.73}$$

Since $\delta\phi_i^*(r)$ is arbitrary, the term in the brackets must be zero for all i. These are the Hartree-Fock equations.

Chapter 3

State-of-the-art in downfolding the first-principles Hamiltonian

Access to accurate model Hamiltonians would generally improve many of the methods discussed in §2. The computational requirements of exact diagonalization, CCSD, AFQMC, DMRG, and DMFT all grow with the size of a single-particle basis set used to express the many-body Hilbert space. Smaller basis sets may be possible if interaction parameters are adjusted to account for basis elements left out of the calculation. If these adjusted interactions are short-ranged, several of the methods will also be more efficient. For example, matrix product states are easier to evaluate for Hamiltonians with short-range operators [77]. In DMFT, interactions extending farther than a single site require a cluster calculation, which is much more computationally costly [159]. Although the first-principles Hamiltonian electrons interact with a relatively long-range Coulomb potential, lattice models with short-range interactions can sometimes be a good approximation [210]. The best form for the interactions and how accurate they are is often unclear.

Besides these practical considerations, knowing the types of effective models and their parameters often provides a clear, concise, and intuitive description for a system. For example, if a material is accurately described by a Heisenberg model,

$$\hat{H}_{\text{eff}} = J \sum_{\langle ij \rangle} \hat{S}_i \cdot \hat{S}_j, \tag{3.1}$$

and $J < 0$, it is clear that the material should be a ferromagnet, and the magnitude of J sets the energy scale of the transition temperature.

The most commonly used downfolding approach is constrained-RPA [211, 200], which utilizes DFT to derive the model. Recently, I as well as other collaborators have developed and applied a method known as density-matrix downfolding, a downfolding approach utilizing wave-function based methods. Another technique known as **canonical transformations** has been applied to molecules with strong correlations [212, 213, 214, 215]. Canonical transformation approximately block-diagonalizes the Hamiltonian by applying unitary operator to reduce undesirable off-diagonal elements. After this process is complete, one block of the modified Hamiltonian represents the model of the system. The computational cost scales as N^6, similar

to coupled cluster. This makes application to solids difficult, so I will not go into further detail for this method.

3.1 Constrained-RPA

Basic definitions. **Constrained-RPA (cRPA)** is a modification of the RPA approach for computing the screened interaction, W, in (2.57), where only part of the space is traced out. In the RPA, $P(x_1, x_2) = -iG(x_1, x_2)G(x_2, x_1)$. If the Green functions are approximated by the DFT Kohn-Sham system, then

$$P(r_1, r_2, \omega) = \sum_i^{\text{occ}} \sum_j^{\text{unocc}} \phi_i(r_1)\phi_i^*(r_2')\phi_j(r_1)\phi_j(r_2') \left\{ \frac{1}{\omega - \varepsilon_j + \varepsilon_i} - \frac{1}{\omega + \varepsilon_j - \varepsilon_i} \right\} \tag{3.2}$$

where $\phi_i(r)$ and ε_i are the Kohn-Sham orbitals and energies [216, 4]. The "constraint" is that the sums over the occupied orbitals, $\sum_i^{\text{occ}}$, and unoccupied orbitals, $\sum_i^{\text{unocc}}$, does not extend over the d or f orbitals on a site. The screened interaction, W (2.57), is computed from this modified polarization calculation. This is used to determine an effective Hamiltonian of the form

$$\hat{H}_{\text{eff}} = \sum_{ij} t_{ij}\hat{c}_i^\dagger \hat{c}_j + \sum_{ijkl} V_{ijkl}\hat{c}_i^\dagger \hat{c}_j^\dagger \hat{c}_k \hat{c}_l.$$

A Wannier basis is constructed from the d-state DFT orbitals [216, 159], and interaction parameters for the Hamiltonian in this basis, V_{ijkl} is simply this W expressed in this basis. Often the hopping parameters, t_{ij}, are approximated as the same as those for the Kohn-Sham non-interacting Hamiltonian [216, 159]. The interaction parameters V_{ijkl} has a frequency dependence originating from the ω appearing in the expression for the polarization.

Interaction between the d states is already accounted for in the non-interacting Kohn-Sham Hamiltonian. Interactions between all electrons in the system is part of the external potential in the Kohn-Sham auxiliary system, which is solved self-consistently to determine the Kohn-Sham orbitals and eigenvalues. A **double-counting correction** is normally subtracted to remove these approximate interactions within the d states already present in the DFT results. Most of the applications of cRPA to DMFT in the literature have approximated this term [217, 218, 189]. More recently, Haule presented an approach to removing the double-counting bias for a given DFT functional [203].

Approximations. The errors of the RPA in §2.3.1 also apply here for cRPA. Additionally, the parameters from the method will depend on the definition of the orbitals that are integrated out. The Wannier basis is guaranteed to be a complete basis for the Kohn-Sham orbitals, but may not be a good basis for

the real system. Exactly what precise definition of a d orbital is the best description for the system is not addressable with this approach.

Examples of applications. All of the examples listed in §2.3.2 apply this technique to estimate the parameters for the model to solve using DMFT. To make the interactions local, usually only one-site terms in U are kept.

Current challenges. The results of DFT+DMFT calculations can be sensitive to the double-counting correction used. For example, a study with $SrVO_3$, Sr_2RuO_4, MnO, CoO, and NiO found orbital occupations and spectra can shift depending on the treatment of double-counting [218]. Similar results were found in NiO [217] and rare-earth nickelate perovskites [189].

Recently, higher-level calculations discovered certain classes of problems where cRPA breaks down [219]. As an example, when downfolding two-dimensional two and three-band Hubbard models to one band, they found that with equal hopping in both directions and $U = 4$, there were significant errors in the cRPA-downfolded Hamiltonian. A similar effect was seen in downfolding multiband Hubbard models in two dimensions [220]. Both studies attribute the error to the RPA approximation.

Critically, this formalism does not provide any means for evaluating the accuracy of approximate Hamiltonians independently of experiment. For example, it is an open question if Hubbard-like models are a good model for superconductivity in the cuprates, and even if they are, how many bands are required [38]. Additionally, there is no means of discovering the minimal set of parameters required to describe the system to some degree of accuracy. For example, the Hund's coupling term represents a complicated combination of a spin-resolved V_{ijkl} within the d space. There is no formalism for discovering that only this parameter is required without appealing to experiment.

3.2 Density matrix downfolding.

Density matrix downfolding [42, 210] is a method of determining the parameters and accuracy of a wide class of lattice models. The class of lattice models it determines are of the form:

$$\hat{H}_{\text{eff}} = \sum_l \beta_l \hat{d}_l, \tag{3.3}$$

where β_l are parameters and $\hat{d}_l$ are elements of the one- or two-body reduced density matrix (1-RDM/2-RDM). This definition includes band structure models ($\hat{d}_l$ are elements of the 1-RDM in a molecular orbital basis), tight-binding models ($\hat{d}_l$ are elements of the 1-RDM in a localized basis), Heisenberg models ($\hat{d}_l$ are of the form $S_i \cdot S_j$), Hubbard models ($\hat{d}_l$ are elements of the two-body density matrix), and combinations of

them. For instance, the one-band Hubbard model on square lattice is:

$$\hat{H}_{\text{eff}} = t\sum_{\langle ij\rangle}(c_i^\dagger c_j + \text{h.c.}) + U\sum_i n_{i,\uparrow}n_{i,\downarrow} \tag{3.4}$$

In this case, $\hat{d}_1 = \sum_{\langle ij\rangle}\hat{c}_i^\dagger\hat{c}_j$ and $\hat{d}_2 = \sum_i \hat{n}_{i,\uparrow}\hat{n}_{i,\downarrow}$.

3.2.1 Proof of principles

The goal of this process will be to efficiently describe a low-energy subspace of the full Hilbert space, called $\mathcal{LE}$. Let $|\Psi_i\rangle$ be the eigenstates of $\hat{H}$ with eigenvalue E_i, and let $E_0 \leq E_1 \leq ...$, i.e. the indices are sorted by energy. The **low-energy subspace**, $\mathcal{LE}$, is defined as the lowest n eigenstates for some integer, n: $\mathcal{LE} = \text{Span}(\{|\Psi_i\rangle_{i=1}^n\})$. Density matrix downfolding focuses on matching an effective energy functional, $E_{\text{eff}}[\Psi] = \langle\Psi|\hat{H}_{\text{eff}}|\Psi\rangle/\langle\Psi|\Psi\rangle$ to the first-principles energy functional, $E[\Psi] = \langle\Psi|\hat{H}|\Psi\rangle/\langle\Psi|\Psi\rangle$ for all $|\Psi\rangle \in \mathcal{LE}$. This section will prove that once this is done, the eigenstates and eigenvalues of $\hat{H}$ can be mapped to eigenstates and eigenvalues of $\hat{H}_{\text{eff}}$ in a straightforward manner. These proofs first appeared in Ref. [210].

Theorem 1. $|\Psi\rangle$ is a critical point of $E[\Psi]$ if and only if $|\Psi\rangle$ is an eigenstate of $\hat{H}$.

Proof of theorem 1. A functional derivative of $E[\Psi]$ demonstrates this.

$$\frac{\delta}{\delta\Psi^*}E[\Psi] = \frac{\delta}{\delta\Psi^*}\frac{\langle\Psi|H|\Psi\rangle}{\langle\Psi|\Psi\rangle} = \frac{H|\Psi\rangle}{\langle\Psi|\Psi\rangle} - \langle\Psi|H|\Psi\rangle\frac{|\Psi\rangle}{|\langle\Psi|\Psi\rangle|^2} = \frac{(H - E[\Psi])|\Psi\rangle}{\langle\Psi|\Psi\rangle}\,. \tag{3.5}$$

Thus, $(\hat{H} - E[\Psi])|\Psi\rangle = 0$ if and only if $\delta E[\Psi]/\delta\Psi^* = 0$, i.e. $|\Psi\rangle$ is a critical point of $E[\Psi]$.

Let $\mathcal{H}$ be the Hilbert space of $\hat{H}$. $\hat{H}_{\text{eff}}$ will be an operator on $\mathcal{LE}$, a subspace of $\mathcal{H}$. If $|\Psi\rangle \in \mathcal{LE}$ and $|\Phi\rangle \in \mathcal{H} \setminus \mathcal{LE}$, then $|\Psi\rangle \oplus |\Phi\rangle \in \mathcal{H}$. In the following, we will use the direct sum operator $\oplus 0$ to translate between the larger $\mathcal{H}$ and the smaller $\mathcal{LE}$. The state $|\Psi\rangle \oplus 0$ represented in the basis of eigenstates of $\hat{H}$ will have zero components for all eigenstates outside of $\mathcal{LE}$.

Lemma 1. Suppose that $|\Psi\rangle \in \mathcal{LE}$ and $|\Phi\rangle \in \mathcal{H} \setminus \mathcal{LE}$. Then $\left.\frac{\delta E[\Psi\oplus\Phi]}{\delta\Phi}\right|_{\Phi=0} = 0$.

Proof. $\langle\Psi \oplus 0|\hat{H}|0 \oplus \Phi\rangle = 0$ because the two states have non-overlapping expansions in the eigenstates of $\hat{H}$. Using that fact, we can evaluate

$$\left.\frac{\delta E[\Psi \oplus \Phi]}{\delta\Phi}\right|_{\Phi=0} = \left.\frac{\left(\hat{H} - E[\Psi \oplus \Phi]\right)|\Phi\rangle}{\langle\Psi|\Psi\rangle + \langle\Phi|\Phi\rangle}\right|_{\Phi=0} = 0. \tag{3.6}$$

This is equivalent to noting that $\hat{H}$ is block diagonal in the partitioning of $\mathcal{H}$ into $\mathcal{LE}$ and $\mathcal{H} \setminus \mathcal{LE}$.

Importantly, if $|\Psi\rangle \in \mathcal{LE}$, then $\frac{\delta E[\Psi\oplus 0]}{\delta(\Psi\oplus 0)^*} = |\Psi'\rangle \oplus 0$, where $|\Psi'\rangle \in \mathcal{LE}$.

Theorem 2 Assume $E[\Psi \oplus 0] = E_{\text{eff}}[\Psi] + C$ for any $|\Psi\rangle \in \mathcal{LE}$, where C is a constant. Then $(\hat{H}_{\text{eff}} + C)|\Psi\rangle \oplus 0 = \hat{H}(|\Psi\rangle \oplus 0)$.

Proof. Note that

$$\frac{\delta E[\Psi \oplus 0]}{\delta(\Psi \oplus 0)^*} = \frac{(\hat{H} - E[\Psi \oplus 0])|\Psi \oplus 0\rangle}{\langle\Psi|\Psi\rangle} \tag{3.7}$$

and

$$\frac{\delta E_{\text{eff}}[\Psi]}{\delta \Psi^*} = \frac{(\hat{H}_{\text{eff}} - E_{\text{eff}}[\Psi])|\Psi\rangle}{\langle\Psi|\Psi\rangle}. \tag{3.8}$$

Since the derivatives are equal, setting Eq. (3.7) equal to Eq. (3.8),

$$\hat{H}|\Psi \oplus 0\rangle = (\hat{H}_{\text{eff}} + E[\Psi \oplus 0] - E_{\text{eff}}[\Psi])|\Psi\rangle \oplus 0 = (\hat{H}_{\text{eff}} + C)|\Psi\rangle \oplus 0. \tag{3.9}$$

Theorem 2 combined with Lemma 1 means that the eigenstates of $\hat{H}_{\text{eff}}$ are the same as the eigenstates of $\hat{H}$ if the derivatives of its energy functional match $\hat{H}$. Such a $\hat{H}_{\text{eff}}$ always exists. Let $\hat{H}_{\text{eff}} = \sum_{n=1}^{N} E_n|\Psi_n\rangle\langle\Psi_n|$ where $|\Psi_n\rangle$'s are eigenstates belong to $\mathcal{LE}$. This satisfies $E[\Psi] = E_{\text{eff}}[\Psi]$ and $\hat{H}_{\text{eff}}|\Psi\rangle = H|\Psi\rangle$ for any $|\Psi\rangle$ in $\mathcal{LE}$. We have thus reduced the problem of finding an effective Hamiltonian $\hat{H}_{\text{eff}}$ that reproduces the low-energy spectrum of $\hat{H}$ to matching the corresponding energy functionals $E[\Psi]$ and $E_{\text{eff}}[\Psi]$.

3.2.2 Fitting energy functions that are linear in density-matrix elements

Given $\{\Psi_\alpha\}_{\alpha=1}^{N_{\text{samp}}} \subset \mathcal{LE}$, the best parameters for a model, $\hat{H}_{\text{eff}}$, can be defined as minimizing the square deviation between $E[\Psi_\alpha]$ and $E_{\text{eff}}[\Psi_\alpha]$ for all α. By assuming the linear form for the parameters (3.3) and evaluating $E_{\text{eff}}[\Psi_\alpha]$ on each sample, the problem becomes a standard linear regression:

$$\min_{\{\beta_l\}} \left\{ \left(E[\Psi] - \sum_l \beta_l \langle\Psi_\alpha|\hat{d}_l|\Psi_\alpha\rangle \right)^2 \right\} = \min_{\{\beta_l\}} \left\{ (\mathbf{y} - A\beta)^2 \right\}, \tag{3.10}$$

where $y_\alpha = E[\Psi_\alpha]$ is a component of the target vector, $A_{\alpha,l} = \langle\Psi_\alpha|\hat{d}_l|\Psi_\alpha\rangle$ is a matrix element of the linear predictor function, and $\beta = (\beta_1, ..., \beta_{N_{\text{parameters}}})$ is the parameter vector. The expectation values of the $\hat{d}_l$ operators are called **descriptors**, and are generally defined as observables meant to describe elements of the Hilbert space in a coarse-grained way. In the case of the one-band Hubbard model (3.4), $A_{\alpha,1} = \sum_{\langle ij\rangle}\langle\Psi_\alpha|\hat{c}_i^\dagger\hat{c}_j|\Psi_\alpha\rangle$ and $A_{\alpha,2} = \sum_i \langle\Psi_\alpha|\hat{n}_{i,\uparrow}\hat{n}_{i,\downarrow}|\Psi_\alpha\rangle$. If there are N_{samp} samples, then A is of size

$N_{\text{samp}} \times 2$, because there are two parameters, $\beta = (t, U)$. The samples need not be approximate eigenstates, but they should lie within $\mathcal{LE}$.

The data set can both determine the parameters and measure the degree to which E_{eff} correctly describes the set. The coefficient of determination, R^2, is the ratio of the variance explained by the model relative to the total variance of the data set [221]. The singular values of a principal component analysis measures the number of parameters required to describe the sample set [222]. Using LASSO, ridge regression, or orthogonal matching pursuit, techniques for regularization are available which find models with minimal number of parameters [223, 224, 225]. Uncertainty in the parameters can be measured using bootstrapping [226] or cross-validation [227]. A sense of the relative importance of parameters is available by evaluating the correlation between the descriptors and the energy of the samples. Similarly, a strong correlation within the sample set between residuals of a model and a descriptor outside the model suggests that the outside descriptor can be included to reduce errors.

To summarize, the density matrix downfolding process is:

(a) Generate samples in $\mathcal{LE}$, not necessarily eigenstates.

(b) Choose a set of descriptors to consider, $\hat{d}_l$.

(c) Form a vector of the energies, $\mathbf{y}$, and a matrix of the descriptors for each sample, A, both evaluated with first-principles methods.

(d) Perform linear regression: $\min_\beta (y - A\beta)^2$.

(e) Evaluate the sample and descriptor set.

The last step is to emphasize that review of the sample set or the descriptors is often needed. If there are insufficient descriptors, the method will find poor goodness-of-fit, for instance, low R^2. If there are insufficient samples to fit all the descriptors, the method will find large errors on the parameters. In this way, the method has an internal way of determining if the samples and the descriptors are a good match. Consequently, if the user is confident in either the samples or the descriptors, the method has an internal way of determining if the downfolding was successful and suggesting improvements. If neither the samples nor the descriptors are certain, the process requires more exploration and careful consideration. I present a new strategy for handling this situation in Chapter 9, which automatically finds low-energy samples for the model fit.

3.2.3 Examples of applications and current challenges

Examples of applications. Density matrix downfolding has been applied to several systems, successfully predicting excitation spectra. For example, the spectrum of benzene and graphene [42]. It has also been applied to study spin Hamiltonians, computing the singlet-triplet gap successfully in VO_2, and computing the correct effective exchange coupling in the parent compound of a cuprate superconductor [107, 123]

Current challenges. In most of the applications so far, the subspace of interest has been clear *a priori*. In many cases where the correct form for a model Hamiltonian is unclear, it is also unclear what low-energy states of the systems are like. For example, the proper effective model for the ground state magnetic properties of the iron-based superconductor, FeSe, is unclear. Sometimes the process will require low-energy states with a given orbital occupation or other property. It is sometimes difficult to guess low-energy wave functions with a given orbital occupation (for example). This is especially difficult if the state of interest shares its symmetries with another state in the sample set. I present a new method of addressing this challenge in Chapter 9.

Additionally, a many-body calculation is required for each sample, which makes this significantly more computationally expensive than cRPA downfolding. Generalizations to fitting parameter derivatives of the model can alleviate this, but nonetheless require calculations of large numbers of many-body properties. Because of this, for large systems, it is important to choose samples carefully to minimize the number of necessary samples.

Chapter 4

Connecting methods into a calculation workflow

An accurate DMC calculation requires input from several of these methods together. The basic workflow for a DMC calculation is outlined here.

(a) Perform a self-consistent calculation such as Hartree-Fock (§2.1.1) or DFT (2.2) to provide orbitals $\{\phi_i(r_j)\}$ for a Slater determinant or multi-Slater wave function (§2.1.4). DFT provides orbitals through the Kohn-Sham *ansatz* (§2.2.2).

(b) Form a state of the form $\Psi_{\mathrm{T}}(\mathbf{R}) = \Phi_{\uparrow}(R_{\uparrow})\Phi_{\downarrow}(R_{\downarrow})e^{U(\mathbf{R})}$, where $\Phi_{\uparrow}(R_{\uparrow})$ and $\Phi_{\downarrow}(R_{\downarrow})$ are Slater determinant wave functions from (a) containing the up and down electron coordinates, respectively, and $e^{U(\mathbf{R})}$ is a Jastrow factor (§2.1.4). Optimize the Jastrow parameters with VMC (§2.1.4). For small systems, the multi-Slater coefficients or orbitals can also be optimized at this step.

(c) With the VMC-optimized $\Psi_{\mathrm{T}}(\mathbf{R})$, use this as the trial function for a fixed-node DMC calculation (§2.1.5): $\Psi_{\mathrm{FN}}(\mathbf{R}) = \lim_{\tau\to\infty} e^{-\tau\hat{H}}\Psi_{\mathrm{T}}(\mathbf{R})$.

Properties from the VMC step are also used for reducing the mixed-estimator error when quantitative accuracy is important.

These methods are also used in various ways to generate the samples, $|\Psi_\alpha\rangle$, for density matrix downfolding (chapter 3). For example, one can start with either Hartree-Fock or a DFT functional to generate a Slater determinant of Hartree-Fock orbitals or Kohn-Sham orbitals. Different samples will use the ground state determinant, singles excitations, doubles excitations and so on. For each determinant, VMC is used to optimize a Jastrow factor. Finally each of these states is used as a trial function for fixed-node diffusion Monte Carlo. The fixed-node constraint keeps these states from all converging to the same state, but the projection dramatically lowers their energy, making them reasonable approximations to a sampling of $\mathcal{LE}$. The other method is described in more detail in §9, and utilizes a modification of the objective function in VMC to explore $\mathcal{LE}$ systematically.

Chapter 5

Reaction barriers for non-hydrogen transfer reactions

The work in this chapter was reported in K. Krongchon, B. Busemeyer, and L. K. Wagner, "Accurate barrier heights using diffusion Monte Carlo," *The Journal of Chemical Physics*, **146**, 12, 124129, (2017). The results help to demonstrate the accuracy of FN-DMC for realistic calculations which are directly comparable to experiment. Fixed node diffusion Monte Carlo was performed on a test set of forward and reverse barrier heights for 19 non-hydrogen-transfer reactions, and the nodal error was assessed. The DMC results are robust to changes in the nodal surface, as assessed by using different mean-field techniques to generate single determinant wave functions. Using these single determinant nodal surfaces, DMC results in errors of 1.5(1) kcal/mol on barrier heights (meaning 1.5 kcal/mol with 0.1 kcal/mol standard error). Using the large data set of DMC energies, we attempted to find good descriptors of the fixed node error. It does not correlate with a number of descriptors including change in density, but does show some correlation with the gap between the highest occupied and lowest unoccupied orbital energies in the mean-field calculation.

5.1 Reaction barriers from first-principles

DMC has been applied to both periodic and open boundary Hamiltonians and can obtain accurate results currently up to around 1000 electrons [89]. These aspects make DMC an interesting possibility for studying large reactions such as those on surfaces. In order to properly evaluate the performance of DMC on chemical systems, extensive benchmarking is necessary. There have been only a few tests of the performance of QMC methods for reaction barriers. DMC studies of reaction barriers have been calculated for $H + H_2$ [228, 229, 230], several organic molecules [231, 232, 233, 234, 235], surface reactions [236, 237, 72], and others [238, 239]. These have generally found that DMC can get close to or within chemical accuracy for reaction barriers, often improving on results of density functional theory (DFT). Recently, a large test set of DMC calculations on hydrogen-transfer reactions found mean unsigned errors of 1.0 kcal/mol for barrier heights and between 0.5 and 0.8 for bond dissociation energies, depending on the approximations used [240]. However, no large test sets of reaction barriers of non-hydrogen transfer reactions computed at the same

level of accuracy using DMC have been conducted prior to this work.

We use a high-throughput implementation of DMC to study a database from Peverati and Truhlar [2]. The database consists of non-hydrogen-transfer reactions that involves relatively small molecules, and was chosen to complement the existing results from other methods on this particular set of reactions available in the literature [1, 241, 242]. We evaluate several simple strategies for constructing trial wave functions and assess their performance. We also present a recipe for QMC calculations of reaction barriers that obtains mean absolute errors of reaction barriers of approximately 1.5(1) kcal/mol, close to so-called chemical accuracy.

5.2 Details of the calculations

We consider the 19 reactions enumerated in Table 5.1. The barrier heights are calculated by subtracting the DMC total energies of the products and reactants to the transition states. We employ the clamped ion approximation to the Hamiltonian of the ions, which neglects the kinetic energy of the ions.

The Hartree–Fock (HF) and DFT calculations were performed using the CRYSTAL code [243]. The core electrons were removed using pseudopotentials published by Burkatzki, Filippi, and Dolg [204, 205]. The use of these pseudopotentials has been justified by Nazarov *et al.* [244]. We used a Gaussian triple-ζ basis set with polarization functions.

The set of orbitals produced by each of these methods was used as the foundation for a Slater–Jastrow-type trial wave function for DMC calculations. The Jastrow factor was optimized by minimizing the variance of the local energy. DMC was then performed on the Slater–Jastrow wave function to find the best estimate of the ground state energy for each system. Both the variational and the diffusion Monte Carlo calculations are done within the open source code QWalk [90]. Thus, four DMC methods: DMC(PBE), DMC(HF), DMC(PBE0), and DMC(Min) are considered. The first three represent DMC calculations whose Slater determinant is generated by the method in parentheses. The DMC(Min) method is formed by taking the minimum DMC energy among the other three. Due to the variational principle, DMC(Min) should give the closest upper bound to the ground state energy and would be the canonical DMC result for predictions.

5.3 Results

The trial wave function performances from each of the nodal surfaces are compared in Fig. 5.1. For each system, we show the total DMC energy relative to the lowest energy of the three methods. The transition states labeled as TS01 to TS19 are defined in Table 5.1. The Ne and Ar atoms have also been checked and

Table 5.1: The non-hydrogen-transfer reactions [1] and their corresponding IDs. The transition states are labeled as TS01 to TS19, following Ref [2]. When + separates the reactants or products, the energies of each atom or molecule are calculated in separate DFT, HF, or DMC calculations, whereas when ... separates the reactants or products, all the reactants or all the products are simulated in the same calculation together although they are actually seperated in physical space.

ID	Reaction
1	$H + N_2O \xrightarrow{TS01} OH + N_2$
2	$H + FH \xrightarrow{TS02} HF + H$
3	$H + ClH \xrightarrow{TS03} HCl + H$
4	$H + FCH_3 \xrightarrow{TS04} HF + CH_3$
5	$H + F_2 \xrightarrow{TS05} HF + F$
6	$CH_3 + FCl \xrightarrow{TS06} CH_3F + Cl$
7	$F^- + CH_3F \xrightarrow{TS07} FCH_3 + F^-$
8	$F^- \ldots CH_3F \xrightarrow{TS07} FCH_3 \ldots F^-$
9	$Cl^- + CH_3Cl \xrightarrow{TS09} ClCH_3 + Cl^-$
10	$Cl^- \ldots CH_3Cl \xrightarrow{TS09} ClCH_3 \ldots Cl^-$
11	$F^- + CH_3Cl \xrightarrow{TS11} FCH_3 + Cl^-$
12	$F^- \ldots CH_3Cl \xrightarrow{TS11} FCH_3 \ldots Cl^-$
13	$OH^- + CH_3F \xrightarrow{TS13} HOCH_3 + F^-$
14	$OH^- \ldots CH_3F \xrightarrow{TS13} HOCH_3 \ldots F^-$
15	$H + N_2 \xrightarrow{TS15} HN_2$
16	$H + CO \xrightarrow{TS16} HCO$
17	$H + C_2H_4 \xrightarrow{TS17} CH_3CH_2$
18	$CH_3 + C_2H_4 \xrightarrow{TS18} CH_3CH_2CH_2$
19	$HCN \xrightarrow{TS19} HNC$

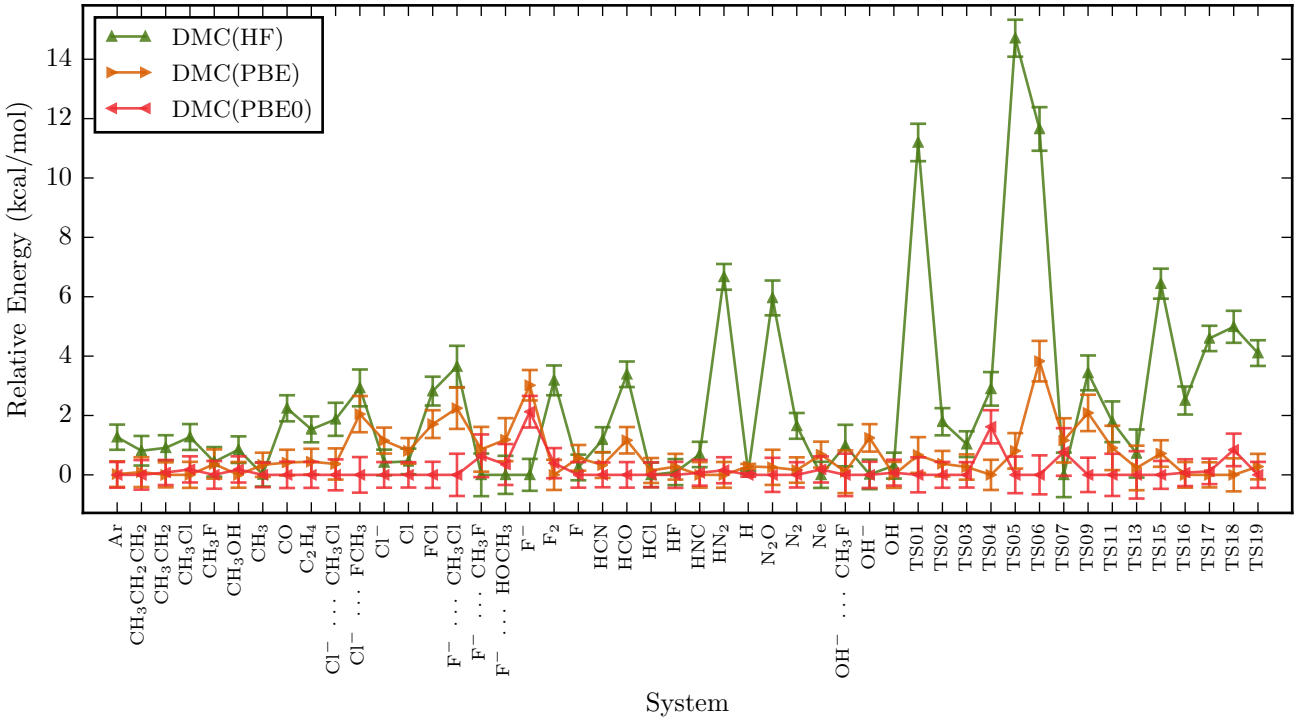

Figure 5.1: The DMC total energy relative to the lowest energy among the three functionals. The error bars are statistical errors from DMC.

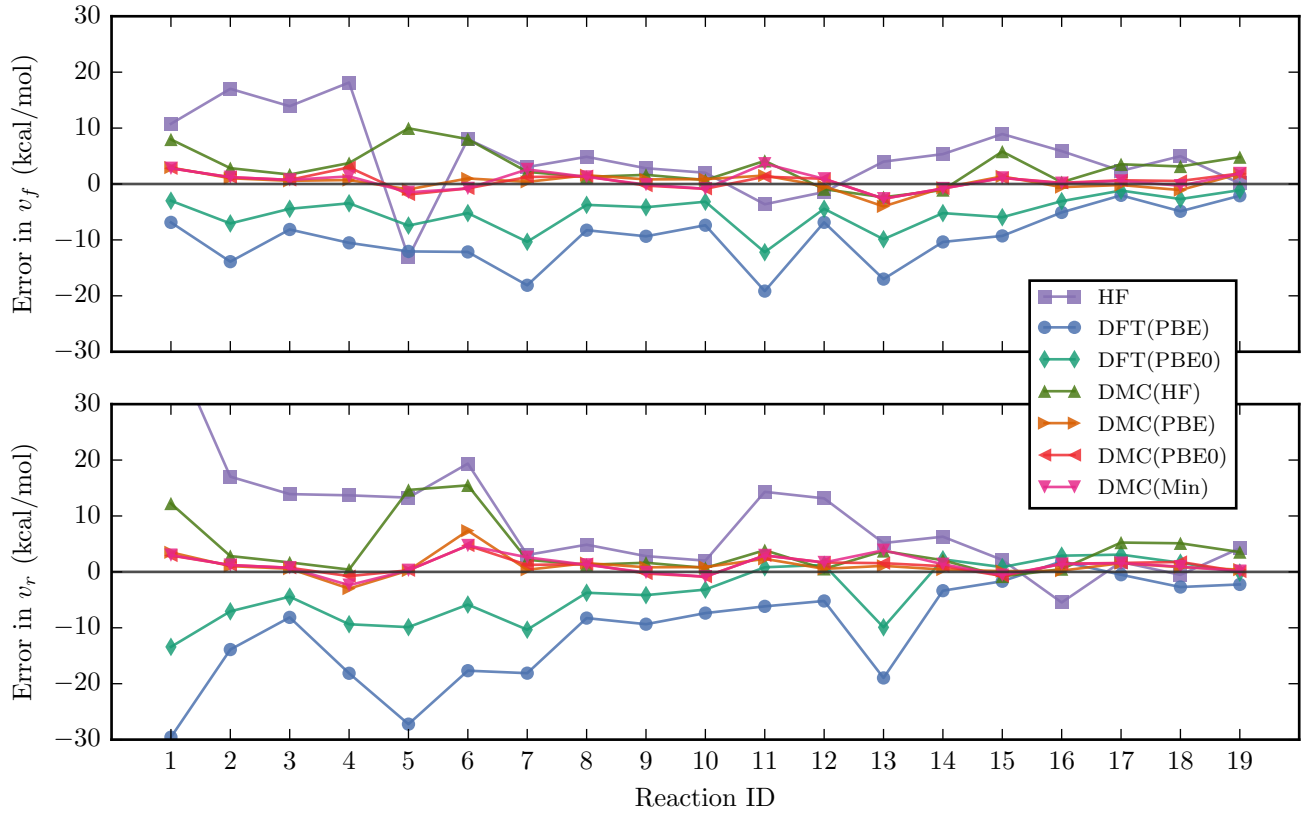

Figure 5.2: The error of forward and reverse reaction barrier heights, denoted by v_f and v_r, versus reaction ID as defined in Table 5.1. The error bars are insignificant and therefore neglected. The value of the missing point, v_r of HF for Reaction 1, is 41.14 kcal/mol.

included in the plot as a comparison to other closed shell systems. From the plot, the Kohn–Sham orbitals calculated from the PBE0 functional yield the lowest DMC energies for almost all systems studied, except for F^- and Ne, which are closed shell second period atoms, where DMC(HF) outperforms DMC(PBE0). The fact that HF tends to do better for closed shell second period atoms agrees with the general trend that has been observed, for example, in C_2 and Si_2 [85, 245].

After obtaining the energy for each system, we calculate the forward and reverse barrier heights, denoted by v_f and v_r, of the reactions in Table 5.1. The error between the calculated barrier heights and the experimental results [1, 2] are presented in Fig. 5.2. For reference, we also present the results of the DFT and HF calculations. However, note that our DFT results are using HF pseudopotentials, so they will differ slightly from results including all electrons or using DFT- and DFT-functional-specific pseudopotentials. The dependence of the DMC results on the nodal surface is on the order of a few kcal/mol for these systems.

Consistent with a previous study [1], HF tends to overestimate the barrier height, and the trend continues

to hold for DMC(HF). The notable exception is Reaction 5, which is far too low in HF, while it is unusually too high in DMC(HF). This discrepancy can be understood by the fact that HF seems to overestimate the energy of F_2 as can be seen from Fig. 5.1, while the fixed-node error of TS05 is particularly large. This illustrates the general feature that the fixed-node errors tend not to correlate with the quality of the method generating the trial wave function, which is examined in the Discussion.

To summarize the results, the errors in v_f and v_r are combined into a single data set and presented as a box-and-whisker plot [246] as shown in Fig. 5.3 (Top). The plot shows that DFT(PBE) tends to underestimate the barrier height, while HF does the opposite, as has been found before [1, 247]. On going to the DMC results, the spread in the barrier-height errors decreases dramatically, while the median is much closer to zero. While DMC(PBE) method yields the median closest to zero, 5 out of the 19 results were outliers, suggesting this trial wave function is less reliable.

Finally, the mean absolute error (MAE) for each method has been calculated and reported in a bar chart (Fig. 5.3) (Bottom). As discussed previously, the reactions being tested do not exhibit any significant difference between DMC(PBE0) and DMC(Min) because DMC(PBE0) tends to provide the lowest total energies. Neglecting DMC(Min), the most accurate methods as shown are DMC(PBE) and DMC(PBE0) followed in order by DMC(HF), DFT(PBE0), HF, and DFT(PBE). The differences in the overall accuracy for DMC(Min), DMC(PBE), and DMC(PBE0) are statistically indistinguishable by our calculations. However, these three methods clearly perform better than DMC(HF). The MAEs in DMC(Min) and DMC(PBE0) are 1.5(1) kcal/mol and 1.4(1) kcal/mol—close to the 1 kcal/mol accuracy necessary to predict chemical reaction rates.

For comparison, Zheng *et al.* [241] found the best N^4 scaling methods to have MAE around 1 kcal/mol, and the best N^3 scaling methods to have error around 3 kcal/mol. The best accuracy methods in this category of their database are semi-empirical density functionals, whereas our DMC methods require no experimental input. From this database, other wave-function-based methods such as variants of the CCSD(T) method attain a MAE of around 0.5 to around 1 kcal/mol accuracy, but scale much less favorably with system size.

5.4 When are fixed-node errors large?

Analyzing trends in the fixed node error of the test set demonstrates the principle that the quality of the functional may have little to do with the quality of the DMC calculation utilizing the trial wave function it generates. The error in the barrier heights themselves did not correlate reliably between the method producing the trial function and the final DMC result. For instance, the HF error of v_f in Reaction 5 is

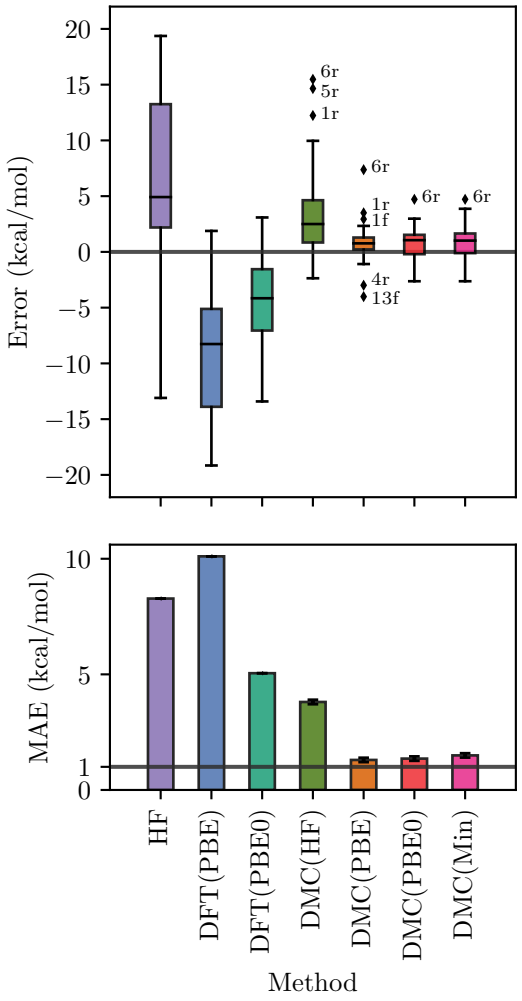

Figure 5.3: (Top) The box-and-whisker plot of the barrier-height errors for each method. Each box ends at first (Q_1) and third (Q_3) quantiles. The horizontal line in each box represents the median. The whiskers extend to the farthest points within 1.5 times the difference between Q_1 and Q_3. Every point outside of this range is represented by a diamond and labeled by an ID number as defined in Table 5.1 followed by a character, r or f, which represents a forward or reverse reaction. (Bottom) The bar chart of the mean absolute error for each method. The DMC error bars denote statistical errors.

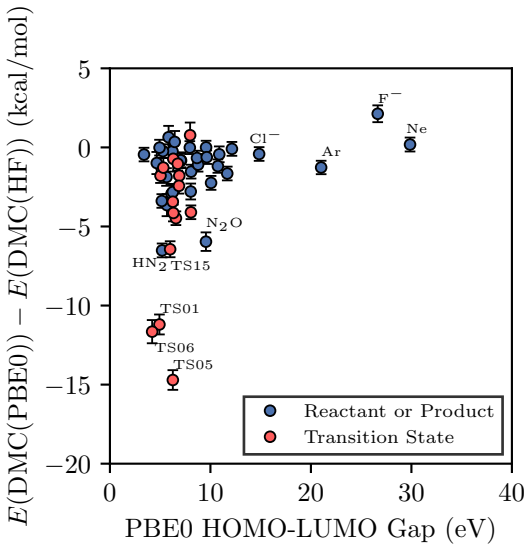

Figure 5.4: Approximate nodal error, measured by the energy difference between DMC(PBE0) and DMC(HF) plotted against the HOMO-LUMO gap, computed by PBE0.

more negative, while DMC(HF) error is more positive compared to the average error.

We attempted to find some correlation with quantities computable in DFT and HF which may indicate the fixed node error may be large. We computed several physical quantities within PBE0 and HF and checked to see if the differences between these results correlated with the nodal error, measured by the difference in energy between DMC(PBE0) and DMC(HF). We found that the difference in energies computed by the PBE0 and HF did not correlate with the fixed-node error. Also, the square difference in the electron densities between PBE0 and HF, $\int d^3r\ (\rho_{\mathrm{PBE0}}(\mathbf{r}) - \rho_{\mathrm{HF}}(\mathbf{r}))^2$ did not correlate with the fixed-node error. The total change in atomic charges, measured by $\left(\sum_I (c_{I,\mathrm{PBE0}} - c_{I,\mathrm{HF}})^2\right)^{1/2}$ where $c_{I,\mathrm{PBE0}}$ is the number of electrons on ion I as measured by PBE0, for example, also did not correlate with the fixed-node error. Additionally, the difference in the barrier heights between DMC(PBE0) and DMC(HF) did not correlate with the difference in barrier heights between PBE0 and HF.

We did find some correlation between the gap in energy between the highest-occupied and lowest-unoccupied-molecular-orbital (the HOMO-LUMO gap) and the fixed-node error. Fig. 5.4 plots out the HOMO-LUMO gap computed by PBE0 compared to the energy difference between DMC(PBE0) and DMC(HF). This plot illustrates how the worst fixed-node errors tend to occur in transition states, and these transition states tend to have lower energy gaps. This is consistent with previous work on reaction barriers [239], which found that transition states tend to have multiconfigurational character, due to the stretching of bonds which often occurs in transition states.

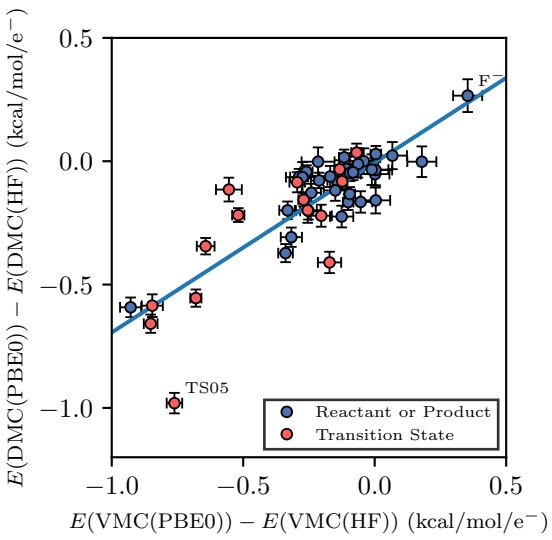

Figure 5.5: Approximate nodal error, measured by the energy difference between DMC(PBE0) and DMC(HF) plotted against the energy difference between VMC(PBE0) and VMC(HF).

We also attempted to correlate the fixed node error with VMC results. For variance optimized wave functions, the noise inherent in the variance optimization was a limiting factor in making the comparison. While this noise does not affect the DMC results, it is larger than any correlation between the optimized variance and the DMC energy. Instead, we reoptimized the wave functions using the linear method [85], minimizing the energy directly, as shown in Fig. 5.5. There is a high correlation (0.7) between the VMC energies and the DMC energies. We found that to obtain this correlation, the total energy needed to be optimized to high accuracy. In some cases, this could be more computationally demanding than the DMC calculation.

5.5 Conclusions from barrier height study

We have found that fixed node diffusion Monte Carlo (DMC) with a single Slater determinant can obtain near-chemical accuracy for a benchmark set of 19 chemical reactions. Using this set, we performed statistical analysis to investigate trends in the nodal error. Of the functionals we surveyed, PBE0 provides the lowest energy nodal surfaces for almost all molecules. The size of the nodal errors in DMC are uncorrelated with the error of the DFT functional used to produce the trial wave function but do tend to be larger for transition states with small HOMO-LUMO gaps. However, the HOMO-LUMO gap does not appear to completely determine the nodal error. Since the version of the algorithm we used scales very well with system size, $\mathcal{O}(N_e^{3-4})$, it is applicable even to larger systems, and since it does not use fitted parameters, one may expect

it to have similar accuracy on other systems. It thus appears that DMC could be a viable route to performing high accuracy calculations on barrier heights for many chemical systems.

Chapter 6

Accurate FN-DMC calculations of FeSe

The work in this chapter was reported in B. Busemeyer, M. Dagrada, S. Sorella, M. Casula, and L. K. Wagner, "Competing collinear magnetic structures in superconducting FeSe by first-principles quantum Monte Carlo calculations," *Phys. Rev. B*, **94**, 3,035108, (2016). The results labeled "VMC(opt)" and "DMC(opt)" and the PBE calculations were performed by M. Dagrada, S. Sorella, and M. Casula. All other calculations were performed by me. These results demonstrate that FN-DMC can provide both accurate results and insight into microscopic mechanisms for unusual properties in materials that are difficult to analyze with other theoretical approaches.

Resolving the interplay between magnetic interactions and structural properties in strongly correlated materials through a quantitatively accurate approach has been a major challenge in condensed matter physics. Here we apply highly accurate first principles quantum Monte Carlo (QMC) techniques to obtain structural and magnetic properties of the iron selenide (FeSe) superconductor under pressure. Where comparable, the computed properties are very close to the experimental values. Of potential ordered magnetic configurations, collinear spin configurations are the most energetically favorable over the explored pressure range. They become nearly degenerate in energy with bicollinear spin orderings at around 7 GPa, when the experimental critical temperature T_c is the highest. On the other hand, ferromagnetic, checkerboard, and staggered dimer configurations become relatively higher in energy as the pressure increases. The behavior under pressure is explained by an analysis of the local charge compressibility and the orbital occupation as described by the QMC many-body wave function, which reveals how spin, charge and orbital degrees of freedom are strongly coupled in this compound. This remarkable pressure evolution suggests that stripe-like magnetic fluctuations may be responsible for the enhanced T_c in FeSe and that higher T_c is associated with nearness to a crossover between collinear and bicollinear ordering.

6.1 Introduction to FeSe

The quest for a microscopic theory of unconventional or high-temperature superconductivity is a major challenge in condensed matter physics. The discovery of iron-based superconductors in 2006 [14] was an important contribution to the field since it added a second class of high-temperature unconventional superconductors to the experimental roster, along with the cuprate superconductors. Despite their different electronic structure, their phase diagrams have striking similarities[248, 249], particularly the proximity of the superconducting phase with an antiferromagnetic state. This behavior, along with other considerations[250, 251, 252, 253, 254], makes it likely that spins and magnetism are important in determining the superconducting state.

FeSe is a particularly interesting example of the iron-based superconductors for several reasons. Its critical temperature is strongly dependent on pressure[255, 254, 5], reaching 37 K at 7 GPa. At ambient conditions, FeSe has a simple P4/nmm crystal structure with two inequivalent Fe and Se positions per unit cell, and it undergoes a distortion from tetragonal to orthorhombic symmetry by cooling it down below 91 K, while it becomes superconducting below 8 K at ambient pressure. An intriguing peculiarity of FeSe is that, at variance with most of the iron-based superconductors, it does not show any long-range magnetic order at ambient pressure[256]. Long-range magnetic order is realized under pressure [257]. Additionally, antiferromagnetic spin fluctuations have been revealed by neutron scattering experiments (see for example Ref. [258]) in the proximity of the superconducting phase. Their role in driving the nematic transition and their connection to superconductivity have been the subject of intense debate. All these aspects make it attractive for computational techniques to correlate microscopic electronic structure with the superconductivity and it is therefore one of the most studied iron-based superconductors. However, the precise calculation of the properties of this material remains challenging from first principles methods such as density functional theory (DFT) due to strong electron correlation.

For example, the PBE band structure is in poor agreement with experiments which report a considerably narrower bandwidth[259, 260]. Furthermore the FeSe lattice constants display an average error of ~ 0.1 Å independently from the exchange correlation functional employed (see for instance Ref [261] and Tab 6.1). Despite useful work using dynamical mean field theory[262, 263, 193, 264, 265, 266, 267, 268, 269, 270, 271, 272] and GW[194, 273, 274] methods, there is a need for high quality calculations that can better describe the electronic and crystal structure of these materials.

In this chapter, I describe the results of first principles quantum Monte Carlo simulations of the magnetic behavior of FeSe under pressure. We find that, compared to commonly used density functional theory calculations, the FN-DMC calculations obtain more accurate lattice constants, bulk moduli, and band dispersion.

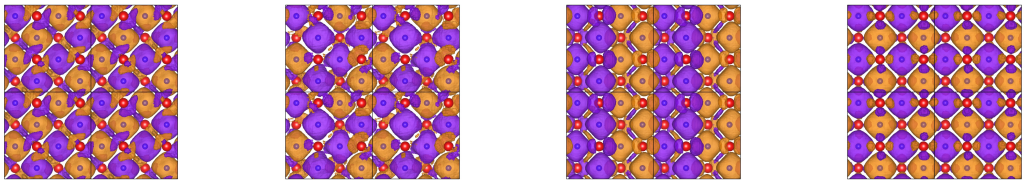

(a) (b) (c) (d)

Figure 6.1: Spin densities of magnetic orderings at ambient pressure, (a) collinear, (b) collinear, 1 flip, (c) bicollinear, and (d) checkerboard. Four unit cells of a single iron layer are shown, divided by black lines. "Collinear, 1 flip" refers to flipping the spin of one iron per unit cell in the collinear configuration. Since four unit cells are shown above, there are four "flipped" iron moments shown in this plot. The larger red Se atoms lie above and below the plane and show significantly smaller spin density. Irons are smaller and blue, and lie within larger concentration of spin. The two colors of the isosurfaces denote density of up and down.

By increasing the pressure, the difference in energy of ordered magnetic states with stripe-like order goes to zero with pressure, while checkerboard-like magnetic states increase in energy. The convergence of the stripe-like magnetic states is correlated with the increase in T_c in this material under pressure, which offers a tantalizing connection to spin fluctuations as a potential origin. Such behavior may be a calculable design principle for new unconventional superconducting materials.

6.2 Details of the calculations

We perform FN-DMC calculations with a single Slater-Jastrow trial wave function *ansatz*, To test the sensitivity of the choice of orbitals used in the Slater determinant part, we use two approaches to determine the orbitals. The first optimizes a parameter in density functional theory used to generate the orbitals, and is the less computationally demanding of the two. The parameter to be optimized in the Slater determinant is the amount of exact exchange w, for which we find the optimal value near $w = 0.25$. This corresponds to the PBE0 functional, and this optimum is often the case for similar calculations on transition metal systems [275]. For consistency, we used $w = 0.25$ for all our calculations, and we denote this method by DMC(PBE0). The details of the optimization of functional and of the parameter, w, is reported in the appendix. The second QMC approach used in this work performs a complete variational optimization of the determinant orbitals within a relatively small basis set, and is more computationally demanding but in principle more accurate. These calculations are denoted throughout the paper with the label QMC(opt), where QMC will refer to VMC or DMC depending on the calculation. Further information on the orbital optimization procedure is provided in the Supplementary Material. In our tests for FeSe, while the DMC(opt) technique did obtain lower energies as expected, the energy differences were consistent between the two techniques, so most data is obtained from DMC(PBE0).

All DMC(PBE0) calculations were done within the open-source package QWalk [90], with orbitals generated by DFT calculations performed with the DFT code CRYSTAL [243]. For the DMC(opt) method, we used the package TurboRVB [276].

We use the BFD pseudopotential to approximate the core of the atoms [204, 205]. The energy difference between the collinear and checkerboard magnetic state is consistent between an all-electron and pseudopotential PBE0 calculation within 0.01 eV. The convergence of the most important parameters in both our QMC methods is shown in the "Convergence and validation" section of the appendix. For the FeSe crystal structure, the anion height above the iron planes is the only internal parameter of the compound in the tetragonal P4/nmm phase. This parameter represents a crucial ingredient to determine the magnetic behavior of FeSe, but its evaluation by first-principles methods is a challenging task, as detailed in the section titled "Crystal structure." The optimization of the Se height is carried out with two different procedures. For the DMC(PBE0) method, the relaxed value is obtained by fitting a total energy curve with a cubic function. In the VMC(opt), the optimized Se height value is obtained by a direct minimization of the ionic forces within the variational Monte Carlo framework [277]. By including the cell parameters in the minimization procedure, we are able to fully relax the crystal structure of FeSe at different magnetic orderings. We consider a minimization converged when both the forces and their error bars are lower than 10^{-3} Ha/a.u. per atom.

We found that effects due to the finite size of the simulation cell, or finite size errors (FSEs), constitute the major source of systematic error for both DMC(PBE0) and DMC(opt). We apply several techniques in order to reduce FSEs. All DMC(PBE0) calculations are twist averaged [278] over 8 twist conditions on the 8 f.u. FeSe supercell; DMC(opt) results are instead obtained with a larger 16 f.u. supercell averaging over periodic and antiperiodic boundary conditions; further corrections are then applied to cure one-body and two-body FSEs. In both cases, we managed to reduce the impact of FSEs below the desired accuracy on energy calculations. A detailed explanation of the procedures used to control FSEs is given in the appendix.

6.3 Results

6.3.1 Trial wave functions and ground state

For the Slater-Jastrow wave function there are many local minima both in preparing the Kohn-Sham orbitals using density functional theory and in optimizing the orbitals directly. These minima correspond to different magnetic orderings of the Fe spins. The most relevant ones are presented in Fig. 6.1. We also included a type of paramagnetic state in which the up and down spin orbitals are constrained to be equal, but we found

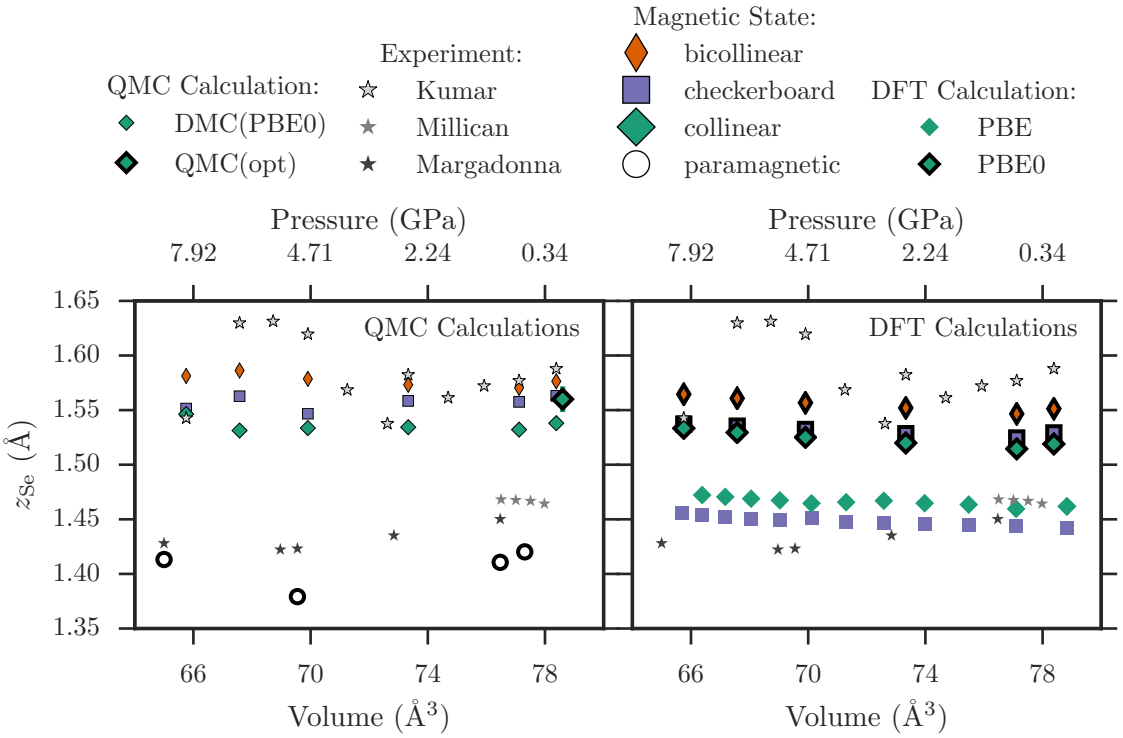

Figure 6.2: Selection of experimental measurements from Margadonna *et al.* [5], Kumar *et al.* [6], and Millican *et al.* [7] of the selenium height, z_{Se}, as a function of pressure, along with corresponding QMC (left) and DFT (right) predictions. QMC(opt) refers to calculations done with a fully optimized Slater determinant, which was VMC for the paramagnetic state (open circles), and DMC for the collinear state (green diamonds). The fully-optimized QMC calculation is done at Γ-point only, but at a 16-f.u. supercell. The DMC(PBE0) points are at 8 f.u., but are twist averaged over 8 twist values, therefore should have compareable finite-size errors. More discussion of this comparison is available in the appendix. Accordingly, the ambient pressure DMC(PBE0) calculation agrees nearly within error bars with the fully optimized DMC(opt) calculation.

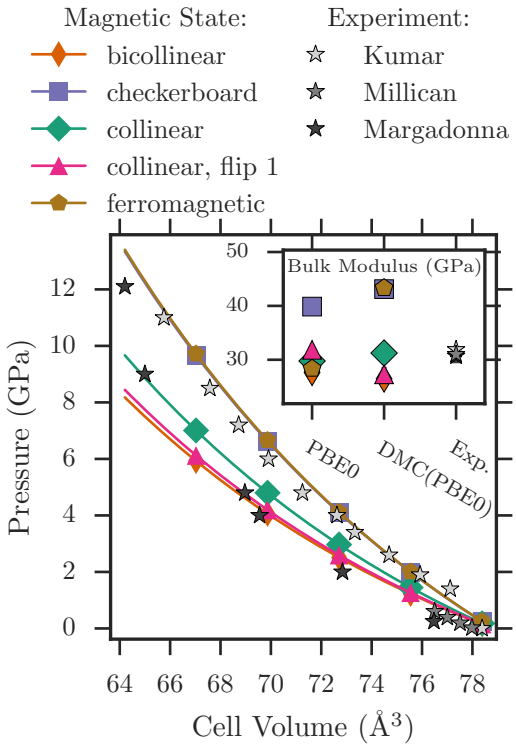

Figure 6.3: Pressure as a function of volume, computed through an equation-of-state fit to DMC(PBE0) data and from experiments by Margadonna *et al.* [5], Kumar *et al.* [6], and Millican *et al.* [7]. All points along the solid line come from the equation-of-state, and markers are added purely to distinguish the magnetic state. For the volumes considered here, regardless of spin ordering, $P(V)$ falls within the experimental spread. Inset displays corresponding bulk modulus in units of GPa for PBE0, DMC(PBE0), and the experiments considered. The bulk modulus is strongly coupled to the magnetic state, and for the collinear state, DMC(PBE0) demonstrates excellent agreement with all the experiments considered. Bulk moduli computed from PBE are between 7 and 9 GPa, and are much more insensitive to the magnetic ordering (see Supplemental Materials for tabulated values). Lattice constants used were those of Kumar[6].

that state to be more than 0.5 eV/Fe higher in energy than any magnetically ordered wavefunction. The ground state thus seems to require large local moments on the Fe atoms.

While it is known experimentally that FeSe does not have long-range ordering [256], the calculations here enforce periodic boundary conditions on a relatively small cell and thus cannot describe long-range fluctuations of the magnetic order that might be the cause of loss of long-range order. For the experimental crystal structure, the collinear magnetic ordering is the lowest in energy in our calculations and is observed to be the dominant short-range order experimentally [258]. The energetic cost of introducing a "defect" into the magnetic order is quite small; we will discuss that aspect later. Both the DMC(opt) and DMC(PBE0) approaches result in a rather large magnetic moment on the Fe atom. For the collinear magnetic ordering we obtain a value of $\sim 3.4\ \mu_B$ for DMC(PBE0), and a slightly lower $\sim 3.1\ \mu_B$ for the fully optimized calculations. In both cases the magnetic moment is close to the atomic limit.

Between the two DMC approaches, the energy difference between different magnetic orderings is in agreement within stochastic errors, so there is good reason to believe that the cheaper DMC(PBE0) technique is accurate. In comparison to PBE calculations, which are the most common in the literature, the relative energies according DMC are quite different, including the lowest energy magnetic phase, which is the "staggered dimer" configuration in DFT [279, 280, 281], but turns out to be the collinear configuration in DMC. It appears that hybrid DFT calculations in the PBE0 approximation obtain reasonably good magnetic energy differences in comparison to DMC; since this functional also produced the orbitals that gave the lowest FN-DMC energy, it may be capturing some of the correct physics for the magnetic properties of this material. However, the PBE0 functional predicts an insulating gap[8] for FeSe for all magnetic orderings, in contrast to DMC and experiment.

6.3.2 Crystal structure

Obtaining the correct crystal structure for FeSe is a major challenge, since the layers interact through non-bonded interactions. The c lattice parameter in particular is affected by Van der Waals interactions and electron correlation plays a key role in determining the in-plane physics. The behavior of FeSe's superconducting properties under pressure gives another clue on the importance of structural variations in its description. A first-principles prediction of the lattice parameters is thus an important test of the description of this physics. Since the DMC calculations are computationally costly, we limited our study to the tetragonal phase of FeSe. Because the low temperature orthorhombic distortion is small[5], one might expect that its effect on the overall electronic structure is also small. We leave such considerations to another paper.

The equilibrium lattice parameters of FeSe are presented in Table 6.1. As mentioned in the previous

Table 6.1: FeSe optimal structural parameters with different computational methods. DFT calculations have been performed with the software package QUANTUMESPRESSO [3] using a 10x10x10 k-points mesh, an energy cutoff of 75 Ry and norm conserving pseudopotentials for both Fe and Se. The variational Monte Carlo VMC(opt) results are obtained at Gamma point only with the 16 f.u. FeSe supercell containing 32 atoms.

SOURCE	MAGNETIC ORD.	a	c	$\overline{\text{FeFe}}$	z_{Se}
DFT-PBE	paramagnetic	3.6802	6.1663	2.6023	1.3862
DFT-PBE	collinear	3.8007	6.2363	2.6966	1.4568
VMC	paramagnetic	3.71(1)	5.49(1)	2.62(1)	1.437(5)
VMC	collinear	3.72(1)	5.68(1)	2.63(1)	1.56(1)
experimental [282] - T 7 K		3.7646(1)	5.47920(9)		1.4622
experimental [6] - T 8 K		3.7685(1)	5.5194(9)	2.6647(3)	1.5879
experimental [5] - T 300 K		3.7724(1)	5.5217(1)		1.4759

sections, these results are obtained with a direct optimization of FeSe cell parameters with the VMC(opt) method. The in-plane FeSe properties should be well captured by QMC since the a lattice parameter is in close agreement with experimental results (within $\sim 4\,\sigma$) independently of the chosen magnetic configuration. Both collinear and paramagnetic wavefunctions shows also a general improvement with respect to DFT concerning the c lattice parameter. This provides evidence of the accuracy in treating Van der Waals interactions with the QMC wavefunction, mainly achieved with the Jastrow factor[283, 284]. The evaluation of the inter-plane c distance might be affected by the dispersion along the z-axis, which we did not take into account in our supercell which always contains only one Fe plane. We check this dependency by performing a test structural relaxation on a FeSe supercell with 16 Fe atoms in two planes and 8 Fe atoms with only one plane considered in the supercell. We find that the difference between the c parameter obtained in the two configurations is negligible.

The final internal parameter z_{Se} represents the height of the selenium anion above the plane, and it has been experimentally demonstrated [285] to be of key importance in determining superconducting properties of iron-based superconductors in general. We collect all our calculations of z_{Se}, as well as some experimental results, in Fig. 6.2. We find that both the magnetic state and the accuracy of the calculation have an important effect on the prediction of this parameter. At approximately the same level of finite size error, our two DMC calculations agree very closely, determining that fixed node and basis set error is likely to be unimportant. However, we found that z_{Se} is surprisingly sensitive to finite size effects, both in the in-plane and out of plane directions. Given the supercells that we studied, we found a variation in z_{Se} of approximately 0.05 Å, depending on the twisted boundary conditions and supercell. With experimental lattice parameters, our best estimate for z_{Se} is thus 1.54(5)Å, which is quite close to the experimental range. As we shall see later, the properties of FeSe depend sensitively on z_{Se}, so to account for this uncertainty, we will consider properties as a function of selenium height as well as pressure.

By fitting an equation of state previously used by Anton *et al.* [286] to our DMC(PBE0) energies as a function of volume, we extract the bulk modulus and the pressure dependence on volume $P(V)$, shown in Fig 6.3. The collection of ambient-pressure bulk-moduli results is reported in the inset of Fig. 6.3, in units of GPa. For all these calculations, experimental lattice constants [6] have been used. $P(V)$ and the bulk modulus show a strong dependence on the magnetic order.

While $P(V)$ has scatter between experiments, they are more consistent in the bulk modulus, so we base our comparisons of the theoretical calculations on the latter quantity. The DMC(PBE0) calculation demonstrates excellent agreement with all three experiments if the collinear magnetic ordering is imposed, but it is less close to experiment for the other magnetic orderings. Our PBE0 calculations are also in somewhat good agreement with DMC(PBE0), except a notable disagreement for the ferromagnetic ordering. On the other hand, PBE bulk moduli are significantly lower than both experiment and the other calculations, generally predicting bulk moduli between 7 and 10 GPa, depending only slightly on the magnetic ordering. Since the collinear ordering is also the lowest energy for DMC(PBE0), for the remainder of this article, we use the collinear equation of state to estimate the pressures that correspond to the volumes used in the calculations.

6.3.3 Interaction of structure and magnetism

Fig 6.4 shows the interaction between pressure, magnetic ordering, and selenium height. As has been found before [287], the magnetic energies depend strongly on the selenium height, and this dependence changes with pressure. For a given pressure, there are two points on the selenium height curves that are of substantial interest. The first is the minimum energy (solid vertical line), which as can be seen in Fig 6.2, does not change very much with pressure(or volume) in our calculations. The second is the crossing point (dashed vertical line) between the collinear and bicollinear magnetic orderings, which are competing low-energy states. This crossing point depends on the pressure, and approaches the minimum energy point at higher pressures (lower volumes), as shown on the rightmost plot in the figure.

Another interesting feature visible in Fig 6.4 is that the checkerboard magnetic ordering intersects the bicollinear and collinear magnetic orders at zero pressure (78.4 Å^3) and large z_{Se}, but there is a shift of the checkerboard curve to higher energies once pressure is applied. The underlying physics of this effect will be discussed in the Section titled "Interaction of charge and orbitals with magnetism."

Fig 6.5 shows a cut through the data in Fig 6.4 along the minimum energy z_{Se} (subfigure a), and the experimentally determined z_{Se} (subfigure b). Along this cut we evaluated many magnetic orderings to establish a set of trends, and checked finite size errors by considering an 8 f.u. cell and 16 f.u. cell with

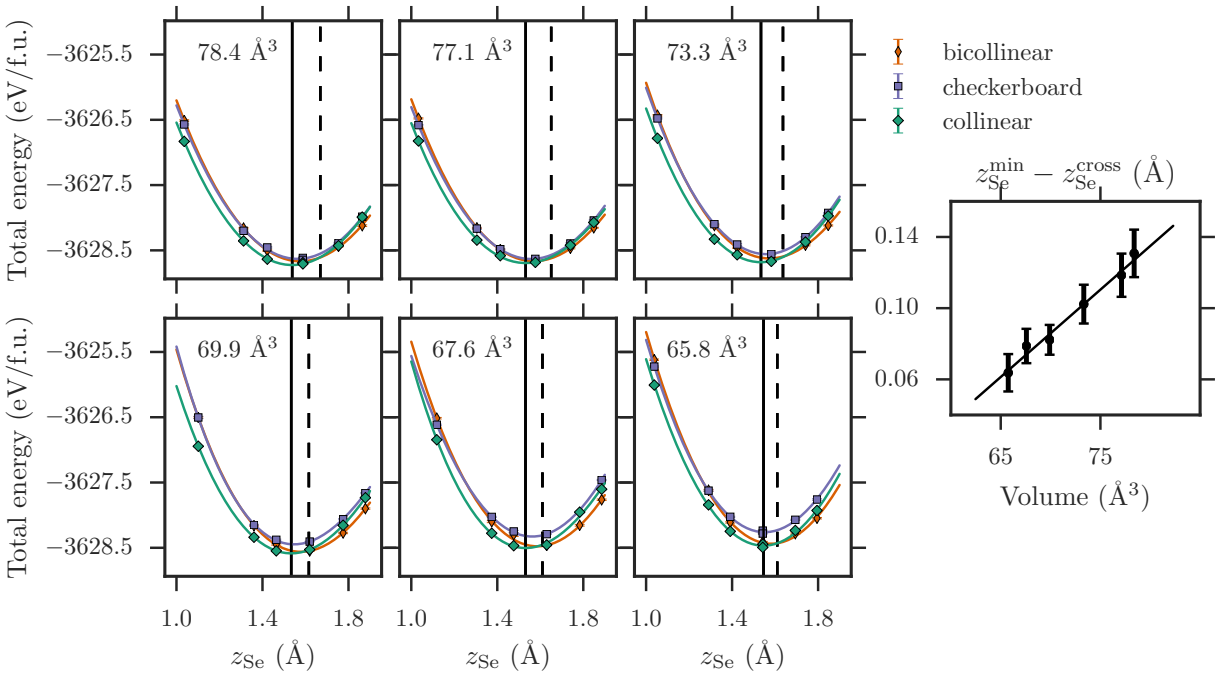

Figure 6.4: DMC(PBE0) energies as a function of volume and selenium height z_{Se} for three of the magnetic orderings. The solid vertical line represents the minimum of the collinear magnetic ordering, while the dashed vertical line represent the predicted crossing of the bicollinear and collinear energies. These two points converge as the pressure is increased, as shown on the far right.

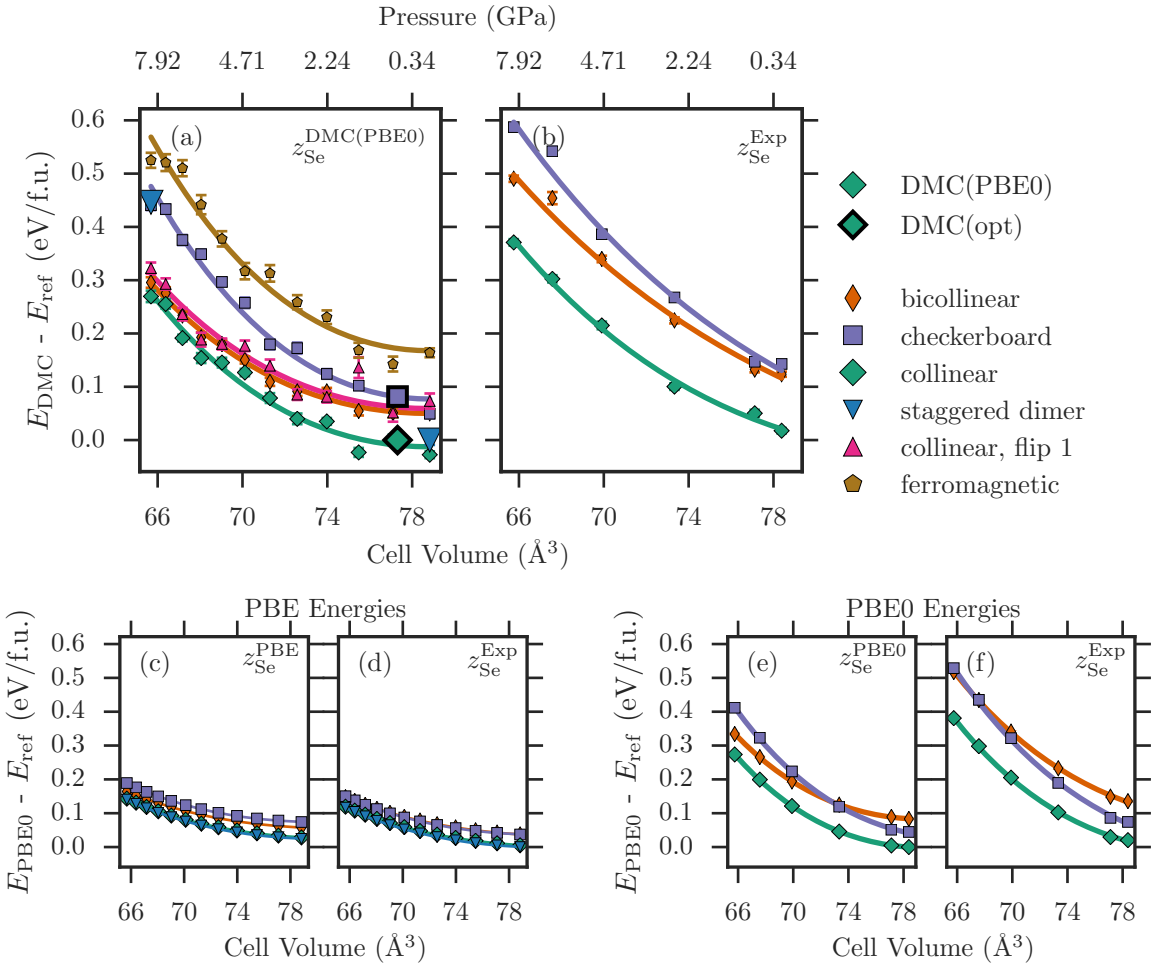

Figure 6.5: For each calculation (QMC, PBE, and PBE0): (Right) Total energies for 8 f.u. cell for various magnetic orderings, as a function of volume, choosing experimental [5] values of z_{Se}. (Left) Same as right, but choosing optimized values of z_{Se}. For the top QMC plots, energies are referenced to the collinear energy at around 77 Å^3. The DFT calculations are referenced to the z_{Se} minimum energy for that type of calculation. The DMC paramagnetic energies are $\sim$ 0.85 eV/f.u. higher than the reference collinear energy.

twist averaging. Further information on finite size corrections are available in the appendix. Under pressure, the checkerboard, ferromagnetic, and staggered dimer magnetic orderings rise in energy compared to the lowest energy collinear ordering. On the other hand, the stripe-like orderings, including the bicollinear and collinear orderings with defects converge with applied pressure.

From Fig 6.5 (bottom panels) the failure of PBE in capture this trend in FeSe energetics under pressure is apparent. Even with lattice constants fixed to experimental ones, the PBE energies of magnetically ordered states are quite different from the FN-DMC energies. In agreement with recent work, PBE does predict the staggered dimer as ground state. Despite the failure of PBE0 in describing the conducting behavior of FeSe, the magnetic energies are reasonably close to the DMC results.

Given the data available to us, we can determine some properties that are robust to the finite size errors and uncertainty in z_{Se} in our calculations. The first is that the relative energetics of magnetic orders changes strongly as a function z_{Se} and pressure. In FN-DMC and PBE0, which would *a priori* be expected to be more accurate, the collinear and bicollinear orders become closer in energy as with increasing pressure for reasonable values of z_{Se}. According to FN-DMC, this effect is robust against z_{Se} variations, depending mainly on the change in the relative magnetic energies as a function of pressure.

The energetic cost of reversing a single spin in the collinear ordered state, labeled "collinear, flip 1" in Fig 6.5a, follows the bicollinear energy quite closely. Because this cost decreases with pressure, we can surmise that magnetic fluctuations become more energetically available as pressure is increased.

6.3.4 Optical excitations and magnetism

The direct optical gap was calculated by promoting the highest energy orbital in the Slater determinant part of the trial wavefunction to the next excited state orbital. This constructs a wave function *ansatz* for an electron-hole excitation. The results are shown in Fig 6.6. The resulting DMC(PBE0) energy relative to the DMC(PBE0) ground state is our estimation of the gap. Interestingly, the DMC(PBE0) gap is within statistical uncertainties of 0 despite the fact PBE0 estimates a rather large gap, regardless of magnetic ordering. Only the checkerboard state is gapped according to DMC(PBE0).

The charge degrees of freedom are therefore coupled to the spin degrees of freedom. According to these calculations, in FeSe there is a coupling between the mobility of charge and the spin ordering. In the remainder of the paper, we will correlate these properties with those of the ground state for different spin orderings.

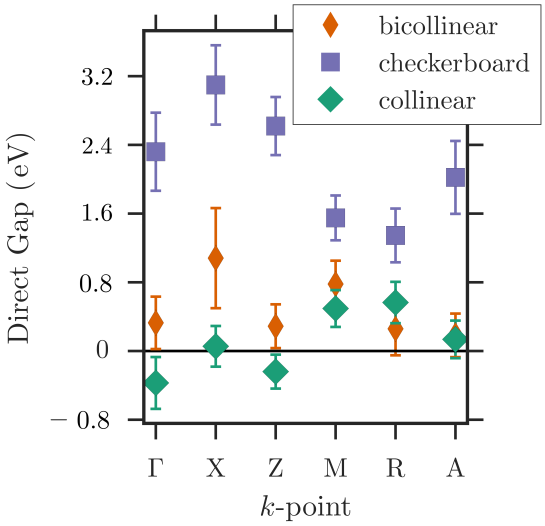

Figure 6.6: Gap as a function of twisted boundary conditions calculated within DMC(PBE0). For the stripe-like magnetic states, the gap is zero within statistical error. The unit cell is a 2×2 supercell, expanded in the x-y plane, shown as one of the four outlined boxes in each of the spin densities of Fig. 6.1. [Note: this figure has been updated from the published version to correct an mistake in the units of the gap.]

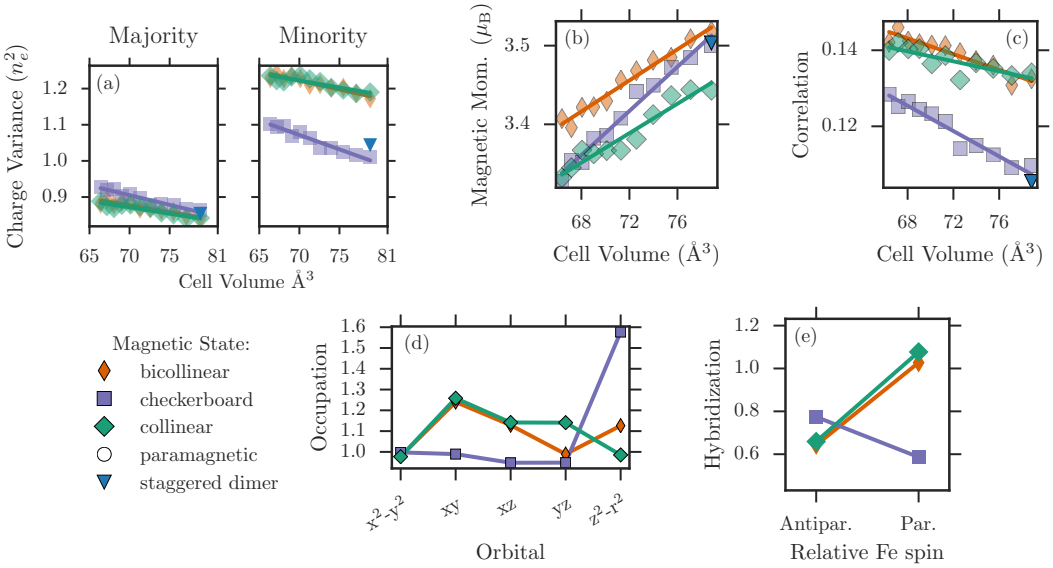

Figure 6.7: **(a)** Charge variance, in units of number of electrons squared for different magnetic orderings in the majority and minority spin channel, as a function of cell volume, illustrating that the minority spin channel is more mobile, and additionally that the checkerboard ordering's electrons are more constrained to a given iron site. **(b)** Magnetic moments inside each iron's Voronoi polyhedron. **(c)** Magnitude of on-site correlations, measured by $|\mathrm{Cov}(n^\uparrow, n^\downarrow)|/[\mathrm{Var}(n^\uparrow)\mathrm{Var}(n^\downarrow)]^{1/2}$. **(d)** Single-particle orbital occupations of the iron d-states, measured by the on-diagonal terms of the 1-RDM. Note checkerboard's charge density points mostly out of the iron plane, while the other orderings point mostly within the plane. **(e)** Hybridization of different orderings, as measured by an average of the off-diagonal elements of the 1-RDM, broken down by interactions between antiparallel (Antipar.) aligned irons and parallel (Par.).

6.3.5 Interaction of charge and orbitals with magnetism

From the energetic properties, we note two classes of magnetic order in FeSe: ones which are stripe-like, and ones which are not stripe-like. The stripe-like orderings converge in energy with pressure, while the checkerboard and staggered dimer pattern increases in energy relative to those orderings. Similarly, the gap calculated in DMC(PBE0) distinguishes between different orderings, with metallic character in the stripe-like ordering. In this section, we will make the following observations:

- Compared to majority electrons, minority spin electrons are more mobile and are more affected by the spin ordering.
- The one-particle orbitals are occupied differently depending on the spin ordering.

These effects combine to give a cartoon picture of the physics that explains the difference in pressure behavior between the magnetic orders.

Character of minority and majority spin electrons. To characterize the differences between the spin channels, we evaluate the local charge compressibility of the Fe sites: $\langle (n_{i,\sigma} - \langle n_{i,\sigma} \rangle)^2 \rangle$, where n_{i_σ} is the number of electrons within a Voronoi polyhedron around the ith Fe site of spin σ. Larger values of the compressibility indicate electrons are more likely to hop between atoms. For a Fe atom with net $\uparrow$ spin, the $\uparrow$ electrons are labeled majority electrons and the $\downarrow$ minority, and vice versa for Fe atoms with net $\downarrow$ spin.

In Fig 7a, these results are presented. For all magnetic orders, the majority spin is very similar and shows a low local charge compressibility, while the minority spin is different between different magnetic orders, and its local charge compressibility is larger than the majority channel by around 0.3 n_e^2 (electron number squared). This suggests the minority electrons are more mobile, however, their ability to hop is affected by the local magnetic order. For the stripe-like orders, the minority electrons are least constrained, and their minority channel compressibility is about 0.1 n_e^2 more than the checkerboard and dimer state. This measure of mobility seems to be correlated with the optical gap calculations, which predict that the checkerboard pattern induces a gap in contrast to the other magnetic orders.

One particle orbitals. In Fig 6.7d, we present the orbital occupation of the d orbitals in different spin orderings. For stripe-like orderings, the xy, xz, and yz orbitals are occupied, in agreement with ARPES results [259]. On the other hand, the $3z^2 - r^2$ orbital is occupied for the checkerboard ordering. This gives a simple explanation for the differences in the local charge compressibility: The checkerboard pattern causes the minority spin to occupy the out of plane orbital, which would rise to an insulating state if it were the ground state. This idea can be confirmed by checking the off-diagonal one-particle density matrix

elements between Fe atoms with parallel and antiparallel net spins, in Fig 6.7e. The atomic orbitals are more hybridized between parallel spin Fe atoms for the stripe-like orders. The charge degrees of freedom, which are mainly the minority spins from the Fe, interact strongly with the magnetic ordering. This effect also interacts with the net magnetic moment and on-site correlations (Fig 6.7b and Fig 6.7c).

6.3.6 Hund's coupling and the connection to spin-charge coupling

The importance of Hund's coupling in tuning correlation effects of multiband materials has been extensively demonstrated by means of dynamical mean field theory (DMFT) calculations [268, 267, 269]. These results highlighted its role in determining the bad metallic behavior in iron-based superconductors [270, 271], which are therefore sometimes referred as Hund's metals. DMFT studies of $BaFe_2As_2$ have predicted that kinetic energy should be lower in the paramagnetic state, although the total energy is lower in the spin-polarized states due to Hund's coupling [263]. Correspondingly, we find that comparing the paramagnetic state and collinear state, the kinetic energy is 21.5(8) eV/f.u. larger in collinear, while the total energy is 1.75 eV/f.u. lower for collinear. Also due to Hund's coupling, DMFT studies have predicted that the high-spin state should be the only highly probable state [272]. Correspondingly, we find that the iron magnetic moment fluctuates around 3.4 μ_B, with a standard deviation of 1.5 μ_B.

A simple picture based on Hund's coupling can explain the energetics and other properties presented in the results section. Hund's rules dictate that for an atom with a partially filled shell, we expect the electrons to have total spin S that maximizes the multiplicity $2S+1$. This is consistent with our computed magnetic moment, which find that the majority channel is mostly filled, bringing the moment to around 3.1-3.4 μ_B. The spin occupation of the d-states in a reference iron is diagrammatically shown in the top row of Fig. 6.8. Also due to Hund's coupling, the electron that is most likely to hop to nearby iron atoms would be the electron in the minority channel, to keep a large S. As illustrated in Fig. 6.8, this minority channel is already filled for neighboring irons that are antiparallel, so only majority spin electrons can hop to those atoms. Conversely, minority electrons can hop to neighboring parallel irons, since that spin channel is not filled. Thus, irons with parallel spins allow the minority electrons to more easily hop about the aligned iron sites, therefore decrease the kinetic energy. As seen in Fig. 6.7d the magnetic ordering affects the occupation of the d states, hence affects the labeling of the states in Fig. 6.8, but the basic idea is unchanged.

While the minority spins require at least some parallel iron magnetic moments, the large localized magnetic moments also interact antiferromagnetically, leading to a competition between these two mechanisms. As a compromise, antiferromagnetic configurations with ferromagnetic chains emerge as the lowest energy configurations.

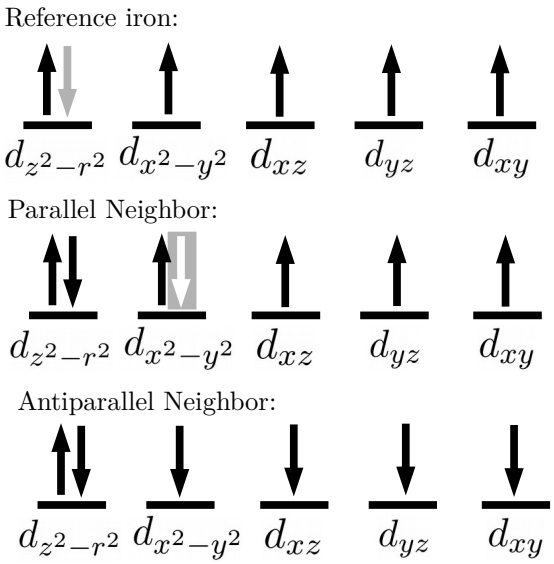

Figure 6.8: Diagrams depicting the occupations of the d-orbitals of a reference iron, one of its neighbors with parallel net magnetic moment, and another neighbor with antiparallel magnetic moment. The minority channel is spin down for the top two, and is spin up for the last. The minority electron on the reference atom is most likely to hop to a neighbor, for example, the greyed out down electron on $d_{z^2-r^2}$. It may easily hop to its parallel neighbor, which may fill its $d_{x^2-y^2}$ orbital as suggested by the grey box. It may not hop to any of the orbitals of the antiparallel neighbor, since the down spin channel is filled. Any hopping from the reference iron to its antiparallel neighbor must occur in the spin-up channel, which consequently violates Hund's rule for the reference iron.

This picture unifies many of the observations from our calculations. The checkerboard state is distinguished from the other states by its lack of parallel nearest neighbors, similar to how the ferromagnetic state is distinguished by its lack of antiparallel neighbors. These two extremes are higher in energy, and are disfavored as pressure increases the importance of Fe-Fe interactions. Because the checkerboard has no parallel nearest neighbor, its iron d-electrons are more trapped on a single site, leading to a low charge variance, and states that primarily occupy the $d_{z^2-r^2}$ orbital. All stripe-like states have a combination of antiparallel and parallel nearest neighbors, and allow the electrons to delocalize along the irons chains, leading to higher correlations, higher variance, and more Fe-Fe hybridization. Although the staggered dimer ordering is energetically competitive at low pressures, its energy, charge variance, and magnetic moment are similar to checkerboard, and at high pressures, becomes energetically unfavorable just as the checkerboard ordering does. Although the staggered dimer does allow some delocalization between the dimered parallel spins, the itinerant spins are still trapped on the dimers, and therefore this state's energetics follow the checkerboard behavior at higher pressures.

This competition of interactions sets up a fine balance between many qualitatively different magnetic configurations. Parameters in the structure can tilt this balance one way or another, leading to a strong magneto-structural coupling. This is evident both from the strong magnetic dependence of the bulk modulus in Fig. 6.3, as well as in Fig. 6.4, where z_{Se} can exchange the ground state configuration between at least two magnetic configurations. This logic can be straightforwardly applied to iron telluride (FeTe), the non superconducting parent compound of FeSe. This material has the ground state magnetic ordering at a z_{Te} around 1.75 Å, which implies that the z_{Te} should be decreased to force a crossover. By this logic, FeTe would superconduct if it were put in tensile stress, as it has been observed [288].

6.4 Conclusion for bulk-FeSe

In summary, we have shown that QMC calculations can obtain an accurate description of the electronic structure of FeSe. The lattice constants and bulk modulus are all very close to the experimental values and significantly improve over DFT calculations. Our results are substantiated by the agreement between different and complementary QMC techniques employed. We showed that they yield sufficiently small statistical and systematic errors to study the relative energetics of different magnetic orders, which behave differently from those predicted by DFT. The largest error in the calculations appear to be due to finite size supercells, which we checked to be small enough that the trends presented here are preserved.

As an outcome of the high-accuracy calculations, we have determined that collinear and bicollinear

motifs become close in energy as pressure increases, while the checkerboard motif increases in energy with pressure. This behavior is correlated with delocalization of the minority electrons on the high-spin Fe atom. Collinear and bicollinear motifs allow for more delocalization, which increases in importance as the pressure is increased. This delocalization effect is strong enough to change the occupation of atomic orbitals in FeSe depending on the magnetic ordering, so it is larger than the crystal field splitting of the orbitals. The spontaneous breaking of C_4 symmetry (or more properly S_4 symmetry)[289, 290], is a result of this physics. Magnetic configurations which contain spin chains are thus favored over the whole considered range of pressure.

From the above results, we can see that the magnetic degrees of freedom are strongly coupled with the charge and orbital degrees of freedom. In a similar way, since the relative magnetic energies are dependent on the hopping of minority electrons from site to site, they are also strongly dependent on the structure. There is thus both spin-charge and spin-structural coupling in this system. As one of us showed recently[123, 124], the cuprates also show strong magneto-structural and magneto-charge coupling. One might speculate that both of these effects are necessary for high T_c and it may prove fruitful to look for similar effects in proposed new superconductors.

6.5 Supplemental information

6.5.1 Convergence and validation

In this appendix we present an extensive study of the convergence of the main parameters involved in our QMC calculations. Within DMC(PBE0), the only parameter to be optimized in the Slater determinant is the amount of exact exchange w. The optimization of FN-DMC energy as a function of w is presented in Fig 6.10. As already mentioned in the main manuscript, we notice that the best FN-DMC is generally obtained with $\sim 25\%$ of exact exchange for all magnetic configurations; this corresponds to the PBE0 density functional. The convergence of the FN-DMC energy with other parameters of QMC methods is reported in Fig 6.9. For the DMC(PBE0) method, in Fig. 6.9b, we present energy convergence as a function of Fe and Se basis set exponents by showing the behavior of the exponent of our most diffuse gaussian basis exponent as it gets more diffuse. Benchmark calculations of DMC(PBE0) against the time step used in the projection are presented in Fig 6.9d. We employed a time step of 0.01 for all DMC(PBE0) calculations. On the other hand, lattice regularized FN-DMC algorithm employed for DMC(opt) method (see next section) suffers from the lattice step error in Laplacian discretization. Convergence with lattice step is shown for the collinear configuration in Fig 6.9f. We used a lattice step of 0.125 a.u. for all DMC(opt) calculations.

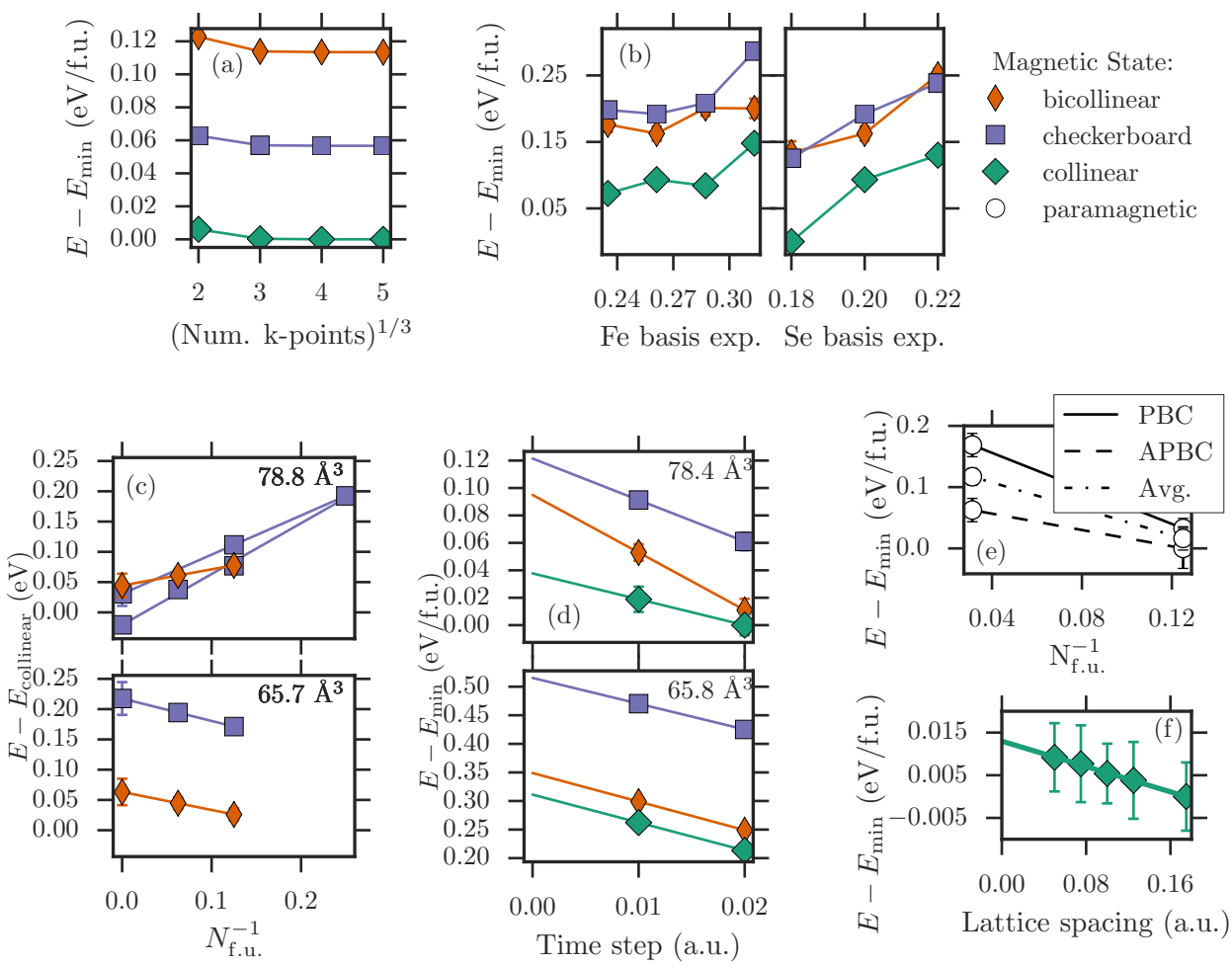

Figure 6.9: Convergence of DFT and DMC parameters. Axes labeled by $E - E_{\min}$ are energies relative to the minimum energy of the points in the subfigure. (a) Convergence of k-point grid for DFT calculations for the 8 f.u. cell. A $4 \times 4 \times 4$ grid was used for all these calculations. (b) Convergence of DMC(PBE0) basis set parameters for the 8 f.u. cell, at zero pressure. "Fe basis exp" and "Se basis exp" refer to the value of the smallest exponent in the basis. Values of around 0.26 and 0.2 were used for Fe and Se respectively. While in the latter case the total energy is decreasing, the energy differences are stable. (c) Finite size extrapolation for DMC(PBE0) at the largest and smallest volumes considered, twist averaging over 8 boundary conditions. Energy is relative to the collinear energy for each size. The two checkerboard lines reflect a finite size extrapolation in the $\hat{z}$ direction (upper line) and extrapolation in the x-y plane (lower line). The full extrapolation will likely be near the center of the two line endpoints. (d) Time step extrapolation for the DMC(PBE0) at 8 f.u. at the largest and smallest volumes considered. A value of 0.01 a.u. was adopted for all DMC(PBE0) calculations. (e) Finite size extrapolation for the DMC(opt) calculations, with periodic (PBC) and antiperiodic (APBC) boundary conditions, along with their average (Avg.). These benchmark calculations are performed in the paramagnetic phase and energies are corrected for one-body and two-body finite size errors. (f) Extrapolation of the lattice spacing used for the laplacian discretization for the LR-DMC, i.e. DMC(opt), calculations. These benchmark calculations are performed in the collinear phase. A value of 0.125 a.u. was adopted for all calculations.

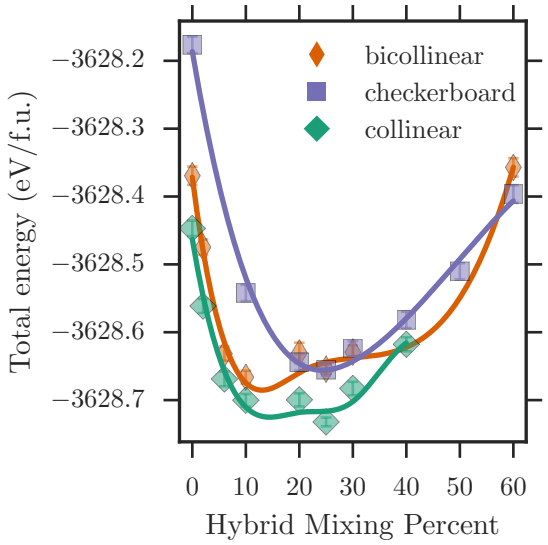

Figure 6.10: DMC optimization of exchange correlation functional for the DFT calculations. The exchange-correlation function depends on w as $E_{\mathrm{xc}}^{w}[n] = wE_{\mathrm{x}}^{\mathrm{HF}}[n] + (1-w)E_{\mathrm{x}}^{\mathrm{PBE}}[n] + E_{\mathrm{c}}^{\mathrm{PBE}}[n]$. Lines are a cubic spline interpolation as a guide to the eye.

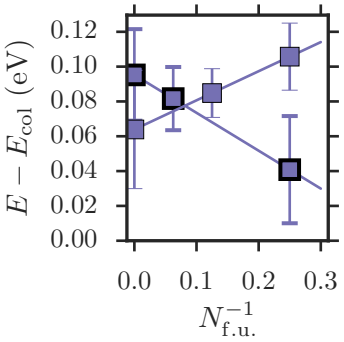

Figure 6.11: Finite size extrapolation near $z_{\mathrm{Se}} = 1.42$ of the energy differences between collinear and checkerboard magnetic ordering for DMC(opt) (thick outline) an DMC(PBE0) (thin outline). DMC(opt) data points are averaged over periodic and fully antiperiodic boundary conditions, while DMC(PBE0) is averaged over 8 twists. The extrapolations are in agreement within statistical error.

We turn now our attention to finite size errors (FSE) which represent the main source of error in our QMC calculations. We performed several DFT test calculations to determine the impact of one-body FSE. For both 8 f.u. and 16 f.u. supercells (used for DMC(PBE0) and DMC(opt) methods respectively) a 4x4x4 k-point grid is enough to obtain results converged within 1 meV independently from the density functional used, as shown in 6.9a. The same k-point grid in the PBE0 wavefunction is also sufficient to converge FN-DMC energies within the same threshold. For the DMC(PBE0) calculations, we twist average over a set of 8 twist conditions [278], for unit cells ranging from 4 to 16 f.u., expanding the supercell in the x-y plane, and z direction (adding an additional layer). The resulting finite-size extrapolations are depicted in Fig 6.9c. The finite size extrapolation in the z direction is the checkerboard line above the other checkerboard line. The true infinite size limit will likely lie in between these two extrapolations. Although the finite size effects are relevant, they do not alter any conclusions of the main text. Going from low to high pressure, the finite size errors amplify the change in energy differences between checkerboard and collinear. Extrapolating with more than two points is prohibitively expensive for the bicollinear state, and so how finite size effects affects the pressure dependence of the energy differences between collinear and bicollinear is not clear, as the extrapolations are within error bars. However, it is certainly clear that bicollinear both remains very close in energy to the collinear state—even in the extrapolation—whereas checkerboard's energy certainly rises well above the other states.

For DMC(opt), all calculations have been done with a 16 f.u. supercell. Structural optimization was performed with periodic boundary conditions only. All other calculations were instead averaged between periodic (PBC) and fully antiperiodic (APBC) boundary conditions. Further finite size corrections to DMC(opt) energies are obtained by adding one-body corrections estimated from fully converged DFT-LDA calculations and two-body corrections evaluated within the KZK approach [291, 292]. In Figure 6.9e is reported the convergence of DMC(opt) energy in the paramagnetic phase as a function of the system size after applying the corrections.

We verified that DMC(PBE0) and DMC(opt) are in agreement when the calculation is carried out with exactly the same setup. For this purpose, we used a small 4 f.u. supercell in the collinear configuration at the Γ-point. We computed the optimal Se height by fitting the total energy curve with both methods and we found 1.46(1) Å for the DMC(opt) method and 1.40(5) Å for the DMC(PBE0) method. The two values lies within one standard deviation of each other, and we consider them in statistical agreement.

Finally, we check the impact of finite size errors on the energy differences between collinear and checkerboard orderings. For this purpose, we compared finite size extrapolations at a fixed $z_{\mathrm{Se}} \approx 1.42$ with the typical setup employed for production runs, i.e. 8 f.u. averaged over 8 twists for DMC(PBE0) and 16 f.u.

averaged over periodic and fully antiperiodic boundary conditions for DMC(opt). The results are presented in Fig. 6.11. We found that the extrapolations as well as the larger cell sizes we used were within statistical error. This suggests that the fixed node error of DMC(PBE0) when compared to the best Jastrow-correlated single-deteminant wavefunctions is below statistical errors with respect to magnetic energy differences. It is possible that this fixed node error is still larger than our statistical errors when comparing to the exact energy differences, however, this would require investigation beyond Jastrow-correlated single-determinant trial wavefunctions, which due to computational complexity, we leave for another study.

Chapter 7

Low-energy description of FeSe molecule from first-principles

The work in this chapter was reported in H. Zheng, H. J. Changlani, K. T. Williams, B. Busemeyer, and L. K. Wagner, "From Real Materials to Model Hamiltonians With Density Matrix Downfolding," *Front. Phys.*, **6**, (2018). I have performed all the calculations presented in this chapter. One of the goals of first-principles downfolding is to determine minimal descriptions for complex systems. This chapter presents a strategy for using density matrix downfolding to find a minimal model for a transition metal system.

Transition metal systems are often difficult to model because the low energy physics involves multiple orbitals and various kinds of couplings. This is seen in the proliferation of models for transition metals, which include terms like spin-spin coupling, spin-orbital coupling, hopping, Hund's coupling, and so on. Models containing all possible descriptors are unwieldy, and it is difficult to determine which degrees of freedom are needed for a minimal model to reproduce an interesting effect. Transition metal systems are challenging to describe using most electronic structure methods because of the strong electron correlations and multiple oxidation states possible in these systems. Fixed-node DMC has been shown to be a highly accurate method on transition metal materials for improving the description of the ground state properties and energy gaps [107, 123, 41, 89]. In this chapter, we applied DMD using fixed-node DMC to quantify the importance of different terms in the effective Hamiltonian in a FeSe diatomic molecule with a bond length equal to that of the iron based superconductor, FeSe [6], in order to help identify the descriptors that may be relevant in the bulk material. We considered a low-energy space spanned by the Se $4p$, Fe $3d$, and Fe $4s$ orbitals. We sampled singles and doubles excitations from a reference Slater determinant of Kohn-Sham orbitals taken from DFT calculations with PBE0 functional with total spin 0, 2, and 4, which were then multiplied by a Jastrow factor and further optimized using fixed-node DMC. After this procedure, 241 states were within a low energy window of 8 eV. Of these, eight states had a significant iron $4p$ component, which excludes them from the low-energy subspace. This left us with 233 states in the low-energy subspace.

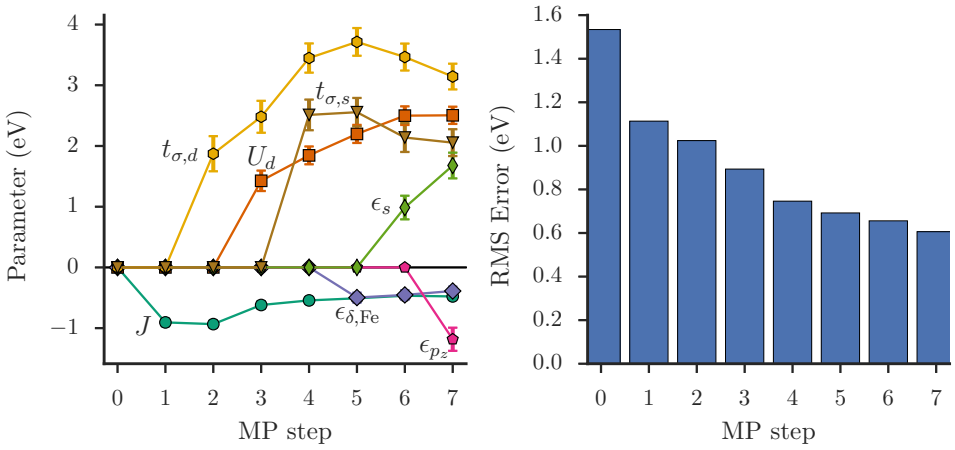

Figure 7.1: (Left) Parameter values for each fit generated in the MP algorithm, labeled at the step where they are included in the model. A zero value indicates that parameter is not yet added to the model. The sign of J is consistent with Hund's rules, and the signs of $t_{\sigma,d}$ and $t_{\sigma,s}$ are consistent with Se being located in positive z with respect to Fe. (Right) RMS error of each model generated by MP as the algorithm includes parameters. The RMS error of the largest model considered was 0.61 eV.

7.1 Downfolding procedure

We considered a set of 21 possible descriptors consisting of local operators on the iron $4s$, iron $3d$ states, and selenium $4p$ states, which is a total of 9 single-particle orbitals. We used the intrinsic atomic orbital construction [293] to generate an efficient localized basis set. At the one-body level, we considered orbital energy descriptors:

$$\begin{aligned} &\epsilon_s n_s, && \epsilon_{\pi,\mathrm{Se}}(n_{p_x}+n_{p_y}), && \epsilon_z n_{p_z}, \\ &\epsilon_{z^2} n_{d_{z^2}}, && \epsilon_{\pi,\mathrm{Fe}}(n_{d_{xz}}+n_{d_{yz}}). && \epsilon_\delta(n_{d_{xy}}+n_{d_{x^2-y^2}}), \end{aligned} \tag{7.1}$$

The labels π and δ signify that these are the π and δ-bonding orbitals for each atom. We also considered the symmetry-allowed hopping terms:

$$t_{\sigma,d}\sum_\eta \left(c^\dagger_{d_{z^2},\eta}c_{p_z,\eta}+\mathrm{h.c.}\right), \quad t_{\sigma,s}\sum_\eta \left(c^\dagger_{s,\eta}c_{p_z,\eta}+\mathrm{h.c.}\right), \quad t_\pi \sum_\eta \left(c^\dagger_{d_{xz},\eta}c_{p_x,\eta}+c^\dagger_{d_{yz},\eta}c_{p_y,\eta}+\mathrm{h.c.}\right). \tag{7.2}$$

As before, η represents the spin index. At the two-body level, we considered Hubbard interactions:

$$U_p \sum_{i\in p} n_{i,\uparrow} n_{i,\downarrow}, \qquad U_{d,\delta} \sum_{i\in\{d_{xy},d_{x^2-y^2}\}} n_{i,\uparrow} n_{i,\downarrow},$$

$$U_d \sum_{i\in d} n_{i,\uparrow} n_{i,\downarrow}, \qquad U_{d,\pi} \sum_{i\in\{d_{xz},d_{yz}\}} n_{i,\uparrow} n_{i,\downarrow}, \qquad U_{d_{z^2}} n_{d_{z^2},\uparrow} n_{d_{z^2},\downarrow}, \tag{7.3}$$

where p refers to the Se-4p orbitals and d refers to the Fe-3d orbitals. Importantly, we also accounted for the Hund's coupling terms for the iron atom:

$$J \sum_{\substack{i\neq j \\ i,j\in d}} S_i \cdot S_j, \qquad J_\delta S_{d_{xy}} \cdot S_{d_{x^2-y^2}}, \qquad J_{\delta,d_{z^2}} (S_{d_{xy}} + S_{d_{x^2-y^2}}) \cdot S_{d_{z^2}},$$

$$J_\pi S_{d_{xz}} \cdot S_{d_{yz}}, \qquad J_{\pi,d_{z^2}} (S_{d_{xz}} + S_{d_{yz}}) \cdot S_{d_{z^2}}. \qquad J_{\pi,\delta} (S_{d_{xz}} + S_{d_{yz}}) \cdot (S_{d_{xy}} + S_{d_{x^2-y^2}}), \tag{7.4}$$

Finally, we also added a nearest neighbor Hubbard interaction: $V \sum_{i\in p, j\in d} n_i n_j$.

7.2 Results

To generate a minimal description of the system, we employed a matching pursuit (MP) method [225]. MP chooses to add descriptors based on their correlation with the residual of the linear fit. We started with a model that only consists of E_0. The Hund's coupling descriptor [the first term in Eq. (7.4)] has the largest correlation coefficient with the residual fit, so it is added first. The fact that the Hund's coupling is chosen first in MP is consistent with several studies in the literature which show that it is important for the magnetic properties of bulk FeSe [267, 268, 269], as well as the result from Chapter 6. Next, MP includes the descriptor that correlates most strongly with the residuals of this first minimal model, in this case the hopping between d and p σ-symmetry orbitals. We repeated this procedure until the RMS error did not improve more than 0.05 eV upon adding a new parameter. This criterion was chosen to strike a balance between the complexity of the model and the accuracy in reproducing the data set.

The following model was produced:

$$\begin{aligned} H_{eff} &= \epsilon_{\delta,\mathrm{Fe}}(n_{d_{xy}} + n_{d_{x^2-y^2}}) + \epsilon_s n_s + \epsilon_z n_{p_z} \\ &\quad + t_{\sigma,d} \sum_{\eta} \left(c^{\dagger}_{d_{z^2},\eta} c_{p_z,\eta} + \mathrm{h.c.} \right) + t_{\sigma,s} \sum_{\eta} \left(c^{\dagger}_{s,\eta} c_{p_z,\eta} + \mathrm{h.c.} \right) \\ &\quad + U_d \sum_{i \in d} n_{i,\uparrow} n_{i,\downarrow} + J \sum_{\substack{i \neq j \\ i,j \in d}} S_i \cdot S_j + E_0. \end{aligned} \tag{7.5}$$

E_0 is an overall energy shift, also included as a fit parameter. The parameter values and corresponding error of each model produced by MP are shown in Figure 7.1. Note that all parameters may change at each step because the entire model is refitted when an additional parameter is included in each iteration. The parameters are smoothly varying with the inclusion of new parameters, and they take the correct signs based on symmetry (where applicable). The RMS error decreases with each additional parameter, but less so as the algorithm appends additional parameters. Eventually the diminishing improvements do not merit the additional complexity of more parameters.

In summary, these calculations demonstrated a practical procedure for quantifying the importance of model parameters: the matching pursuit order, which is determined by the correlation coefficients with either the energy or the residual of previous fits. The procedure confirmed the importance of Hund's coupling in a direct and unbiased way—the importance of the term is quantified by the correlation of the Hund's coupling descriptor, $\langle \sum_{\substack{i \neq j \\ i,j \in d}} S_i \cdot S_j \rangle$, with the energy. The Coulomb repulsion is also important in this system, as it appeared 3rd in the matching pursuit order. Quantifying the importance of model interactions helps describe the system and can determine practical effective minimal models.

Chapter 8

Prediction of the singlet-triplet gap of $MgTi_2O_4$

The work in this chapter was reported in B. Busemeyer, G. J. MacDougall, and L. K. Wagner, "Prediction for the singlet-triplet excitation energy for the spinel $MgTi_2O_4$ using first-principles diffusion Monte Carlo," *Phys. Rev. B*, **99**, 8, 081118, (2019). This work presents a simple application of downfolding to make a prediction for experiments. Publishing calculations ahead of experiments is an important step towards demonstrating the predictive capability of downfolding FN-DMC calculations.

The spinel, $MgTi_2O_4$, undergoes a transition into a dimerized state at low temperatures that is expected to be a spin singlet. However, no signature of a singlet-triplet transition has been discovered, in part due to the difficulty of predicting the energy of the transition from theory. We find that the dimers of $MgTi_2O_4$ can be described by a Heisenberg model with very small interactions between different dimers. Using high-accuracy first-principles quantum Monte Carlo combined with a novel model-fitting approach, we predict the singlet-triplet gap of these dimers to be 350(50) meV, a higher energy than previous experimental observations have considered. The prediction is published in advance of experimental confirmation.

8.1 Nature of the ground state of $MgTi_2O_4$

Exotic electronic states are predicted to occur at low temperatures in geometrically frustrated lattices, including the pyrochlore lattice[294, 295]. However, as temperature is decreased, the frustration is often resolved by structural distortions. Because these systems have strong electron-electron interaction effects, the resultant ground states can be challenging to describe using simple electronic structure theories. The causation of this distortion is not always completely understood, and the correlated nature of the material makes theoretical approaches challenging.

In the case of pyrochlore $MgTi_2O_4$, the high temperature pyrochlore lattice distorts to a dimerized structure at $T_s = 260$ K[296]. A spin-singlet state would not be surprising in this case, since there is a sharp decrease in the magnetic susceptibility coincident with the dimerization[297]. Existence of the singlet ground state is also indirectly supported by optical experiments[298] interpreted through density functional

theory (DFT) calculations with the B3LYP functional[296]. Local spin density approximation (LSDA) + U calculations find that at nonzero U, the ground state contains antiferromagnetic dimers[150]. However, both generalized gradient approximation (GGA) and local density approximation (LDA) + U with $U < 6$ eV fail to produce the insulating state, highlighting the dependence of the results on the choice of DFT functional. An additional concern with the spin-singlet identification is that neutron scattering experiments of $MgTi_2O_4$ find no singlet-triplet excitation up to energies of 25 meV[295]. We are not aware of any attempt to predict the singlet-triplet gap of the system from first-principles calculations.

Another system, VO_2, is quite similar to $MgTi_2O_4$ in that it undergoes a metal-insulator transition at low temperatures simultaneously with a structural transition that forms dimers. An inelastic x-ray scattering measurement found the singlet-triplet gap of VO_2 to be 460 meV[299]. Diffusion Monte Carlo (DMC) was applied to compute the singlet-triplet gap of VO_2, finding the gap to be 440(24) eV—within statistical errors of the experiment[41, 125]. The analysis used the DMC calculations to fit a model Heisenberg Hamiltonian, which can be solved for the excitation energies. Similar techniques have been successfully applied widely in the literature, including calculations utilizing quantum Monte Carlo[300, 301, 105, 302, 303, 106, 304, 107, 41]. Recently, the method was generalized and given the theoretical grounding to fit a large family of models, including Hubbard and generalized Hubbard models[210], which would give access to additional types of excitation energies. However, to cleanly demonstrate its predictability, correct predictions with the method should be published before the experimental observation.

In this manuscript, we use quantum Monte Carlo calculations and a rigorous theory of effective models[210] to make a prediction for the singlet-triplet gap of $MgTi_2O_4$. The gap is predicted to be 350(50) meV, which should be observable using neutron scattering or reasonant inelastic x-ray scattering (RIXS) experiments. Observation of an excitation at the singlet-triplet gap would be strong evidence for the singlet ground state, and confirmation that our technique is a new predictive tool for calculation of excited state properties in transition metal systems.

8.2 Calculation details

We used a conventional recipe to perform the DMC calculations. To generate the trial functions, we employed single-Slater-Jastrow-type wave functions[90, 305, 275, 306]. The Slater determinant is provided by DFT calculations, which were performed by the CRYSTAL package[243]. In previous studies of hybrid functionals and fixed-node error, the PBE0 functional often provides the best nodes compared to other choices of common DFT functionals[275, 123, 41, 307], so we employed the PBE0 exchange-correlation functional for the DFT

calculations in this work. We used a local Gaussian triple-ζ with polarization (TZP) basis set for the PBE0 calculations. The Jastrow factor was energy-optimized with variational Monte Carlo within the QWalk package[90, 85]. Fixed-node diffusion Monte Carlo calculations were performed using QWalk, using T-moves to handle the nonlocal parts of the pseudopotential[209]. The timestep error was confirmed to be negligible for these quantities (Supplemental Information). All DMC energies were twist-averaged over the 8 real twist-boundary conditions.

We fit a nearest-neighbor Heisenberg model to our DMC data, and use it to calculate the singlet-triplet gap.

$$H_{\text{eff}} = J \sum_{\langle ij \rangle} S_i \cdot S_j \tag{8.1}$$

where $\langle ij \rangle$ represent the pairs of Ti in a dimer. Because each dimer is independent, the Hamiltonian is block diagonal with blocks corresponding to each dimer. Let $|\uparrow\uparrow\rangle$ represent the spin state on a single dimer with both spins up, and $|\uparrow\downarrow\rangle$ be the corresponding state with one spin up and one spin down, etc. Although not all of them are eigenstates, the expectation value of the energies of these states according to (8.1) are $-J/4$ for $|\uparrow\downarrow\rangle$ and $|\downarrow\uparrow\rangle$ and is $J/4$ for $|\uparrow\uparrow\rangle$ and $|\downarrow\downarrow\rangle$. Thus, knowing the correct difference between the expectation value of the energies of $|\uparrow\uparrow\rangle$ state and the $|\uparrow\downarrow\rangle$ state determines J. Similar approaches have been utilized in many systems to determine effective exchange couplings[300, 301, 105, 302, 303, 106, 304, 107, 41]. The singlet-triplet gap of this Hamiltonian is then

$$\langle\uparrow\uparrow|H_{\text{eff}}|\uparrow\uparrow\rangle - \langle s|H_{\text{eff}}|s\rangle = J/4 - (-3J/4) = J,$$

where $|s\rangle = (|\uparrow\downarrow\rangle - |\downarrow\uparrow\rangle)/\sqrt{2}$ is the singlet ground state.

Fixed-node DMC provided the estimated energy difference between $|\uparrow\uparrow\rangle$ and $|\uparrow\downarrow\rangle$ state for each dimer. Trial functions for each state are prepared by initializing the DFT state with the target spin configuration, achieving self-consistency, and checking that the resulting Kohn-Sham Slater determinant has the correct spin configuration. The spin densities of the Slater determinants for each state are shown in Fig. 8.1. We then optimize a two-body Jastrow factor for each Slater determinant generated this way, and use the resulting Slater-Jastrow wave function as the trial function for DMC. Beginning with each of these trial wave functions (with different spin densities), the fixed-node constraint fixes the overall spin symmetry as the DMC projection removes all the high energy components from the trial wave function. Thus the resulting fixed-node wave function represents low-energy states with the spins on each Ti corresponding to $|\uparrow\uparrow\rangle$ or $|\uparrow\downarrow\rangle$ on each dimer.

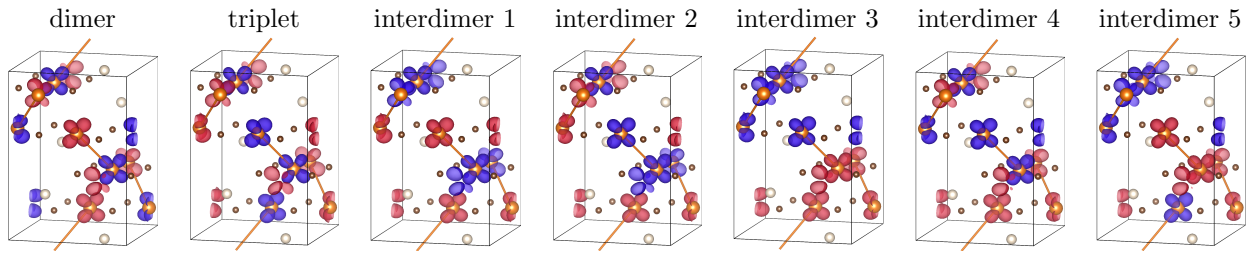

Figure 8.1: Spin density contour plot for the spin states considered in this work. Up and down spin densities are represented as blue and red. Orange atoms with spin are Ti atoms, of the spinless atoms, the smaller brown atoms are O, and the white atoms are Mg. Bonds are drawn between dimerized Ti atoms, and bonds that exit the unit cell have no Ti atom on the end outside the cell, which is drawn with black lines. The diffusion Monte Carlo energies of the dimer and triplet state determine the model, and the "interdimer" states are used to test the accuracy of the model.

8.3 Results

We evaluated the energetics of the "dimer" and "triplet" spin configurations presented in Fig. 8.1 to fit the dimer model (8.1). We also evaluated the energy of the spin-unpolarized state, finding it to be 810(30) meV higher than the "dimer" according to DMC and 898 meV according to PBE0. Net spin moments around each Ti are therefore energetically favorable in our calculations. The relative energy of the "triplet" state to the "dimer" state according to both PBE0 and DMC are presented in the "triplet" group of in Fig. 8.2. Requiring the model (8.1) to reproduce this relative energy constrains its parameter to be $J = 350(50)$ meV. Thus the singlet-triplet gap is predicted to be 350(50) meV.

To test the accuracy of the independent-dimer Heisenberg model (8.1), we compare its predictions for an additional test-set of states. An important approximation of the independent-dimer model is that it neglects interactions between different dimers. The Ti-Ti distance within a dimer is approximately 2.85 Å. There are two bonds that are 3.00 Å, two bonds that are 3.01 Å, and one long bond that is 3.16 Å. Considering the bond lengths, the intra-dimer interaction should be the strongest, with possible corrections due to interdimer interactions. The importance of these intermediate-distance interdimer interactions was checked by sampling additional "interdimer" states with different relative dimer orientations as well as different numbers of parallel and antiparallel intra-dimer alignment. For example, the state labeled "interdimer 1" in Fig. 8.1 will probe interdimer interactions, as it changes the relative orientations of the dimers. For all the states we calculated energies with DMC in Fig 8.2 and the unpolarized state, PBE0 tends to reproduce the DMC energy differences within 2–3σ (σ being the statistical uncertainty of the DMC results). Given the agreement with DMC and due to computational constraints, we only computed PBE0 as reference energies for interdimer 2–5, as these states are only used to probe the relevance of interdimer interactions. The independent-dimer model predictions appear in Fig. 8.2 along with the first-principle energy differences

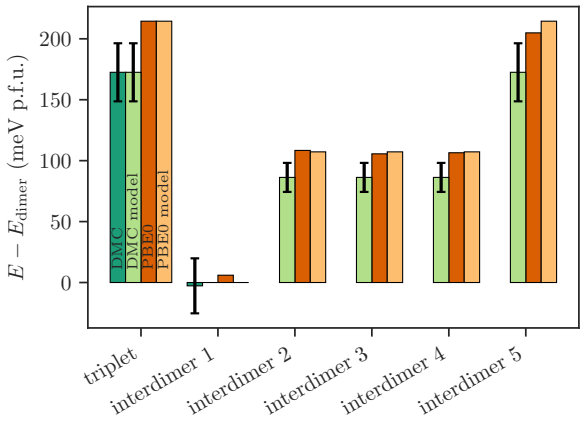

Figure 8.2: Energies of each state relative to the dimer state of Fig. 8.1 according to DMC and PBE0 as well as models fit to DMC and PBE0 data. The triplet energy difference is sufficient to fit the parameter in (8.1), with $J = 350(50)$ meV from DMC, for example. This makes the singlet-triplet gap 350(50) meV for this system. The interdimer states are predictions from the independent dimer model (8.1), and are used to test the predictability of the model. Because PBE0 reproduces the energy differences for the unpolarized, triplet, and interdimer state, PBE0 energies should be sufficient for interdimer 2–5, which are only used to probe the relevance of interdimer interactions. Due to computational constraints we did not also provide DMC energies for interdimer 2–5. The model predictions for the interdimer states agree quite well with (8.1), suggesting that the independent-dimer model is an accurate effective model for the spins in this system.

according to PBE0. The independent-dimer model can be fit to either the PBE0 or DMC triplet energy difference, and both resulting model predictions are presented in Fig. 8.2. The model predictions and reference energies agree within 10 meV, so the energy of these spin states only depends on intra-dimer interactions to high accuracy. Thus, the independent dimer model (8.1) seems to be an accurate minimal model for the spin degree of freedom of $MgTi_2O_4$.

The spin and charge density of the lowest energy state are shown in Fig 8.3. The spin and charge density in DMC is within statistical uncertainties of the Slater determinant of PBE0 orbitals, hence we show the trial function densities to avoid the statistical noise in DMC. The 2-d slices, shown in Fig. 8.3, are through nearest neighbor Ti atoms (intra-dimer) and through nearest neighbor Ti atoms in the x-y plane (interdimer). The spin density in the dimer bond is typical for systems interacting through superexchange; in particular, the spin density on the oxygen tends to be opposite the spin of the nearest Ti atom. In contrast, the interdimer pairs ligands' spin densities do not show any obvious superexchange pattern. There is an increase in Ti-O-Ti hybridization relative to the spin-unpolarized state, but only inside the dimer bond, as one can see from the increased charge density. The spin and charge densities show little increase in hybridization outside the dimers, consistent with the results from fitting the models above.

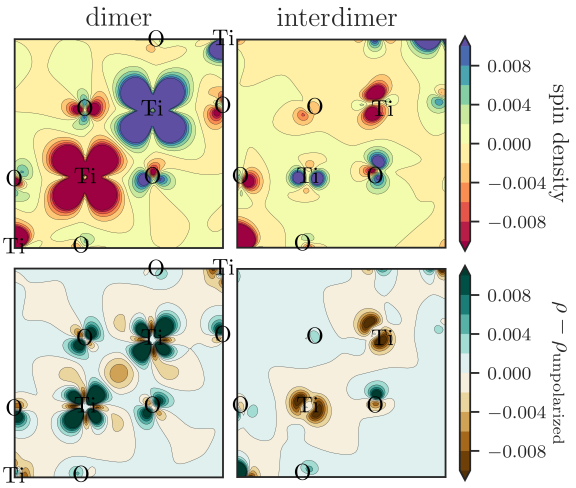

Figure 8.3: Spin density (top row) and charge density (ρ) relative to the unpolarized charge density $\rho_{\text{unpolarized}}$ (bottom row) through Ti pairs and their intermediate O. Dimer signifies the Ti atoms in the center form a nearest neighbor dimer pair in the structure. Inter-dimer signifies that the Ti atoms are nearest neighbors in the x-y plane. The dimer bond shows spin density typical for atoms interacting through superexchange, as well as an increase in hybridization between Ti and O within the dimer as compared to the unpolarized state. The interdimer bond shows no such signals of superexchange, in agreement with the model results.

8.4 Conclusion for $MgTi_2O_4$

We have found the singlet-triplet gap of $MgTi_2O_4$ using high-accuracy diffusion Monte Carlo calculations to be 350(50) meV. The approach utilizes a downfolding approach that had been applied successfully to VO_2[41] and a variety of other systems[210]. A second benefit of this approach is that it can evaluate the accuracy of minimal models, which can provide simplified views of complex materials. In this case, we found that a Heisenberg model with interactions between Ti inside a dimer but with independent dimers can accurately describe the low-energy spin states in the system. Experimental confirmation of the singlet-triplet gap should be possible in RIXS or neutron scattering. We are publishing this result in advance of an experimental measurement so that it constitutes a true prediction. If confirmed, this would be an example of a rare event in correlated electron physics–the prediction of a precise experimental result with quantitative accuracy, and cement diffusion Monte Carlo as a technique that can accurately predict properties of correlated electron materials.

8.5 Supplemental information

We converged the Brillioun zone sampling in the PBE0 calculations in Fig. 8.4. The total energies are already converged within the micro-eV scale with a $4 \times 4 \times 4$ grid, which is well below the scale of the energy

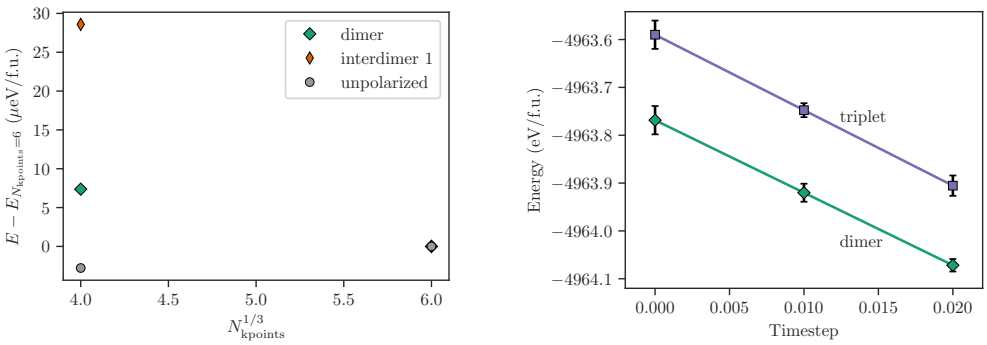

Figure 8.4: (left) Energy vs. Brillouin zone sampling for the PBE0 calculations. The energies are shown relative to the largest number of kpoints ($6 \times 6 \times 6$), so that the left point is zero by definition. The error in the total energies is converged to the micro-eV scale, which is well below the scale of other errors in our work. (right) Timestep extrapolation for the DMC calculations was performed with two points at 0.01 and 0.02 timestep. These points were extrapolated to zero timestep. The timestep error in the energy difference is well within our statistical error.

differences (hundreds of meV).

We converged the timestep error from the DMC simulations in Fig. 8.4. While the timestep error on the total energy is larger than the statistical error, this error completely cancels in any energy differences. The difference in extrapolated DMC energies match the difference in the 0.01 timestep energies within one standard error.

Chapter 9

Algorithm for the discovery of low-energy states

9.1 Approaches to finding low-energy states

A critical input into the downfolding procedure of §3.2 is a set of states in the low-energy Hilbert space spanned by the lowest few eigenstates of $\hat{H}$. Previous applications of the approach to extended systems have used mean-field calculations to generate a set of determinants as starting points for VMC and DMC calculations which generate the states. This can be an effective way to generate the states when properties of the desired excited states are clear, for example, the spin states of Chapter 8. Previous applications to fit spin and spin-phonon models, VO_2 [41] and a cuprate [123] are similar. In systems where Kohn-Sham excitations are reasonable approximations to low-energy states, QMC calculations initialized from these states can be used for the fitting [210]. In all these cases the approximate low-energy states of interest were clear *a priori*, and it was possible to use mean-field theory to generate nodes with the correct symmetries for them.

In cases where the low-energy states are not so clear, mean-field excitations may target the wrong states. For example consider FeSe, discussed in Chapter 6. In that chapter, PBE0 gave optimal nodal structure among the DFT functionals considered, so it may also give reasonable nodes for excited states. Fig. 9.1 shows the band structure of FeSe in the collinear spin texture according to PBE0. Consistent with other calculations using PBE0 [8], the bands feature an unphysical gap larger than 2 eV. In Chapter 6, Fig. 6.6 showed the result of using single-excitations to form the nodal surface for FN-DMC calculations, and computing the energy difference between that state and the ground state (note Fig. 6.6 is done in an 8 f.u. cell). This is an estimate of the optical gap at each k-point. The results show that the gap is reduced significantly, and is within statistical error of zero, however the errorbars are still quite large in that calculation. More recently, I converged the errorbars of the calculation further for the Γ-point optical gaps for the first few excited states in the 8 f.u. cell, finding them to be 0.8(2) eV, 1.3(2) eV, and 1.5(2) eV. While significantly reduced compared to the PBE0 gaps, the gaps are clearly nonzero, and the energy levels are larger than the scale seen in ARPES [40], which suggest they are on the order of 10 meV.

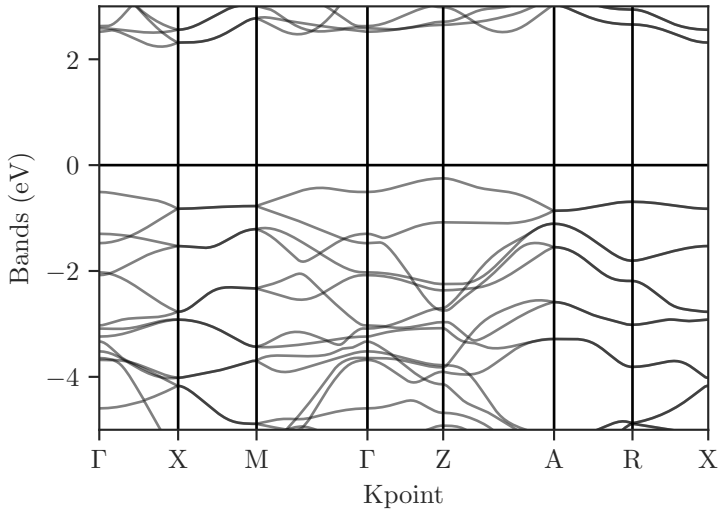

Figure 9.1: PBE0 band structure of FeSe with the collinear spin texture. The bands feature an unphysical gap of over 2 eV, consistent with other hybrid functional calculations [8].

As discussed in §6.3.5, the orbital occupations are coupled to the local spin texture in the system. This suggests that low-energy excitations of the system may require both orbital content and local spin texture to change. Using singles excitations to calculate gaps does not adjust the local spin to account for changes in the orbital content, and so may represent higher energy states. Altering the local spin texture requires many orbital excitations, and it is difficult to guess exactly how it should be adjusted.

The method presented in this chapter is a new approach to generating low-energy states that would handle this problem by modifying the orbitals and using variational Monte Carlo to optimize all other degrees of freedom, including the local spin texture. The approach modifies the objective function of the VMC algorithm, similar to other calculations which target excited states [93]. In this approach, the objective is not an eigenstate, but rather a low-energy wave function with density matrix elements that are different from the ground state. In §9.2, I introduce the objective functions and the variant of VMC I implemented to test out the approach. In §9.3, I apply the method to equilibrium and stretched H_2 to demonstrate how it works in a controlled system. The method was able to reproduce the first 3 excitation energies, compared to FCI. Unlike FCI, the method is capable of scaling to much larger systems.

9.2 Modifying the VMC objective function

As discussed in §2.1.4, VMC optimizes the parameters in $|\Psi_{\mathrm{T}}(\mathbf{P})\rangle$ by computing

$$\langle \hat{H} \rangle = \frac{\langle \Psi_{\mathrm{T}}(\mathbf{P}) | \hat{H} | \Psi_{\mathrm{T}}(\mathbf{P}) \rangle}{\langle \Psi_{\mathrm{T}}(\mathbf{P}) | \Psi_{\mathrm{T}}(\mathbf{P}) \rangle} \tag{9.1}$$

and adjusting $\mathbf{P}$, the parameters, to minimize the result. Instead of minimizing the energy alone, the algorithm minimizes the objective function

$$O(\mathbf{P}) = \langle \hat{H} \rangle + \lambda \frac{\langle \Psi_{\mathrm{T}}(\mathbf{P}) | \hat{d} | \Psi_{\mathrm{T}}(\mathbf{P}) \rangle}{\langle \Psi_{\mathrm{T}}(\mathbf{P}) | \Psi_{\mathrm{T}}(\mathbf{P}) \rangle}, \tag{9.2}$$

where $\hat{d}$ is an operator whose expectation value is a descriptor for the model (such as a density matrix element, see §3.2) and λ is a parameter that will move the state away from the ground state as it increases in magnitude.

To optimize this objective function, the Stochastic Reconfiguration (SR) method was applied [308, 309], with the Hamiltonian modified to be $\hat{H}_{\mathrm{mod}} = \hat{H} + \lambda \hat{d}$. The properties required for this modified SR method are already available in QWalk. The wave function was parameterized as

$$\Psi_{\mathrm{T}}(\mathbf{R}) = \sum_{i=1}^{4} c_i \Phi_{i,\uparrow}(\mathbf{R}) \Phi_{i,\downarrow}(\mathbf{R}) J(\mathbf{R}) \tag{9.3}$$

where $\Phi_{i,\sigma}(\mathbf{R})$ were the set of 4 determinants made up of the complete active space (CAS) of the σ bonding and antibonding orbitals from a spin-unrestricted DFT-B3LYP calculation. In this case, $\mathbf{P}$ represents $\{c_i\}_{i=1}^{4}$ and 7 parameters in the Jastrow factor.

9.3 Application to H_2

The approach was applied to fit a two-site Hubbard model of the form:

$$\hat{H}_{\mathrm{eff}} = t(\hat{c}_1^{\dagger}\hat{c}_2 + \hat{c}_2^{\dagger}\hat{c}_1) + U(\hat{n}_{\uparrow,1}\hat{n}_{\downarrow,1} + \hat{n}_{\uparrow,2}\hat{n}_{\downarrow,2}) + E_{\mathrm{ext}} \tag{9.4}$$

to fit a hydrogen molecule at approximately equilibrium length (0.74 Å) and stretched (2.0 Å). E_{ext} is a constant offset which is also a fit parameter. For these calculations, $\hat{d}$ was chosen for (9.2) to be $\hat{c}_1^{\dagger}\hat{c}_2 + \hat{c}_2^{\dagger}\hat{c}_1$. Large positive λ will push the state towards the bonding state and more negative values will push it towards an antibonding state. The system was chosen because it should be describable by a tight-binding model near

Table 9.1: Parameters, goodness of fit, and first three eigenvalues relative to the ground state for all calculations presented in this chapter. Energies are in units of Ha.

$d_{\mathrm{H-H}}$	calculation	t	U	R^2	E_1	E_2	E_3
0.74 Å	FCI	-	-	-	0.4881	0.5205	0.5846
	TB	-0.281	-	0.996	0.5627	0.5627	1.1254
	Hubbard	-0.291	0.107	0.999	0.5301	0.6375	1.1676
2.00 Å	FCI	-	-	-	0.031	0.286	0.320
	TB	-0.0577	-	0.864	0.1154	0.1154	0.2308
	Hubbard	-0.0569	0.3126	0.999	0.037	0.350	0.387

equilibrium, and as the bond is stretched, interactions should become important. Additionally the system is simple enough to solve nearly exactly using FCI.

9.3.1 H_2 with equilibrium bond length

Fig. 9.2 shows the result of tuning λ from 0.0 to 1.0 Ha, which is sufficient to shift the resulting state from the bonding to antibonding state. At $\lambda = 0.0$, the state shows $\langle \hat{c}_1^\dagger \hat{c}_2 + \hat{c}_2^\dagger \hat{c}_1 \rangle = 2$, meaning the bonding state is double occupied. The slope of the line is precisely the t parameter for tight-binding model describing the system. As discussed in the caption to Fig. 9.2, the fit with $t = -0.296$, $U = 0.0$ is a good fit for the system, with $R^2 = 0.996$. A negative t in (9.4) is consistent with a bonding ground state. A slight dip in the middle of Fig. 9.2 (a) is due to interaction effects: this state has little double-occupation, and therefore has lower interaction energy. Fitting both U and t will correct this so that the fit has $R^2 \approx 0.99989$.

Tab. 9.1 summarizes the fit parameters and resulting eigenvalues compared to a nearly exact FCI calculation (performed in a quadruple-ζ basis set). The gap between ground and first excited state from both models match FCI to roughly 10%. The next excited state gap is slightly more in disagreement with FCI, and the third state is significantly different. The source of error for the last state is that the model is fitting the space of the $1s$ orbitals of the hydrogen atoms only, and $2s$ or $2p$ states become significant in the FCI calculation for the third excited state.

9.3.2 H_2 with stretched bond length

When H_2 is stretched to 2.0 Å, it enters a correlated, magnetic ground state. In this situation, we would expect that the tight-binding model should be a poor description of the low-energy space. Fig. 9.3 shows the result of applying the constrained VMC routine to the stretched geometry, with λ varying enough to move from the bonding to the antibonding state once again. For this bond length, the tight-binding model is a poorer ($R^2 = 0.864$) description, with the error being proportional to the double occupation. This is an indication that a Hubbard-U term will correct the model. Fitting the t and U of this system brings the R^2

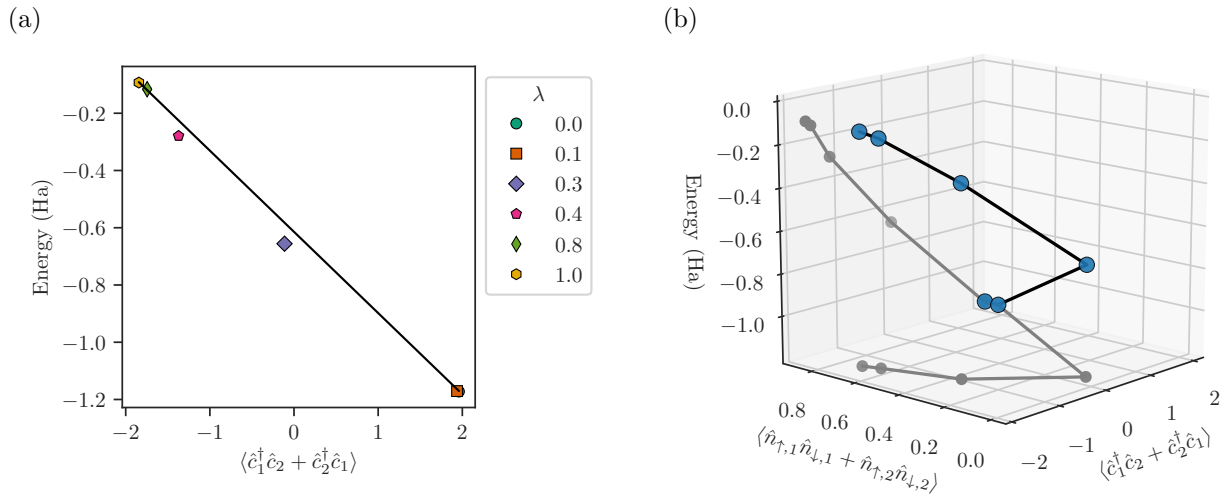

Figure 9.2: States sampled by the constrained VMC algorithm by adjusting the hopping amplitude in H_2. Each point represents a VMC calculation with different λ specified by the color and marker. (a) By increasing λ, the VMC optimization shifts from the bonding (lower right) to antibonding (upper left) state. The t parameter of a tight-binding model, (9.4) with $U = 0$, is equal to the slope of the line. The state begins to shift when $\lambda \approx t = -0.296$ Ha, as this is the energy scale of changing the hopping amplitude. The R^2 of the fit is 0.996, signifying that the tight-binding model is a good fit for this system. (b) The same data, but plotted with respect to both descriptors of the Hubbard model. The projection on the back (matching (a)) and bottom planes are shown in grey. Although the plane traces a path in three dimensions, the plot is very linear with $\langle \hat{c}_1^\dagger \hat{c}_2 + \hat{c}_2^\dagger \hat{c}_1 \rangle$, meaning that a t-only model is sufficient for this system. The state in the middle of the curve nearly minimizes the expected double occupation on the sites.

to above 0.999, signifying that it describes the states well.

The parameters, goodness-of-fit, and eigenvalues of this system appear in Tab. 9.1 as well. As expected, the tight-binding model does a relatively poor job of replicating the excited states from FCI, indicating the importance of explicitly accounting for interactions in the stretched system. The goodness-of-fit, $R^2 = 0.864$, is a direct measure of the performance of the tight-binding model, which can be interpreted as capturing 86.4% of the energy variation correctly. The performance of the Hubbard model is comparatively better than the equilibrium case, which is because the energy scale of higher-shell orbitals has risen relative to the states in bonding, antibonding, and correlated states in the $1s$ manifold. The conclusion from the study confirms the intuition that the Hubbard model is a sufficient model for the first 4 eigenstates of stretched H_2.

9.3.3 Conclusions from constrained VMC study

I presented a new algorithm for discovering low-energy states for use in density-matrix downfolding which does not rely on mean-field excitations as guesses for the states of interest. The method involves a relatively simple modification of standard VMC optimization which biases the wave function towards changing the

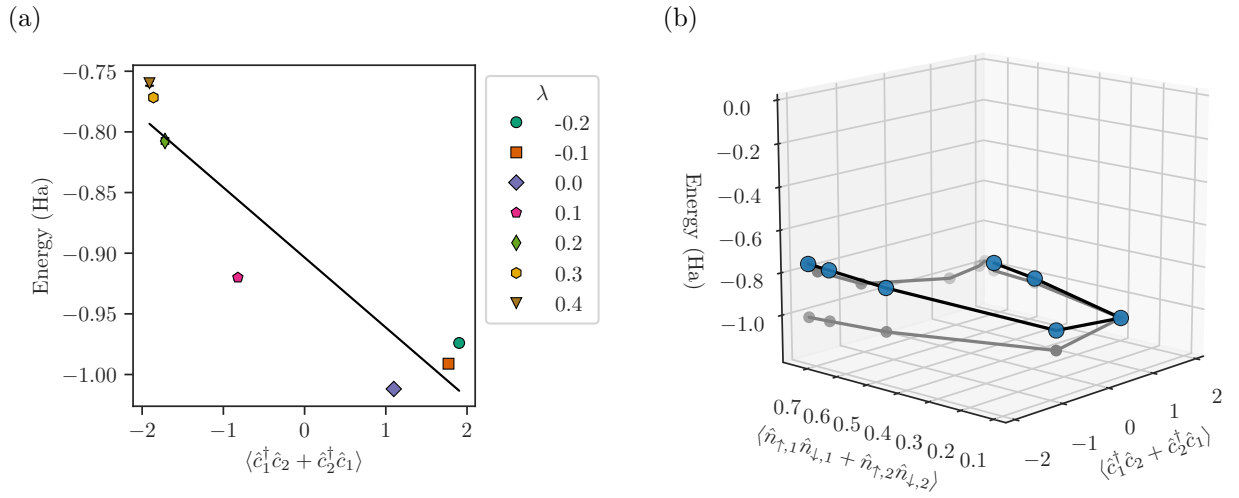

Figure 9.3: Similar to Fig 9.2, states sampled by the constrained VMC algorithm by adjusting the hopping amplitude in stretched H_2. Each point represents a VMC calculation with different λ specified by the color and marker. (a) By increasing λ, the VMC optimization shifts from the ground to antibonding (upper left) state. Because the ground state is no longer the bonding state, decreasing λ moves the state from ground to bonding. The tight-binding fit (the solid line) is no longer a good model for the system, although with $R^2 = 0.864$, it captures most of the energy variation. The error of the fit is proportional to the double-occupation of the state that is sampled, which is why the error has positive curvature. (b) The same data, but plotted with respect to both descriptors of the Hubbard model. The projection on the back (matching (a)) and bottom planes are shown in grey. The energy scale is set to the same as Fig. 9.2 to emphasize the rapid decrease of t—the slope of the line in the $\langle \hat{c}_1^\dagger \hat{c}_2 + \hat{c}_2^\dagger \hat{c}_1 \rangle$ direction, which decreases exponentially with H–H distance. The Hubbard model fits these points with $R^2 \approx 0.999$, so the points all lie in a plane with slopes of non-negligible magnitude in two directions.

descriptors of the wave function while remaining optimized in other regards. The method was able to reproduce eigenstates from FCI in the equilibrium and stretched H_2 molecule, while quantifying the importance of accounting for interactions in the effective model.

The objective function in (9.2) is not the only reasonable choice. For example, another possibility is

$$O(\mathbf{P}) = \langle \hat{H} \rangle + \lambda \left(\frac{\langle \Psi_{\mathrm{T}}(\mathbf{P}) | \hat{d} | \Psi_{\mathrm{T}}(\mathbf{P}) \rangle}{\langle \Psi_{\mathrm{T}}(\mathbf{P}) | \Psi_{\mathrm{T}}(\mathbf{P}) \rangle} - d^* \right)^2 , \tag{9.5}$$

where λ and d^* are two control parameters which control the forcefulness of the bias and the target descriptor value, respectively. By specifying d^*, the algorithm can target specific values of the descriptor.

The methods used to fit the model are applicable to much larger systems than it is possible to solve using FCI, and so represent a promising route to achieving accurate excited state on large systems. The method should allow more accurate and efficient sampling of systems like FeSe, where the low-energy excitations of the system are unclear, and mean-field estimates of the excited states nodes are inaccurate.

Chapter 10

Progress towards a first-principles understanding of correlated electron materials

Accurate and predictive first-principles methods would be an invaluable tool in both materials design and the theory of correlated electron systems. However, systems containing transition metals and other atoms with localized electrons are difficult to treat with most methods. Fixed-node DMC (FN-DMC) represents a promising tool for both these tasks, but the properties available from the method need to be extended and more systematically benchmarked. My Ph.D. work has accomplished two tasks: I have extended the benchmarks of FN-DMC and density-matrix downfolding in available in the literature, and established new strategies for leveraging FN-DMC to better understand correlated electron materials.

Three of the studies contributed to the benchmarks available in the literature. In the benchmark of barrier heights using QMC, we established that FN-DMC can provide accurate estimates of reaction barriers, a critical parameter in the prediction of chemical reaction rates. The calculations compared favorably against experiments, reaching "chemical accuracy," the accuracy required to predict room-temperature chemistry. By applying FN-DMC to a large benchmark, we analyzed trends in the fixed-node error across the sample of molecules we computed, finding that the accuracy of the trial function had little to do with the accuracy of the nodes for FN-DMC. The calculations using quantum Monte Carlo on FeSe found that FN-DMC provided better estimates of structural properties than DFT with no adjustable parameters or undetermined approximations. By comparing to fully optimized orbital calculations, we showed that energy differences in this unconventional superconductor did not change appreciably between fully optimized orbitals and orbitals generated by optimizing the hybrid exchange in DFT calculations. In $MgTi_2O_4$, we found that FN-DMC predicts a larger singlet-triplet gap than current experiments have searched for, providing an explanation for its absence in currently available experimental data. Our calculations of $MgTi_2O_4$ also provide a valuable example of a FN-DMC prediction for an excitation energy published in advance of experiment—an important test to establish a method's predictive capabilities.

These studies also establish strategies for leveraging accurate calculations like FN-DMC to characterize and explain material properties. In FeSe, we utilize FN-DMC to study how local spin texture couples to structural and electronic properties. We found a strong coupling between the energetics of these spin textures

and the structure under pressure, such that several of them become extremely close in energy as pressure rises. The orbital makeup and other electronic properties in the systems are also coupled to these spin textures, bridging structural, electronic, and magnetic properties in the system. The origin of the observations of this coupling could be explained by a simple model assuming large Hund's coupling. To verify the importance of Hund's coupling we performed a downfolding calculation on an Fe-Se diatomic molecule, applied data science techniques to analyze the results, and found that Hund's coupling was the most important predictor of properties in the system. To enable efficient and systematic downfolding calculations in future work, we developed and applied a new method of discovering low-energy states for density-matrix downfolding. This approach, combined with FN-DMC and density-matrix downfolding, could enable accurate first-principles QMC calculations to connect with tools like lattice-model calculations using DMFT and DMRG. Lattice models, in turn, may be solved for excited states and time-dependent properties across larger length scales.

I envision the future of first-principles methods, coarse-grained models, and data science becoming more interdependent, and strengthening one another in the process. Larger computers coupled with efficient and accurate methods can provide large data sets to be analyzed with tools from downfolding and machine learning. Insights from this analysis can be applied towards finding accurate and insightful coarse-grained models. Coarse-grained models can be solved more precisely over larger length-scales, and compute properties more relevant for experiments. The results of this comparison can inform on the accuracy of the first-principles calculations and downfolding process. My Ph.D. work has primarily focused on strengthening the first two steps of this process: accurate first-principles calculations and better modeling strategies. There are many avenues yet to explore, but these results show promise that an approach which unifies these different fields can advance theory of materials to a more predictive level.

Chapter 11

References

[1] Yan Zhao, Nria Gonzlez-Garca, and Donald G. Truhlar. Benchmark Database of Barrier Heights for Heavy Atom Transfer, Nucleophilic Substitution, Association, and Unimolecular Reactions and Its Use to Test Theoretical Methods. *The Journal of Physical Chemistry A*, 109(9):2012–2018, March 2005.

[2] Roberto Peverati and Donald G. Truhlar. Quest for a universal density functional: the accuracy of density functionals across a broad spectrum of databases in chemistry and physics. *Philosophical Transactions of the Royal Society of London A: Mathematical, Physical and Engineering Sciences*, 372(2011):20120476, March 2014.

[3] Paolo Giannozzi, Stefano Baroni, Nicola Bonini, Matteo Calandra, Roberto Car, Carlo Cavazzoni, Davide Ceresoli, Guido L. Chiarotti, Matteo Cococcioni, Ismaila Dabo, Andrea Dal Corso, Stefano de Gironcoli, Stefano Fabris, Guido Fratesi, Ralph Gebauer, Uwe Gerstmann, Christos Gougoussis, Anton Kokalj, Michele Lazzeri, Layla Martin-Samos, Nicola Marzari, Francesco Mauri, Riccardo Mazzarello, Stefano Paolini, Alfredo Pasquarello, Lorenzo Paulatto, Carlo Sbraccia, Sandro Scandolo, Gabriele Sclauzero, Ari P. Seitsonen, Alexander Smogunov, Paolo Umari, and Renata M. Wentzcovitch. QUANTUM ESPRESSO: a modular and open-source software project for quantum simulations of materials. *Journal of Physics: Condensed Matter*, 21(39):395502, September 2009.

[4] Richard M. Martin, Lucia Reining, and David M. Ceperley. RPA and beyond: the BetheSalpeter equation. In *Interacting Electrons*, pages 345–387. Cambridge University Press, 1 edition, 2016.

[5] S. Margadonna, Y. Takabayashi, Y. Ohishi, Y. Mizuguchi, Y. Takano, T. Kagayama, T. Nakagawa, M. Takata, and K. Prassides. Pressure evolution of the low-temperature crystal structure and bonding of the superconductor FeSe $({T}_{c}=37\text{ }\text{K})$. *Physical Review B*, 80(6):064506, August 2009.

[6] Ravhi S. Kumar, Yi Zhang, Stanislav Sinogeikin, Yuming Xiao, Sathish Kumar, Paul Chow, Andrew L. Cornelius, and Changfeng Chen. Crystal and Electronic Structure of FeSe at High Pressure and Low Temperature. *The Journal of Physical Chemistry B*, 114(39):12597–12606, October 2010.

[7] Jasmine N. Millican, Daniel Phelan, Evan L. Thomas, Juscelino B. Leo, and Elisabeth Carpenter. Pressure-induced effects on the structure of the FeSe superconductor. *Solid State Communications*, 149(1718):707–710, May 2009.

[8] Wei Wu. Modelling the electronic structure and magnetic properties of LiFeAs and FeSe using hybrid-exchange density functional theory. *Solid State Communications*, 161:23–28, May 2013.

[9] Rudolf de Bruyn Ouboter. Heike Kamerlingh Onness Discovery of Superconductivity. *Scientific American*, pages 98–103, March 1997.

[10] J. Bardeen, L. N. Cooper, and J. R. Schrieffer. Theory of Superconductivity. *Physical Review*, 108(5):1175–1204, December 1957.

[11] Igor I. Mazin. Superconductivity gets an iron boost. *Nature*, 464(7286):183–186, March 2010.

[12] K. Conder. A second life of the Matthias's rules. *Superconductor Science and Technology*, 29(8):080502, June 2016.

[13] J. G. Bednorz and K. A. Mller. Possible highTc superconductivity in the Ba-La-Cu-O system. *Zeitschrift fr Physik B Condensed Matter*, 64(2):189–193, June 1986.

[14] Yoichi Kamihara, Hidenori Hiramatsu, Masahiro Hirano, Ryuto Kawamura, Hiroshi Yanagi, Toshio Kamiya, and Hideo Hosono. Iron-Based Layered Superconductor: LaOFeP. *Journal of the American Chemical Society*, 128(31):10012–10013, August 2006.

[15] Yoichi Kamihara, Takumi Watanabe, Masahiro Hirano, and Hideo Hosono. Iron-Based Layered Superconductor La[O1-xFx]FeAs (x = 0.05-0.12) with Tc = 26 K. *Journal of the American Chemical Society*, 130(11):3296–3297, March 2008.

[16] Warren Pickett and Mikhail Eremets. The quest for room-temperature superconductivity in hydrides. *Physics Today*, 72(5):52–58, May 2019.

[17] Richard M. Martin. Theoretical Background. In *Electronic Structure*, pages 52–71. Cambridge University Press, 2004.

[18] Richard M. Martin. Relativistic Dirac equation and spin-orbit interactions. In *Electronic Structure*, pages 193–195. Cambridge University Press, 2004.

[19] A. P. Drozdov, M. I. Eremets, I. A. Troyan, V. Ksenofontov, and S. I. Shylin. Conventional superconductivity at 203 kelvin at high pressures in the sulfur hydride system. *Nature*, 525(7567):73–76, September 2015.

[20] Ion Errea, Matteo Calandra, Chris J. Pickard, Joseph Nelson, Richard J. Needs, Yinwei Li, Hanyu Liu, Yunwei Zhang, Yanming Ma, and Francesco Mauri. High-Pressure Hydrogen Sulfide from First Principles: A Strongly Anharmonic Phonon-Mediated Superconductor. *Physical Review Letters*, 114(15):157004, April 2015.

[21] Lucas K. Wagner and Jeffrey C. Grossman. Microscopic Description of Light Induced Defects in Amorphous Silicon Solar Cells. *Physical Review Letters*, 101(26):265501, December 2008.

[22] Ji-Hui Yang, Wan-Jian Yin, Ji-Sang Park, Jie Ma, and Su-Huai Wei. Review on first-principles study of defect properties of CdTe as a solar cell absorber. *Semiconductor Science and Technology*, 31(8):083002, July 2016.

[23] Joseph W. Bennett, Kevin F. Garrity, Karin M. Rabe, and David Vanderbilt. Hexagonal ABC Semiconductors as Ferroelectrics. *Physical Review Letters*, 109(16):167602, October 2012.

[24] L. R. Jr Lawrence, C. Cox, and D. Broman. High temperature superconductivity: The products and their benefits. Technical Report ORNL/Sub-97-SX339V/2, Oak Ridge National Lab., TN (United States), July 1998.

[25] Pascal Tixador. Superconducting Magnetic Energy Storage: Status and Perspective. *IEEE/CSC & ESAS European Superconductivity News Forum*, 3, 2008.

[26] J. L. He, D. M. Rote, and H. T. Coffey. Study of Japanese electrodynamic-suspension maglev systems. Technical Report ANL/ESD-20, Argonne National Lab., IL (United States). Energy Systems Div., April 1994.

[27] K. Tobita, S. Nishio, M. Enoeda, M. Sato, T. Isono, S. Sakurai, H. Nakamura, S. Sato, S. Suzuki, M. Ando, K. Ezato, T. Hayashi, T. Hayashi, T. Hirose, T. Inoue, Y. Kawamura, N. Koizumi, Y. Kudo, R. Kurihara, T. Kuroda, M. Matsukawa, K. Mouri, Y. Nakamura, M. Nishi, Y. Nomoto, J. Ohmori, N. Oyama, K. Sakamoto, T. Suzuki, M. Takechi, H. Tanigawa, K. Tsuchiya, and D. Tsuru. Design study of fusion DEMO plant at JAERI. *Fusion Engineering and Design*, 81(8):1151–1158, February 2006.

[28] D. Drung, C. Abmann, J. Beyer, A. Kirste, M. Peters, F. Ruede, and T. Schurig. Highly Sensitive and Easy-to-Use SQUID Sensors. *IEEE Transactions on Applied Superconductivity*, 17(2):699–704, June 2007.

[29] A. P. Ramirez. Colossal magnetoresistance. *Journal of Physics: Condensed Matter*, 9(39):8171–8199, September 1997.

[30] Lucile Savary and Leon Balents. Quantum spin liquids: a review. *Reports on Progress in Physics*, 80(1):016502, November 2016.

[31] P. Drude. Zur Elektronentheorie der Metalle. *Annalen der Physik*, 306(3):566–613, 1900.

[32] H. J. Schulz. Fermi liquids and non–Fermi liquids. *arXiv:cond-mat/9503150*, March 1995. arXiv: cond-mat/9503150.

[33] Richard M. Martin. Overview. In *Electronic Structure*, pages 11–51. Cambridge University Press, 2004.

[34] Sadamichi Maekawa. *Physics Of Transition Metal Oxides*. Springer, August 2004.

[35] Daniel I. Khomskii. *Transition Metal Compounds*. Cambridge University Press, 2014.

[36] Tom Timusk and Bryan Statt. The pseudogap in high-temperature superconductors: an experimental survey. *Reports on Progress in Physics*, 62(1):61–122, January 1999.

[37] M. Mitrano, A. A. Husain, S. Vig, A. Kogar, M. S. Rak, S. I. Rubeck, J. Schmalian, B. Uchoa, J. Schneeloch, R. Zhong, G. D. Gu, and P. Abbamonte. Anomalous density fluctuations in a strange metal. *Proceedings of the National Academy of Sciences*, 115(21):5392–5396, May 2018.

[38] C. A. Balseiro, M. Avignon, A. G. Rojo, and B. Alascio. Electronic properties of high-${T}_{c}$ superconductors. *Physical Review Letters*, 62(22):2624–2627, May 1989.

[39] M. Yi, Z.-K. Liu, Y. Zhang, R. Yu, J.-X. Zhu, J. J. Lee, R. G. Moore, F. T. Schmitt, W. Li, S. C. Riggs, J.-H. Chu, B. Lv, J. Hu, M. Hashimoto, S.-K. Mo, Z. Hussain, Z. Q. Mao, C. W. Chu, I. R. Fisher, Q. Si, Z.-X. Shen, and D. H. Lu. Observation of universal strong orbital-dependent correlation effects in iron chalcogenides. *Nature Communications*, 6:7777, July 2015.

[40] T. Shimojima, Y. Suzuki, T. Sonobe, A. Nakamura, M. Sakano, J. Omachi, K. Yoshioka, M. Kuwata-Gonokami, K. Ono, H. Kumigashira, A. E. Bhmer, F. Hardy, T. Wolf, C. Meingast, H. v. Lhneysen, H. Ikeda, and K. Ishizaka. Lifting of xz/yz orbital degeneracy at the structural transition in detwinned FeSe. *Physical Review B*, 90(12):121111, September 2014.

[41] Huihuo Zheng and Lucas K. Wagner. Computation of the Correlated Metal-Insulator Transition in Vanadium Dioxide from First Principles. *Physical Review Letters*, 114(17):176401, April 2015.

[42] Hitesh J. Changlani, Huihuo Zheng, and Lucas K. Wagner. Density-matrix based determination of low-energy model Hamiltonians from ab initio wavefunctions. *The Journal of Chemical Physics*, 143(10):102814, September 2015.

[43] qwalk.github.io/mainline.

[44] Brian Busemeyer. github.com/bbusemeyer/autogenv2, April 2019. original-date: 2017-08-23T21:39:13Z.

[45] Brian Busemeyer. github.com/bbusemeyer/qwalk_objects, May 2019. original-date: 2018-11-01T18:31:27Z.

[46] J. N. B. Rodrigues and Lucas K. Wagner. Spin-orbital coupling predicts whether a material class will exhibit unconventional superconductivity with low error rate. *arXiv:1810.03014 [cond-mat]*, October 2018. arXiv: 1810.03014.

[47] Dirac Paul Adrien Maurice and Fowler Ralph Howard. On the theory of quantum mechanics. *Proceedings of the Royal Society of London. Series A, Containing Papers of a Mathematical and Physical Character*, 112(762):661–677, October 1926.

[48] J. C. Slater. The Theory of Complex Spectra. *Physical Review*, 34(10):1293–1322, November 1929.

[49] T Koopmans. ber die Zuordnung von Wellenfunktionen und Eigenwerten zu den Einzelnen Elektronen Eines Atoms. *Physica*, 1(1):104–113, January 1934.

[50] Richard M. Martin. Koopman's theorem. In *Electronic Structure*, pages 64–65. Cambridge University Press, 2004.

[51] L. Dagens and F. Perrot. Hartree-Fock Band Structure and Optical Gap in Solid Neon and Argon. *Physical Review B*, 5(2):641–648, January 1972.

[52] Tomomi Shimazaki and Yoshihiro Asai. Energy band structure calculations based on screened HartreeFock exchange method: Si, AlP, AlAs, GaP, and GaAs. *The Journal of Chemical Physics*, 132(22):224105, June 2010.

[53] Attila Szabo and Neil S. Ostlund. *Modern Quantum Chemistry: Introduction to Advanced Electronic Structure Theory*. Dover Publications, New York, UNITED STATES, 1996.

[54] B. Huron, J. P. Malrieu, and P. Rancurel. Iterative perturbation calculations of ground and excited state energies from multiconfigurational zerothorder wavefunctions. *The Journal of Chemical Physics*, 58(12):5745–5759, June 1973.

[55] Olaf Hbner and Joachim Sauer. The electronic states of Fe2s2-/0/+/2+. *The Journal of Chemical Physics*, 116(2):617–628, December 2001.

[56] Daniel K. W. Mok, Ralf Neumann, and Nicholas C. Handy. Dynamical and Nondynamical Correlation. *The Journal of Physical Chemistry*, 100(15):6225–6230, January 1996.

[57] Sandeep Sharma, Kantharuban Sivalingam, Frank Neese, and Garnet Kin-Lic Chan. Low-energy spectrum of ironsulfur clusters directly from many-particle quantum mechanics. *Nature Chemistry*, 6(10):927–933, October 2014.

[58] Adam A. Holmes, Norm M. Tubman, and C. J. Umrigar. Heat-Bath Configuration Interaction: An Efficient Selected Configuration Interaction Algorithm Inspired by Heat-Bath Sampling. *Journal of Chemical Theory and Computation*, 12(8):3674–3680, August 2016.

[59] Tosio Kato. On the eigenfunctions of many-particle systems in quantum mechanics. *Communications on Pure and Applied Mathematics*, 10(2):151–177, 1957.

[60] R. N. Euwema, D. L. Wilhite, and G. T. Surratt. General Crystalline Hartree-Fock Formalism: Diamond Results. *Physical Review B*, 7(2):818–831, January 1973.

[61] G. G. Wepfer, R. N. Euwema, G. T. Surratt, and D. L. Wilhite. Hartree-Fock directional Compton profiles for diamond. *Physical Review B*, 9(6):2670–2673, March 1974.

[62] F. Gygi and A. Baldereschi. Self-consistent Hartree-Fock and screened-exchange calculations in solids: Application to silicon. *Physical Review B*, 34(6):4405–4408, September 1986.

[63] Tom Ziegler and Arvi Rauk. On the calculation of bonding energies by the Hartree Fock Slater method. *Theoretica chimica acta*, 46(1):1–10, March 1977.

[64] George H. Booth, Andreas Grneis, Georg Kresse, and Ali Alavi. Towards an exact description of electronic wavefunctions in real solids. *Nature*, 493(7432):365–370, January 2013.

[65] W. M. C. Foulkes, L. Mitas, R. J. Needs, and G. Rajagopal. Quantum Monte Carlo simulations of solids. *Reviews of Modern Physics*, 73(1):33–83, January 2001.

[66] R J Bartlett. Many-Body Perturbation Theory and Coupled Cluster Theory for Electron Correlation in Molecules. *Annual Review of Physical Chemistry*, 32(1):359–401, October 1981.

[67] Rodney J. Bartlett and Monika Musia. Coupled-cluster theory in quantum chemistry. *Reviews of Modern Physics*, 79(1):291–352, February 2007.

[68] Shiwei Zhang. Ab Initio Electronic Structure Calculations by Auxiliary-Field Quantum Monte Carlo. In Wanda Andreoni and Sidney Yip, editors, *Handbook of Materials Modeling : Methods: Theory and Modeling*, pages 1–27. Springer International Publishing, Cham, 2018.

[69] So Hirata, Rafa Podeszwa, Motoi Tobita, and Rodney J. Bartlett. Coupled-cluster singles and doubles for extended systems. *The Journal of Chemical Physics*, 120(6):2581–2592, February 2004.

[70] James McClain, Qiming Sun, Garnet Kin-Lic Chan, and Timothy C. Berkelbach. Gaussian-Based Coupled-Cluster Theory for the Ground-State and Band Structure of Solids. *Journal of Chemical Theory and Computation*, 13(3):1209–1218, March 2017.

[71] Thomas Gruber, Ke Liao, Theodoros Tsatsoulis, Felix Hummel, and Andreas Grneis. Applying the Coupled-Cluster Ansatz to Solids and Surfaces in the Thermodynamic Limit. *Physical Review X*, 8(2):021043, May 2018.

[72] Yanbin Wu, Lucas K. Wagner, and Narayana R. Aluru. Hexagonal boron nitride and water interaction parameters. *The Journal of Chemical Physics*, 144(16):164118, April 2016.

[73] Xuefei Xu, Wenjing Zhang, Mingsheng Tang, and Donald G. Truhlar. Do Practical Standard Coupled Cluster Calculations Agree Better than KohnSham Calculations with Currently Available Functionals When Compared to the Best Available Experimental Data for Dissociation Energies of Bonds to 3d Transition Metals? *Journal of Chemical Theory and Computation*, 11(5):2036–2052, May 2015.

[74] Lan Cheng, Jrgen Gauss, Branko Ruscic, Peter B. Armentrout, and John F. Stanton. Bond Dissociation Energies for Diatomic Molecules Containing 3d Transition Metals: Benchmark Scalar-Relativistic Coupled-Cluster Calculations for 20 Molecules. *Journal of Chemical Theory and Computation*, 13(3):1044–1056, March 2017.

[75] Kristine Pierloot, Quan Manh Phung, and Alex Domingo. Spin State Energetics in First-Row Transition Metal Complexes: Contribution of (3s3p) Correlation and Its Description by Second-Order Perturbation Theory. *Journal of Chemical Theory and Computation*, 13(2):537–553, February 2017.

[76] Garnet Kin-Lic Chan and Sandeep Sharma. The Density Matrix Renormalization Group in Quantum Chemistry. *Annual Review of Physical Chemistry*, 62(1):465–481, March 2011.

[77] Ulrich Schollwock. The density-matrix renormalization group in the age of matrix product states. *Annals of Physics*, 326(1):96–192, January 2011.

[78] Roman Orus. A practical introduction to tensor networks: Matrix product states and projected entangled pair states. *Annals of Physics*, 349:117–158, October 2014.

[79] Garnet Kin-Lic Chan and Martin Head-Gordon. Highly correlated calculations with a polynomial cost algorithm: A study of the density matrix renormalization group. *The Journal of Chemical Physics*, 116(11):4462–4476, March 2002.

[80] Garnet Kin-Lic Chan. An algorithm for large scale density matrix renormalization group calculations. *The Journal of Chemical Physics*, 120(7):3172–3178, February 2004.

[81] Yuki Kurashige and Takeshi Yanai. High-performance ab initio density matrix renormalization group method: Applicability to large-scale multireference problems for metal compounds. *The Journal of Chemical Physics*, 130(23):234114, June 2009.

[82] Johannes Hachmann, Jonathan J. Dorando, Michael Avils, and Garnet Kin-Lic Chan. The radical character of the acenes: A density matrix renormalization group study. *The Journal of Chemical Physics*, 127(13):134309, October 2007.

[83] Simons Collaboration on the Many-Electron Problem, Mario Motta, David M. Ceperley, Garnet Kin-Lic Chan, John A. Gomez, Emanuel Gull, Sheng Guo, Carlos A. Jimnez-Hoyos, Tran Nguyen Lan, Jia Li, Fengjie Ma, Andrew J. Millis, Nikolay V. Prokofev, Ushnish Ray, Gustavo E. Scuseria, Sandro Sorella, Edwin M. Stoudenmire, Qiming Sun, Igor S. Tupitsyn, Steven R. White, Dominika Zgid, and Shiwei Zhang. Towards the Solution of the Many-Electron Problem in Real Materials: Equation of State of the Hydrogen Chain with State-of-the-Art Many-Body Methods. *Physical Review X*, 7(3):031059, September 2017.

[84] Bo-Xiao Zheng, Chia-Min Chung, Philippe Corboz, Georg Ehlers, Ming-Pu Qin, Reinhard M. Noack, Hao Shi, Steven R. White, Shiwei Zhang, and Garnet Kin-Lic Chan. Stripe order in the underdoped region of the two-dimensional Hubbard model. *Science*, 358(6367):1155–1160, December 2017.

[85] C. J. Umrigar, Julien Toulouse, Claudia Filippi, S. Sorella, and R. G. Hennig. Alleviation of the Fermion-Sign Problem by Optimization of Many-Body Wave Functions. *Physical Review Letters*, 98(11):110201, March 2007.

[86] Julien Toulouse and C. J. Umrigar. Optimization of quantum Monte Carlo wave functions by energy minimization. *The Journal of Chemical Physics*, 126(8):084102, February 2007.

[87] C. J. Umrigar, K. G. Wilson, and J. W. Wilkins. Optimized trial wave functions for quantum Monte Carlo calculations. *Physical Review Letters*, 60(17):1719–1722, April 1988.

[88] Nicholas Metropolis, Arianna W. Rosenbluth, Marshall N. Rosenbluth, Augusta H. Teller, and Edward Teller. Equation of State Calculations by Fast Computing Machines. *The Journal of Chemical Physics*, 21(6):1087–1092, June 1953.

[89] Lucas K. Wagner and David M. Ceperley. Discovering correlated fermions using quantum Monte Carlo. *Reports on Progress in Physics*, 79(9):094501, 2016.

[90] Lucas K. Wagner, Michal Bajdich, and Lubos Mitas. QWalk: A quantum Monte Carlo program for electronic structure. *Journal of Computational Physics*, 228(9):3390–3404, May 2009.

[91] Lucas K. Wagner. Types of single particle symmetry breaking in transition metal oxides due to electron correlation. *The Journal of Chemical Physics*, 138(9):094106, March 2013.

[92] N. S. Blunt and Eric Neuscamman. Charge-transfer excited states: Seeking a balanced and efficient wave function ansatz in variational Monte Carlo. *The Journal of Chemical Physics*, 147(19):194101, November 2017.

[93] Luning Zhao and Eric Neuscamman. An Efficient Variational Principle for the Direct Optimization of Excited States. *Journal of Chemical Theory and Computation*, 12(8):3436–3440, August 2016.

[94] M. Bajdich, L. Mitas, L.K. Wagner, and K.E. Schmidt. Pfaffian pairing and backflow wavefunctions for electronic structure quantum Monte Carlo methods. *Physical Review B - Condensed Matter and Materials Physics*, 77(11), 2008.

[95] Andrea Zen, Ye Luo, Guglielmo Mazzola, Leonardo Guidoni, and Sandro Sorella. Ab initio molecular dynamics simulation of liquid water by quantum Monte Carlo. *The Journal of Chemical Physics*, 142(14):144111, April 2015.

[96] Luning Zhao and Eric Neuscamman. A Blocked Linear Method for Optimizing Large Parameter Sets in Variational Monte Carlo. *Journal of Chemical Theory and Computation*, 13(6):2604–2611, June 2017.

[97] Giuseppe Carleo and Matthias Troyer. Solving the quantum many-body problem with artificial neural networks. *Science*, 355(6325):602–606, February 2017.

[98] Di Luo and Bryan K. Clark. Backflow Transformations via Neural Networks for Quantum Many-Body Wave Functions. *Physical Review Letters*, 122(22):226401, June 2019.

[99] Julien Toulouse, Roland Assaraf, and C. J. Umrigar. Introduction to the variational and diffusion Monte Carlo methods. *arXiv:1508.02989 [physics]*, August 2015. arXiv: 1508.02989.

[100] Richard M. Martin, Lucia Reining, and David M. Ceperley. Projector quantum Monte Carlo. In *Interacting Electrons*, pages 609–642. Cambridge University Press, 1 edition, 2016.

[101] H. F. Trotter. On the product of semi-groups of operators. *Proceedings of the American Mathematical Society*, 10(4):545–551, 1959.

[102] Peter J. Reynolds, David M. Ceperley, Berni J. Alder, and William A. Lester. Fixednode quantum Monte Carlo for moleculesa)b). *The Journal of Chemical Physics*, 77(11):5593–5603, December 1982.

[103] Friedemann Schautz, Francesco Buda, and Claudia Filippi. Excitations in photoactive molecules from quantum Monte Carlo. *The Journal of Chemical Physics*, 121(12):5836–5844, September 2004.

[104] R. J. Hunt, M. Szyniszewski, G. I. Prayogo, R. Maezono, and N. D. Drummond. Quantum Monte Carlo calculations of energy gaps from first principles. *Physical Review B*, 98(7):075122, August 2018.

[105] Chun-Gang Duan, R. F. Sabiryanov, W. N. Mei, P. A. Dowben, S. S. Jaswal, and E. Y. Tsymbal. Magnetic ordering in Gd monopnictides: Indirect exchange versus superexchange interaction. *Applied Physics Letters*, 88(18):182505, May 2006.

[106] Hirofumi Akamatsu, Yu Kumagai, Fumiyasu Oba, Koji Fujita, Hideo Murakami, Katsuhisa Tanaka, and Isao Tanaka. Antiferromagnetic superexchange via $3d$ states of titanium in EuTiO${}_{3}$ as seen from hybrid Hartree-Fock density functional calculations. *Physical Review B*, 83(21):214421, June 2011.

[107] Kateryna Foyevtsova, Jaron T. Krogel, Jeongnim Kim, P. R. C. Kent, Elbio Dagotto, and Fernando A. Reboredo. Ab initio Quantum Monte Carlo Calculations of Spin Superexchange in Cuprates: The Benchmarking Case of ${\mathrm{Ca}}_{2}{\mathrm{CuO}}_{3}$. *Physical Review X*, 4(3):031003, July 2014.

[108] David M. Ceperley. Monte Carlo Methods in Statistical Physics. In Kurt Binder, editor, *Monte Carlo Methods in Statistical Physics*, Topics in Current Physics, pages 145–194. Springer-Verlag, Berlin Heidelberg, 2 edition, 1986.

[109] Richard M. Martin, Lucia Reining, and David M. Ceperley. Ground state path integrals (GSPI). In *Interacting Electrons*, pages 609–642. Cambridge University Press, 1 edition, 2016.

[110] M. D. Brown, J. R. Trail, P. Lpez Ros, and R. J. Needs. Energies of the first row atoms from quantum Monte Carlo. *The Journal of Chemical Physics*, 126(22):224110, June 2007.

[111] A. Sarsa, E. Buenda, F.J. Glvez, and P. Maldonado. Quantum Monte Carlo for 3d transition-metal atoms. *Journal of Physical Chemistry A*, 112(10):2074–2076, 2008.

[112] P. Seth, P. Lpez Ros, and R. J. Needs. Quantum Monte Carlo study of the first-row atoms and ions. *The Journal of Chemical Physics*, 134(8):084105, February 2011.

[113] E. Buenda, F.J. Glvez, P. Maldonado, and A. Sarsa. Quantum Monte Carlo ionization potential and electron affinity for transition metal atoms. *Chemical Physics Letters*, 559:12–17, 2013.

[114] Lucas K. Wagner and Lubos Mitas. Energetics and dipole moment of transition metal monoxides by quantum Monte Carlo. *The Journal of Chemical Physics*, 126(3):034105, January 2007.

[115] Matus Dubecky, Petr Jureka, Ren Derian, Pavel Hobza, Michal Otyepka, and Lubos Mitas. Quantum Monte Carlo Methods Describe Noncovalent Interactions with Subchemical Accuracy. *Journal of Chemical Theory and Computation*, 9(10):4287–4292, October 2013.

[116] A. Zen, Y. Luo, S. Sorella, and L. Guidoni. Molecular properties by quantum Monte Carlo: An investigation on the role of the wave function ansatz and the basis set in the water molecule. *Journal of Chemical Theory and Computation*, 9(10):4332–4350, 2013.

[117] M. Dubecky, R. Derian, P. Jurecka, L. Mitas, P. Hobza, and M. Otyepka. Quantum Monte Carlo for noncovalent interactions: An efficient protocol attaining benchmark accuracy. *Physical Chemistry Chemical Physics*, 16(38):20915–20923, 2014.

[118] Yubo Yang, Ilkka Kylnp, Norm M. Tubman, Jaron T. Krogel, Sharon Hammes-Schiffer, and David M. Ceperley. How large are nonadiabatic effects in atomic and diatomic systems? *The Journal of Chemical Physics*, 143(12):124308, September 2015.

[119] Jeffrey C. Grossman. Benchmark quantum Monte Carlo calculations. *The Journal of Chemical Physics*, 117(4):1434–1440, July 2002.

[120] N. Nemec, M.D. Towler, and R.J. Needs. Benchmark all-electron ab initio quantum Monte Carlo calculations for small molecules. *Journal of Chemical Physics*, 132(3), 2010.

[121] Petruzielo, F. R., Toulouse, Julien, and Umrigar, C. J. Approaching chemical accuracy with quantum Monte Carlo. *The Journal of Chemical Physics*, 136(12):124116, March 2012.

[122] Jindich Koloren and Lubos Mitas. Quantum Monte Carlo Calculations of Structural Properties of FeO Under Pressure. *Physical Review Letters*, 101(18):185502, October 2008.

[123] Lucas K. Wagner and Peter Abbamonte. Effect of electron correlation on the electronic structure and spin-lattice coupling of high-${T}_{c}$ cuprates: Quantum Monte Carlo calculations. *Physical Review B*, 90(12):125129, September 2014.

[124] Lucas K. Wagner. Ground state of doped cuprates from first-principles quantum Monte Carlo calculations. *Physical Review B*, 92(16):161116, October 2015.

[125] Huihuo Zheng and Lucas K. Wagner. Erratum: Computation of the Correlated Metal-Insulator Transition in Vanadium Dioxide from First Principles [Phys. Rev. Lett. 114, 176401 (2015)]. *Physical Review Letters*, 120(5):059901, January 2018.

[126] R. J. Needs and M. D. Towler. THE DIFFUSION QUANTUM MONTE CARLO METHOD: DESIGNING TRIAL WAVE FUNCTIONS FOR NiO. *International Journal of Modern Physics B*, 17(28):5425–5434, November 2003.

[127] Chandrima Mitra, Jaron T. Krogel, Juan A. Santana, and Fernando A. Reboredo. Many-body ab initio diffusion quantum Monte Carlo applied to the strongly correlated oxide NiO. *The Journal of Chemical Physics*, 143(16):164710, October 2015.

[128] Joshua A. Schiller, Lucas K. Wagner, and Elif Ertekin. Phase stability and properties of manganese oxide polymorphs: Assessment and insights from diffusion Monte Carlo. *Physical Review B*, 92(23):235209, December 2015.

[129] Richard M. Martin, Lucia Reining, and David M. Ceperley. Estimating real-time correlation functions. In *Interacting Electrons*, pages 665–669. Cambridge University Press, 1 edition, 2016.

[130] J. Carlson, J. E. Gubernatis, G. Ortiz, and Shiwei Zhang. Issues and observations on applications of the constrained-path Monte Carlo method to many-fermion systems. *Physical Review B*, 59(20):12788–12798, May 1999.

[131] Shiwei Zhang, J. Carlson, and J. E. Gubernatis. Constrained path Monte Carlo method for fermion ground states. *Physical Review B*, 55(12):7464–7477, March 1997.

[132] Mingpu Qin, Hao Shi, and Shiwei Zhang. Coupling quantum Monte Carlo and independent-particle calculations: Self-consistent constraint for the sign problem based on the density or the density matrix. *Physical Review B*, 94(23):235119, December 2016.

[133] Simons Collaboration on the Many-Electron Problem, J.P.F. LeBlanc, Andrey E. Antipov, Federico Becca, Ireneusz W. Bulik, Garnet Kin-Lic Chan, Chia-Min Chung, Youjin Deng, Michel Ferrero, Thomas M. Henderson, Carlos A. Jimnez-Hoyos, E. Kozik, Xuan-Wen Liu, Andrew J. Millis, N.V. Prokofev, Mingpu Qin, Gustavo E. Scuseria, Hao Shi, B.V. Svistunov, Luca F. Tocchio, I.S. Tupitsyn, Steven R. White, Shiwei Zhang, Bo-Xiao Zheng, Zhenyue Zhu, and Emanuel Gull. Solutions of the Two-Dimensional Hubbard Model: Benchmarks and Results from a Wide Range of Numerical Algorithms. *Physical Review X*, 5(4):041041, December 2015.

[134] Shiwei Zhang, J. Carlson, and J. E. Gubernatis. Pairing Correlations in the Two-Dimensional Hubbard Model. *Physical Review Letters*, 78(23):4486–4489, June 1997.

[135] Mingpu Qin, Hao Shi, and Shiwei Zhang. Benchmark study of the two-dimensional Hubbard model with auxiliary-field quantum Monte Carlo method. *Physical Review B*, 94(8):085103, August 2016.

[136] Ettore Vitali, Hao Shi, Mingpu Qin, and Shiwei Zhang. Computation of dynamical correlation functions for many-fermion systems with auxiliary-field quantum Monte Carlo. *Physical Review B*, 94(8):085140, August 2016.

[137] Fengjie Ma, Shiwei Zhang, and Henry Krakauer. Excited state calculations in solids by auxiliary-field quantum Monte Carlo. *New Journal of Physics*, 15(9):093017, September 2013.

[138] Shuai Zhang, Fionn D. Malone, and Miguel A. Morales. Auxiliary-field quantum Monte Carlo calculations of the structural properties of nickel oxide. *The Journal of Chemical Physics*, 149(16):164102, October 2018.

[139] Mario Motta and Shiwei Zhang. Ab initio computations of molecular systems by the auxiliary-field quantum Monte Carlo method. *Wiley Interdisciplinary Reviews: Computational Molecular Science*, 8(5):e1364, 2018.

[140] Richard M. Martin. Hohenberg-Kohn theorems. In *Electronic Structure*, pages 121–125. Cambridge University Press, 2004.

[141] P. Hohenberg and W. Kohn. Inhomogeneous Electron Gas. *Physical Review*, 136(3B):B864–B871, November 1964.

[142] Michael G. Medvedev, Ivan S. Bushmarinov, Jianwei Sun, John P. Perdew, and Konstantin A. Lyssenko. Density functional theory is straying from the path toward the exact functional. *Science*, 355(6320):49–52, January 2017.

[143] Richard M. Martin. the Kohn-Sham ansatz. In *Electronic Structure*, pages 135–152. Cambridge University Press, 2004.

[144] D. M. Ceperley and B. J. Alder. Ground State of the Electron Gas by a Stochastic Method. *Physical Review Letters*, 45(7):566–569, August 1980.

[145] Lei Wang, Thomas Maxisch, and Gerbrand Ceder. Oxidation energies of transition metal oxides within the $\mathrm{GGA}+\mathrm{U}$ framework. *Physical Review B*, 73(19):195107, May 2006.

[146] John P. Perdew, Kieron Burke, and Matthias Ernzerhof. Generalized Gradient Approximation Made Simple. *Physical Review Letters*, 77(18):3865–3868, October 1996.

[147] John P. Perdew, Matthias Ernzerhof, and Kieron Burke. Rationale for mixing exact exchange with density functional approximations. *The Journal of Chemical Physics*, 105(22):9982–9985, December 1996.

[148] Takao Tsuneda and Kimihiko Hirao. Self-interaction corrections in density functional theory. *The Journal of Chemical Physics*, 140(18):18A513, March 2014.

[149] Anubhav Jain, Geoffroy Hautier, Shyue Ping Ong, Charles J. Moore, Christopher C. Fischer, Kristin A. Persson, and Gerbrand Ceder. Formation enthalpies by mixing GGA and GGA $+$ U calculations. *Physical Review B*, 84(4):045115, July 2011.

[150] S. Leoni, A. N. Yaresko, N. Perkins, H. Rosner, and L. Craco. Orbital-spin order and the origin of structural distortion in ${\text{MgTi}}_{2}{\text{O}}_{4}$. *Physical Review B*, 78(12):125105, September 2008.

[151] Manh-Thuong Nguyen, Matteo Farnesi Camellone, and Ralph Gebauer. On the electronic, structural, and thermodynamic properties of Au supported on -Fe2o3 surfaces and their interaction with CO. *The Journal of Chemical Physics*, 143(3):034704, July 2015.

[152] Carlo Motta, Fedwa El-Mellouhi, Sabre Kais, Nouar Tabet, Fahhad Alharbi, and Stefano Sanvito. Revealing the role of organic cations in hybrid halide perovskite $CH_3NH_3PbI_3$. *Nature Communications*, 6:7026, April 2015.

[153] R. D. King-Smith and David Vanderbilt. Theory of polarization of crystalline solids. *Physical Review B*, 47(3):1651–1654, January 1993.

[154] Ya-ping Wang, Sheng-shi Li, Chang-wen Zhang, Shu-feng Zhang, Wei-xiao Ji, Ping Li, and Pei-ji Wang. High-temperature Dirac half-metal PdCl3: a promising candidate for realizing quantum anomalous Hall effect. *Journal of Materials Chemistry C*, 6(38):10284–10291, October 2018.

[155] Jorge Quintanilla and Chris Hooley. The strong-correlations puzzle. *Physics World*, 22(06):32–37, June 2009.

[156] A. Jain, S.P. Ong, G. Hautier, W. Chen, W.D. Richards, S. Dacek, S. Cholia, D. Gunter, D. Skinner, G. Ceder, and K.A. Persson. Commentary: The materials project: A materials genome approach to accelerating materials innovation. *APL Materials*, 1(1), 2013.

[157] S. Q. Wu, M. Ji, C. Z. Wang, M. C. Nguyen, X. Zhao, K. Umemoto, R. M. Wentzcovitch, and K. M. Ho. An adaptive genetic algorithm for crystal structure prediction. *Journal of Physics: Condensed Matter*, 26(3):035402, December 2013.

[158] F. Ercolessi and J. B. Adams. Interatomic Potentials from First-Principles Calculations: The Force-Matching Method. *EPL (Europhysics Letters)*, 26(8):583, 1994.

[159] G. Kotliar, S. Y. Savrasov, K. Haule, V. S. Oudovenko, O. Parcollet, and C. A. Marianetti. Electronic structure calculations with dynamical mean-field theory. *Reviews of Modern Physics*, 78(3):865–951, August 2006.

[160] V. Eyert. The metalinsulator transitions of VO2: A band theoretical approach. *Annalen der Physik*, 11(9):650–704, October 2002.

[161] C. Rdl, F. Fuchs, J. Furthmller, and F. Bechstedt. Quasiparticle band structures of the antiferromagnetic transition-metal oxides MnO, FeO, CoO, and NiO. *Physical Review B*, 79(23):235114, June 2009.

[162] Simon Pesant and Michel Ct. DFT + U study of magnetic order in doped La${}_{2}$CuO${}_{4}$ crystals. *Physical Review B*, 84(8):085104, August 2011.

[163] W. E. Pickett, D. J. Singh, H. Krakauer, and R. E. Cohen. Fermi Surfaces, Fermi Liquids, and High-Temperature Superconductors. *Science*, 255(5040):46–54, January 1992.

[164] Vladimir I. Anisimov, Jan Zaanen, and Ole K. Andersen. Band theory and Mott insulators: Hubbard U instead of Stoner I. *Physical Review B*, 44(3):943–954, July 1991.

[165] Alaska Subedi, Lijun Zhang, D. J. Singh, and M. H. Du. Density functional study of FeS, FeSe, and FeTe: Electronic structure, magnetism, phonons, and superconductivity. *Physical Review B*, 78(13):134514, October 2008.

[166] Richard M. Martin, Lucia Reining, and David M. Ceperley. Particles and quasi-particles. In *Interacting Electrons*, pages 144–166. Cambridge University Press, 1 edition, 2016.

[167] Richard M. Martin, Lucia Reining, and David M. Ceperley. Correlation functions. In *Interacting Electrons*, pages 84–120. Cambridge University Press, 1 edition, 2016.

[168] David Bohm and David Pines. A Collective Description of Electron Interactions. I. Magnetic Interactions. *Physical Review*, 82(5):625–634, June 1951.

[169] David Pines and David Bohm. A Collective Description of Electron Interactions: II. Collective vs Individual Particle Aspects of the Interactions. *Physical Review*, 85(2):338–353, January 1952.

[170] David Bohm and David Pines. A Collective Description of Electron Interactions: III. Coulomb Interactions in a Degenerate Electron Gas. *Physical Review*, 92(3):609–625, November 1953.

[171] M. vanSchilfgaarde, Takao Kotani, and S. Faleev. Quasiparticle Self-Consistent GW Theory. *Physical Review Letters*, 96(22):226402, June 2006.

[172] Richard M. Martin, Lucia Reining, and David M. Ceperley. The RPA and the GW approximation for the self-energy. In *Interacting Electrons*, pages 245–278. Cambridge University Press, 1 edition, 2016.

[173] Richard M. Martin, Lucia Reining, and David M. Ceperley. GWA calculations in practice. In *Interacting Electrons*, pages 280–310. Cambridge University Press, 1 edition, 2016.

[174] A. G. Marinopoulos, Lucia Reining, Valerio Olevano, Angel Rubio, T. Pichler, X. Liu, M. Knupfer, and J. Fink. Anisotropy and Interplane Interactions in the Dielectric Response of Graphite. *Physical Review Letters*, 89(7):076402, July 2002.

[175] Huihuo Zheng, Yu Gan, Peter Abbamonte, and Lucas K. Wagner. Importance of $\ensuremath{\sigma}$ Bonding Electrons for the Accurate Description of Electron Correlation in Graphene. *Physical Review Letters*, 119(16):166402, October 2017.

[176] Michael Rohlfing, Peter Krger, and Johannes Pollmann. Quasiparticle band-structure calculations for C, Si, Ge, GaAs, and SiC using Gaussian-orbital basis sets. *Physical Review B*, 48(24):17791–17805, December 1993.

[177] Y. Pavlyukh, A.-M. Uimonen, G. Stefanucci, and R. van Leeuwen. Vertex Corrections for Positive-Definite Spectral Functions of Simple Metals. *Physical Review Letters*, 117(20):206402, November 2016.

[178] Andrey L. Kutepov. Electronic structure of Na, K, Si, and LiF from self-consistent solution of Hedin's equations including vertex corrections. *Physical Review B*, 94(15):155101, October 2016.

[179] Peilin Liao and Emily A. Carter. Testing variations of the GW approximation on strongly correlated transition metal oxides: hematite (-Fe2o3) as a benchmark. *Physical Chemistry Chemical Physics*, 13(33):15189–15199, September 2011.

[180] Mark S. Hybertsen and Steven G. Louie. Electron correlation in semiconductors and insulators: Band gaps and quasiparticle energies. *Physical Review B*, 34(8):5390–5413, October 1986.

[181] Miguel M. Ugeda, Aaron J. Bradley, Su-Fei Shi, Felipe H. da Jornada, Yi Zhang, Diana Y. Qiu, Wei Ruan, Sung-Kwan Mo, Zahid Hussain, Zhi-Xun Shen, Feng Wang, Steven G. Louie, and Michael F. Crommie. Giant bandgap renormalization and excitonic effects in a monolayer transition metal dichalcogenide semiconductor. *Nature Materials*, 13(12):1091–1095, December 2014.

[182] Matteo Guzzo, Giovanna Lani, Francesco Sottile, Pina Romaniello, Matteo Gatti, Joshua J. Kas, John J. Rehr, Mathieu G. Silly, Fausto Sirotti, and Lucia Reining. Valence Electron Photoemission Spectrum of Semiconductors: Ab Initio Description of Multiple Satellites. *Physical Review Letters*, 107(16):166401, October 2011.

[183] Matteo Gatti, Fabien Bruneval, Valerio Olevano, and Lucia Reining. Understanding Correlations in Vanadium Dioxide from First Principles. *Physical Review Letters*, 99(26):266402, December 2007.

[184] Hiroyuki Abe, Masami Terauchi, Michiyoshi Tanaka, Shik Shin, and Yutaka Ueda. Electron Energy-loss Spectroscopy Study of the Metal-insulator Transition in VO 2. *Japanese Journal of Applied Physics*, 36(1R):165, January 1997.

[185] B. Holm and U. von Barth. Fully self-consistent GW self-energy of the electron gas. *Physical Review B*, 57(4):2108–2117, January 1998.

[186] M. Shishkin and G. Kresse. Self-consistent GW calculations for semiconductors and insulators. *Physical Review B*, 75(23):235102, June 2007.

[187] Stephan Lany. Band-structure calculations for the 3d transition metal oxides in GW. *Physical Review B*, 87(8):085112, February 2013.

[188] Richard M. Martin, Lucia Reining, and David M. Ceperley. Dynamical mean-field theory. In *Interacting Electrons*, pages 421–457. Cambridge University Press, 1 edition, 2016.

[189] Hyowon Park, Andrew J. Millis, and Chris A. Marianetti. Computing total energies in complex materials using charge self-consistent DFT + DMFT. *Physical Review B*, 90(23):235103, December 2014.

[190] E. A. Nowadnick, J. P. Ruf, H. Park, P. D. C. King, D. G. Schlom, K. M. Shen, and A. J. Millis. Quantifying electronic correlation strength in a complex oxide: A combined DMFT and ARPES study of ${\text{LaNiO}}_{3}$. *Physical Review B*, 92(24):245109, December 2015.

[191] A. I. Lichtenstein, M. I. Katsnelson, and G. Kotliar. Finite-Temperature Magnetism of Transition Metals: An ab initio Dynamical Mean-Field Theory. *Physical Review Letters*, 87(6):067205, July 2001.

[192] Markus Aichhorn, Leonid Pourovskii, Veronica Vildosola, Michel Ferrero, Olivier Parcollet, Takashi Miyake, Antoine Georges, and Silke Biermann. Dynamical mean-field theory within an augmented plane-wave framework: Assessing electronic correlations in the iron pnictide LaFeAsO. *Physical Review B*, 80(8):085101, August 2009.

[193] Markus Aichhorn, Silke Biermann, Takashi Miyake, Antoine Georges, and Masatoshi Imada. Theoretical evidence for strong correlations and incoherent metallic state in FeSe. *Physical Review B*, 82(6):064504, August 2010.

[194] Jan M. Tomczak, M. van Schilfgaarde, and G. Kotliar. Many-Body Effects in Iron Pnictides and Chalcogenides: Nonlocal Versus Dynamic Origin of Effective Masses. *Physical Review Letters*, 109(23):237010, December 2012.

[195] Chenglin Zhang, Leland W. Harriger, Zhiping Yin, Weicheng Lv, Miaoyin Wang, Guotai Tan, Yu Song, D.L. Abernathy, Wei Tian, Takeshi Egami, Kristjan Haule, Gabriel Kotliar, and Pengcheng Dai. Effect of Pnictogen Height on Spin Waves in Iron Pnictides. *Physical Review Letters*, 112(21):217202, May 2014.

[196] Hung T. Dang, Jernej Mravlje, Antoine Georges, and Andrew J. Millis. Electronic correlations, magnetism, and Hund's rule coupling in the ruthenium perovskites ${\text{SrRuO}}_{3}$ and ${\text{CaRuO}}_{3}$. *Physical Review B*, 91(19):195149, May 2015.

[197] Minjae Kim and B. I. Min. Nature of itinerant ferromagnetism of ${\mathrm{SrRuO}}_{3}$: A DFT+DMFT study. *Physical Review B*, 91(20):205116, May 2015.

[198] Daniel Bauernfeind, Robert Triebl, Manuel Zingl, Markus Aichhorn, and Hans Gerd Evertz. Dynamical mean-field theory on the real-frequency axis: $p\text{\ensuremath{-}}d$ hybridization and atomic physics in ${\mathrm{SrMnO}}_{3}$. *Physical Review B*, 97(11):115156, March 2018.

[199] Hong Chul Choi, B. I. Min, J. H. Shim, K. Haule, and G. Kotliar. Temperature-Dependent Fermi Surface Evolution in Heavy Fermion ${\mathrm{CeIrIn}}_{5}$. *Physical Review Letters*, 108(1):016402, January 2012.

[200] S. Biermann, A. Poteryaev, A. I. Lichtenstein, and A. Georges. Dynamical Singlets and Correlation-Assisted Peierls Transition in ${\mathrm{V}\mathrm{O}}_{2}$. *Physical Review Letters*, 94(2):026404, January 2005.

[201] T. A. Maier and D. J. Scalapino. Pairing interaction near a nematic quantum critical point of a three-band ${\mathrm{CuO}}_{2}$ model. *Physical Review B*, 90(17):174510, November 2014.

[202] P. R. C. Kent, T. Saha-Dasgupta, O. Jepsen, O. K. Andersen, A. Macridin, T. A. Maier, M. Jarrell, and T. C. Schulthess. Combined density functional and dynamical cluster quantum Monte Carlo calculations of the three-band Hubbard model for hole-doped cuprate superconductors. *Physical Review B*, 78(3):035132, July 2008.

[203] Kristjan Haule. Exact Double Counting in Combining the Dynamical Mean Field Theory and the Density Functional Theory. *Physical Review Letters*, 115(19):196403, November 2015.

[204] M. Burkatzki, C. Filippi, and M. Dolg. Energy-consistent pseudopotentials for quantum Monte Carlo calculations. *The Journal of Chemical Physics*, 126(23):234105, June 2007.

[205] M. Burkatzki, Claudia Filippi, and M. Dolg. Energy-consistent small-core pseudopotentials for 3d-transition metals adapted to quantum Monte Carlo calculations. *The Journal of Chemical Physics*, 129(16):164115, October 2008.

[206] Katharina Doblhoff-Dier, Jrg Meyer, Philip E. Hoggan, Geert-Jan Kroes, and Lucas K. Wagner. Diffusion Monte Carlo for Accurate Dissociation Energies of 3d Transition Metal Containing Molecules. *Journal of Chemical Theory and Computation*, 12(6):2583–2597, June 2016.

[207] M. Chandler Bennett, Cody A. Melton, Abdulgani Annaberdiyev, Guangming Wang, Luke Shulenburger, and Lubos Mitas. A new generation of effective core potentials for correlated calculations. *The Journal of Chemical Physics*, 147(22):224106, December 2017.

[208] Lubo Mit, Eric L. Shirley, and David M. Ceperley. Nonlocal pseudopotentials and diffusion Monte Carlo. *The Journal of Chemical Physics*, 95(5):3467–3475, September 1991.

[209] Michele Casula. Beyond the locality approximation in the standard diffusion Monte Carlo method. *Physical Review B*, 74(16):161102, October 2006.

[210] Huihuo Zheng, Hitesh J. Changlani, Kiel T. Williams, Brian Busemeyer, and Lucas K. Wagner. From Real Materials to Model Hamiltonians With Density Matrix Downfolding. *Frontiers in Physics*, 6, 2018.

[211] M. Springer and F. Aryasetiawan. Frequency-dependent screened interaction in Ni within the random-phase approximation. *Physical Review B*, 57(8):4364–4368, February 1998.

[212] Steven R. White. Numerical canonical transformation approach to quantum many-body problems. *The Journal of Chemical Physics*, 117(16):7472–7482, October 2002.

[213] Takeshi Yanai and Garnet Kin-Lic Chan. Canonical transformation theory for multireference problems. *The Journal of Chemical Physics*, 124(19):194106, May 2006.

[214] Eric Neuscamman, Takeshi Yanai, and Garnet Kin-Lic Chan. A review of canonical transformation theory. *International Reviews in Physical Chemistry*, 29(2):231–271, April 2010.

[215] Thomas J. Watson and Garnet Kin-Lic Chan. Correct Quantum Chemistry in a Minimal Basis from Effective Hamiltonians. *Journal of Chemical Theory and Computation*, 12(2):512–522, February 2016.

[216] F. Aryasetiawan, M. Imada, A. Georges, G. Kotliar, S. Biermann, and A. I. Lichtenstein. Frequency-dependent local interactions and low-energy effective models from electronic structure calculations. *Physical Review B*, 70(19):195104, November 2004.

[217] M. Karolak, G. Ulm, T. Wehling, V. Mazurenko, A. Poteryaev, and A. Lichtenstein. Double counting in LDA+DMFTThe example of NiO. *Journal of Electron Spectroscopy and Related Phenomena*, 181(1):11–15, July 2010.

[218] I. A. Nekrasov, N. S. Pavlov, and M. V. Sadovskii. Consistent LDA + DMFT approach to the electronic structure of transition metal oxides: Charge transfer insulators and correlated metals. *Journal of Experimental and Theoretical Physics*, 116(4):620–634, April 2013.

[219] Carsten Honerkamp, Hiroshi Shinaoka, Fakher F. Assaad, and Philipp Werner. Limitations of constrained random phase approximation downfolding. *Physical Review B*, 98(23):235151, December 2018.

[220] Qiang Han, B. Chakrabarti, and K. Haule. Investigation into the inadequacy of cRPA in reproducing screening in strongly correlated systems. October 2018.

[221] Christian Heumann, Michael Schomaker, and Shalabh. Goodness of Fit. In *Introduction to Statistics and Data Analysis*, pages 256–259. Springer International Publishing Switzerland, 2016.

[222] Herv Abdi and Lynne J. Williams. Principal component analysis. *Wiley Interdisciplinary Reviews: Computational Statistics*, 2(4):433–459, 2010.

[223] Robert Tibshirani. Regression Shrinkage and Selection Via the Lasso. *Journal of the Royal Statistical Society, Series B*, 58:267–288, 1994.

[224] Arthur E. Hoerl and Robert W. Kennard. Ridge Regression: Biased Estimation for Nonorthogonal Problems. *Technometrics*, 42(1):80–86, February 2000.

[225] S. G. Mallat and Zhifeng Zhang. Matching pursuits with time-frequency dictionaries. *IEEE Transactions on Signal Processing*, 41(12):3397–3415, December 1993.

[226] B. Efron. Bootstrap Methods: Another Look at the Jackknife. *The Annals of Statistics*, 7(1):1–26, January 1979.

[227] David MacKay. Minimum description length (MDL). In *Information Theory, Inference, and Learning Algorithms*, page 353. Cambridge University Press, 7.2 edition, 2005.

[228] R. N. Barnett, P. J. Reynolds, and W. A. Lester Jr. H + H2 reaction barrier: A fixednode quantum Monte Carlo study. *The Journal of Chemical Physics*, 82(6):2700–2707, March 1985.

[229] P. J. Reynolds, R. N. Barnett, B. L. Hammond, and W. A. Lester. Molecular physics and chemistry applications of quantum Monte Carlo. *Journal of Statistical Physics*, 43(5-6):1017–1026, 1986.

[230] James B. Anderson. Note: Exact quantum Monte Carlo calculations of the barrier for the H + H2 reaction at the sub-microhartree level. *The Journal of Chemical Physics*, 144(16):166101, April 2016.

[231] Jeffrey C. Grossman and Lubos Mitas. High Accuracy Molecular Heats of Formation and Reaction Barriers: Essential Role of Electron Correlation. *Physical Review Letters*, 79(22):4353–4356, December 1997.

[232] A. C. Kollias, O. Couronne, and W. A. Lester Jr. Quantum Monte Carlo study of the reaction: Cl+CH3ohCH2oh+HCl. *The Journal of Chemical Physics*, 121(3):1357–1363, July 2004.

[233] Matteo Barborini and Leonardo Guidoni. Reaction pathways by quantum Monte Carlo: Insight on the torsion barrier of 1,3-butadiene, and the conrotatory ring opening of cyclobutene. *The Journal of Chemical Physics*, 137(22):224309, December 2012.

[234] Francesco Fracchia, Claudia Filippi, and Claudio Amovilli. Multi-level quantum monte Carlo wave functions for complex reactions: The decomposition of -hydroxy-dimethylnitrosamine. *Journal of Computational Chemistry*, 35(1):30–38, January 2014.

[235] Srimanta Pakhira, Benjamin S. Lengeling, Olayinka Olatunji-Ojo, Michel Caffarel, Michael Frenklach, and William A. Lester. A Quantum Monte Carlo Study of the Reactions of CH with Acrolein. *The Journal of Physical Chemistry A*, 119(18):4214–4223, May 2015.

[236] Yosuke Kanai and Noboru Takeuchi. Toward accurate reaction energetics for molecular line growth at surface: Quantum Monte Carlo and density functional theory calculations. *The Journal of Chemical Physics*, 131(21):214708, December 2009.

[237] Philip E. Hoggan and Ahmed Boufergune. Quantum Monte Carlo for activated reactions at solid surfaces: Time well spent on stretched bonds. *International Journal of Quantum Chemistry*, 114(17):1150–1156, September 2014.

[238] Shih-I. Lu. Theoretical study of transition state structure and reaction enthalpy of the F+H2HF+H reaction by a diffusion quantum Monte Carlo approach. *The Journal of Chemical Physics*, 122(19):194323, May 2005.

[239] Francesco Fracchia, Claudia Filippi, and Claudio Amovilli. Barrier Heights in Quantum Monte Carlo with Linear-Scaling Generalized-Valence-Bond Wave Functions. *Journal of Chemical Theory and Computation*, 9(8):3453–3462, August 2013.

[240] Xiaojun Zhou and Fan Wang. Barrier heights of hydrogen-transfer reactions with diffusion quantum monte carlo method. *Journal of Computational Chemistry*, 38(11):798–806, April 2017.

[241] Jingjing Zheng, Yan Zhao, and Donald G. Truhlar. The DBH24/08 Database and Its Use to Assess Electronic Structure Model Chemistries for Chemical Reaction Barrier Heights. *Journal of Chemical Theory and Computation*, 5(4):808–821, April 2009.

[242] Francesco Fracchia, Renzo Cimiraglia, and Celestino Angeli. Assessment of Multireference Perturbation Methods for Chemical Reaction Barrier Heights. *The Journal of Physical Chemistry A*, 119(21):5490–5495, May 2015.

[243] Roberto Dovesi, Alessandro Erba, Roberto Orlando, Claudio M. ZicovichWilson, Bartolomeo Civalleri, Lorenzo Maschio, Michel Rrat, Silvia Casassa, Jacopo Baima, Simone Salustro, and Bernard Kirtman. Quantum-mechanical condensed matter simulations with CRYSTAL. *Wiley Interdisciplinary Reviews: Computational Molecular Science*, 8(4):e1360, July 2018.

[244] R. Nazarov, L. Shulenburger, M. Morales, and Randolph Q. Hood. Benchmarking the pseudopotential and fixed-node approximations in diffusion Monte Carlo calculations of molecules and solids. *Physical Review B*, 93(9):094111, March 2016.

[245] Kevin M. Rasch, Shuming Hu, and Lubos Mitas. Communication: Fixed-node errors in quantum Monte Carlo: Interplay of electron density and node nonlinearities. *The Journal of Chemical Physics*, 140(4):041102, January 2014.

[246] J. M. Chambers. *Graphical Methods for Data Analysis*. Chapman and Hall/CRC, 1 edition, 1983.

[247] Ying Zhang, Xin Xu, and William A. Goddard. Doubly hybrid density functional for accurate descriptions of nonbond interactions, thermochemistry, and thermochemical kinetics. *Proceedings of the National Academy of Sciences*, 106(13):4963–4968, March 2009.

[248] Michael R. Norman. Trend: High-temperature superconductivity in the iron pnictides. *Physics*, 1, September 2008.

[249] Luca de Medici, Gianluca Giovannetti, and Massimo Capone. Selective Mott Physics as a Key to Iron Superconductors. *Physical Review Letters*, 112(17):177001, April 2014.

[250] D. J. Scalapino. A common thread: The pairing interaction for unconventional superconductors. *Reviews of Modern Physics*, 84(4):1383–1417, October 2012.

[251] Jinsheng Wen, Guangyong Xu, Genda Gu, J. M. Tranquada, and R. J. Birgeneau. Interplay between magnetism and superconductivity in iron-chalcogenide superconductors: crystal growth and characterizations. *Reports on Progress in Physics*, 74(12):124503, 2011.

[252] Pengcheng Dai. Antiferromagnetic order and spin dynamics in iron-based superconductors. *Reviews of Modern Physics*, 87(3):855–896, August 2015.

[253] Pengcheng Dai, Jiangping Hu, and Elbio Dagotto. Magnetism and its microscopic origin in iron-based high-temperature superconductors. *Nature Physics*, 8(10):709–718, October 2012.

[254] T. Imai, K. Ahilan, F. L. Ning, T. M. McQueen, and R. J. Cava. Why Does Undoped FeSe Become a High-${T}_{c}$ Superconductor under Pressure? *Physical Review Letters*, 102(17):177005, April 2009.

[255] Yoshikazu Mizuguchi, Fumiaki Tomioka, Shunsuke Tsuda, Takahide Yamaguchi, and Yoshihiko Takano. Superconductivity at 27k in tetragonal FeSe under high pressure. *Applied Physics Letters*, 93(15):152505, October 2008.

[256] S. Medvedev, T. M. McQueen, I. A. Troyan, T. Palasyuk, M. I. Eremets, R. J. Cava, S. Naghavi, F. Casper, V. Ksenofontov, G. Wortmann, and C. Felser. Electronic and magnetic phase diagram of -$Fe_{1.01}Se$ with superconductivity at 36.7 K under pressure. *Nature Materials*, 8(8):630–633, August 2009.

[257] M. Bendele, A. Amato, K. Conder, M. Elender, H. Keller, H.-H. Klauss, H. Luetkens, E. Pomjakushina, A. Raselli, and R. Khasanov. Pressure Induced Static Magnetic Order in Superconducting ${\mathrm{FeSe}}_{1-x}$. *Physical Review Letters*, 104(8):087003, February 2010.

[258] M. C. Rahn, R. A. Ewings, S. J. Sedlmaier, S. J. Clarke, and A. T. Boothroyd. Strong $(\pi,0)$ spin fluctuations in β-FeSe observed by neutron spectroscopy. *Physical Review B*, 91(18), May 2015. arXiv: 1502.03838.

[259] J. Maletz, V. B. Zabolotnyy, D. V. Evtushinsky, S. Thirupathaiah, A. U. B. Wolter, L. Harnagea, A. N. Yaresko, A. N. Vasiliev, D. A. Chareev, A. E. Bhmer, F. Hardy, T. Wolf, C. Meingast, E. D. L. Rienks, B. Bchner, and S. V. Borisenko. Unusual band renormalization in the simplest iron-based superconductor ${\text{FeSe}}_{1\ensuremath{-}x}$. *Physical Review B*, 89(22):220506, June 2014.

[260] Alain Audouard, Fabienne Duc, Loc Drigo, Pierre Toulemonde, Sandra Karlsson, Pierre Strobel, and Andr Sulpice. Quantum oscillations and upper critical magnetic field of the iron-based superconductor FeSe. *EPL (Europhysics Letters)*, 109(2):27003, January 2015.

[261] Federico Caglieris, Fabio Ricci, Gianrico Lamura, Albert Martinelli, A. Palenzona, Ilaria Pallecchi, Alberto Sala, Gianni Profeta, and Marina Putti. Theoretical and experimental investigation of magnetotransport in iron chalcogenides. *Science and Technology of Advanced Materials*, 13(5):054402, October 2012.

[262] Ansgar Liebsch and Hiroshi Ishida. Correlation-induced spin freezing transition in FeSe: A dynamical mean field study. *Physical Review B*, 82(15):155106, October 2010.

[263] Z. P. Yin, K. Haule, and G. Kotliar. Magnetism and charge dynamics in iron pnictides. *Nature Physics*, 7(4):294–297, April 2011.

[264] L. Craco and S. Leoni. Comparative study of tetragonal and hexagonal FeSe: An orbital-selective scenario. *EPL (Europhysics Letters)*, 92(6):67003, December 2010.

[265] L. Craco, M. S. Laad, and S. Leoni. Normal-state correlated electronic structure of tetragonal FeSe superconductor. *Journal of Physics: Conference Series*, 487:012017, March 2014.

[266] I. Leonov, S.L. Skornyakov, V.I. Anisimov, and D. Vollhardt. Correlation-Driven Topological Fermi Surface Transition in FeSe. *Physical Review Letters*, 115(10):106402, September 2015.

[267] L. De'Medici. Hund's coupling and its key role in tuning multiorbital correlations. *Physical Review B - Condensed Matter and Materials Physics*, 83(20), 2011.

[268] Luca de Medici, Jernej Mravlje, and Antoine Georges. Janus-Faced Influence of Hund's Rule Coupling in Strongly Correlated Materials. *Physical Review Letters*, 107(25):256401, December 2011.

[269] Antoine Georges, Luca de' Medici, and Jernej Mravlje. Strong electronic correlations from Hund's coupling. *Annual Review of Condensed Matter Physics*, 4(1):137–178, April 2013. arXiv: 1207.3033.

[270] T. Tzen Ong and Piers Coleman. Local Quantum Criticality of an Iron-Pnictide Tetrahedron. *Physical Review Letters*, 108(10):107201, March 2012.

[271] Nicola Lanat, Hugo U. R. Strand, Gianluca Giovannetti, Bo Hellsing, Luca de' Medici, and Massimo Capone. Orbital selectivity in Hund's metals: The iron chalcogenides. *Physical Review B*, 87(4):045122, January 2013.

[272] Z. P. Yin, K. Haule, and G. Kotliar. Kinetic frustration and the nature of the magnetic and paramagnetic states in iron pnictides and iron chalcogenides. *Nature Materials*, 10(12):932–935, December 2011.

[273] Motoaki Hirayama, Takashi Miyake, and Masatoshi Imada. Derivation of static low-energy effective models by an \textit{ab initio} downfolding method without double counting of Coulomb correlations: Application to SrVO${}_{3}$, FeSe, and FeTe. *Physical Review B*, 87(19):195144, May 2013.

[274] Motoaki Hirayama, Takahiro Misawa, Takashi Miyake, and Masatoshi Imada. Ab initio Studies of Magnetism in the Iron Chalcogenides FeTe and FeSe. *Journal of the Physical Society of Japan*, 84(9):093703, August 2015.

[275] Jindich Koloren, Shuming Hu, and Lubos Mitas. Wave functions for quantum Monte Carlo calculations in solids: Orbitals from density functional theory with hybrid exchange-correlation functionals. *Physical Review B*, 82(11):115108, September 2010.

[276] people.sissa.it/~sorella.

[277] Sandro Sorella and Luca Capriotti. Algorithmic differentiation and the calculation of forces by quantum Monte Carlo. *The Journal of Chemical Physics*, 133(23):234111, December 2010.

[278] C. Lin, F. H. Zong, and D. M. Ceperley. Twist-averaged boundary conditions in continuum quantum Monte Carlo algorithms. *Physical Review E*, 64(1):016702, June 2001.

[279] Hai-Yuan Cao, Shiyou Chen, Hongjun Xiang, and Xin-Gao Gong. Antiferromagnetic ground state with pair-checkerboard order in FeSe. *Physical Review B*, 91(2):020504, January 2015.

[280] J. K. Glasbrenner, I. I. Mazin, Harald O. Jeschke, P. J. Hirschfeld, R. M. Fernandes, and Roser Valent. Effect of magnetic frustration on nematicity and superconductivity in iron chalcogenides. *Nature Physics*, 11(11):953–958, November 2015.

[281] Cesare Tresca, Fabio Ricci, and Gianni Profeta. Strain effects in monolayer iron-chalcogenide superconductors. *2D Materials*, 2(1):015001, December 2014.

[282] Despina Louca, K. Horigane, A. Llobet, R. Arita, S. Ji, N. Katayama, S. Konbu, K. Nakamura, T.-Y. Koo, P. Tong, and K. Yamada. Local atomic structure of superconducting ${\text{FeSe}}_{1\ensuremath{-}x}{\text{Te}}_{x}$. *Physical Review B*, 81(13):134524, April 2010.

[283] Anouar Benali, Luke Shulenburger, Nichols A. Romero, Jeongnim Kim, and O. Anatole von Lilienfeld. Application of Diffusion Monte Carlo to Materials Dominated by van der Waals Interactions. *Journal of Chemical Theory and Computation*, 10(8):3417–3422, August 2014.

[284] Sandro Sorella, Michele Casula, and Dario Rocca. Weak binding between two aromatic rings: Feeling the van der Waals attraction by quantum Monte Carlo methods. *The Journal of Chemical Physics*, 127(1):014105, July 2007.

[285] H. Okabe, N. Takeshita, K. Horigane, T. Muranaka, and J. Akimitsu. Pressure-induced high-${T}_{c}$ superconducting phase in FeSe: Correlation between anion height and ${T}_{c}$. *Physical Review B*, 81(20):205119, May 2010.

[286] H. Anton and P. C. Schmidt. Theoretical investigations of the elastic constants in Laves phases. *Intermetallics*, 5(6):449–465, 1997.

[287] Johannes Lischner, Timur Bazhirov, Allan H. MacDonald, Marvin L. Cohen, and Steven G. Louie. First-principles theory of electron-spin fluctuation coupling and superconducting instabilities in iron selenide. *Physical Review B*, 91(2):020502, January 2015.

[288] Y. Han, W. Y. Li, L. X. Cao, X. Y. Wang, B. Xu, B. R. Zhao, Y. Q. Guo, and J. L. Yang. Superconductivity in Iron Telluride Thin Films under Tensile Stress. *Physical Review Letters*, 104(1):017003, January 2010.

[289] M. Casula and S. Sorella. Improper s-wave symmetry of the electronic pairing in iron-based superconductors by first-principles calculations. *Physical Review B*, 88(15):155125, October 2013.

[290] Y. Wang, T. Berlijn, P.J. Hirschfeld, D.J. Scalapino, and T.A. Maier. Glide-Plane Symmetry and Superconducting Gap Structure of Iron-Based Superconductors. *Physical Review Letters*, 114(10):107002, March 2015.

[291] Hendra Kwee, Shiwei Zhang, and Henry Krakauer. Finite-Size Correction in Many-Body Electronic Structure Calculations. *Physical Review Letters*, 100(12):126404, March 2008.

[292] Sandro Sorella, Michele Casula, Leonardo Spanu, and Andrea Dal Corso. Ab initio calculations for the $\ensuremath{\beta}$-tin diamond transition in silicon: Comparing theories with experiments. *Physical Review B*, 83(7):075119, February 2011.

[293] Gerald Knizia. Intrinsic Atomic Orbitals: An Unbiased Bridge between Quantum Theory and Chemical Concepts. *Journal of Chemical Theory and Computation*, 9(11):4834–4843, November 2013.

[294] Paolo G. Radaelli. Orbital ordering in transition-metal spinels. *New Journal of Physics*, 7(1):53, 2005.

[295] S.-H. Lee, H. Takagi, D. Louca, M. Matsuda, S. Ji, H. Ueda, Y. Ueda, T. Katsufuji, J.-H. Chung, S. Park, S.-W. Cheong, and C. Broholm. Frustrated magnetism and cooperative phase transitions in spinels. *Journal of the Physical Society of Japan*, 79(1), 2010.

[296] M. Schmidt, W. Ratcliff, P. G. Radaelli, K. Refson, N. M. Harrison, and S. W. Cheong. Spin Singlet Formation in ${\mathrm{M}\mathrm{g}\mathrm{T}\mathrm{i}}_{2}{\mathrm{O}}_{4}$: Evidence of a Helical Dimerization Pattern. *Physical Review Letters*, 92(5):056402, February 2004.

[297] Masahiko Isobe and Yutaka Ueda. Observation of Phase Transition from Metal to Spin-Singlet Insulator in MgTi2o4 with S=1/2 Pyrochlore Lattice. *Journal of the Physical Society of Japan*, 71(8):1848–1851, August 2002.

[298] J. Zhou, G. Li, J. L. Luo, Y. C. Ma, Dan Wu, B. P. Zhu, Z. Tang, J. Shi, and N. L. Wang. Optical study of ${\mathrm{MgTi}}_{2}{\mathrm{O}}_{4}$: Evidence for an orbital-Peierls state. *Physical Review B*, 74(24):245102, December 2006.

[299] Haowei He, A. X. Gray, P. Granitzka, J. W. Jeong, N. P. Aetukuri, R. Kukreja, Lin Miao, S. Alexander Breitweiser, Jinpeng Wu, Y. B. Huang, P. Olalde-Velasco, J. Pelliciari, W. F. Schlotter, E. Arenholz, T. Schmitt, M. G. Samant, S. S. P. Parkin, H. A. Drr, and L. Andrew Wray. Measurement of collective excitations in ${\text{VO}}_{2}$ by resonant inelastic x-ray scattering. *Physical Review B*, 94(16):161119, October 2016.

[300] P. Reinhardt, M. P. Habas, R. Dovesi, I. de P. R. Moreira, and F. Illas. Magnetic coupling in the weak ferromagnet ${\mathrm{CuF}}_{2}$. *Physical Review B*, 59(2):1016–1023, January 1999.

[301] Coen de Graaf and Francesc Illas. Electronic structure and magnetic interactions of the spin-chain compounds ${\mathrm{Ca}}_{2}{\mathrm{CuO}}_{3}$ and ${\mathrm{Sr}}_{2}{\mathrm{CuO}}_{3}$. *Physical Review B*, 63(1):014404, December 2000.

[302] Fengjie Ma, Zhong-Yi Lu, and Tao Xiang. Arsenic-bridged antiferromagnetic superexchange interactions in LaFeAsO. *Physical Review B*, 78(22):224517, December 2008.

[303] I. I. Mazin, M. D. Johannes, L. Boeri, K. Koepernik, and D. J. Singh. Problems with reconciling density functional theory calculations with experiment in ferropnictides. *Physical Review B*, 78(8):085104, August 2008.

[304] Hosung Seo, Agham Posadas, and Alexander A. Demkov. Strain-driven spin-state transition and superexchange interaction in LaCoO${}_{3}$: Ab initio study. *Physical Review B*, 86(1):014430, July 2012.

[305] R. J. Needs, M. D. Towler, N. D. Drummond, and P. Lpez Ros. Continuum variational and diffusion quantum Monte Carlo calculations. *Journal of Physics: Condensed Matter*, 22(2):023201, 2010.

[306] Luke Shulenburger and Thomas R. Mattsson. Quantum Monte Carlo applied to solids. *Physical Review B*, 88(24):245117, December 2013.

[307] Brian Busemeyer, Mario Dagrada, Sandro Sorella, Michele Casula, and Lucas K. Wagner. Competing collinear magnetic structures in superconducting FeSe by first-principles quantum Monte Carlo calculations. *Physical Review B*, 94(3):035108, July 2016.

[308] Sandro Sorella. Green Function Monte Carlo with Stochastic Reconfiguration. *Physical Review Letters*, 80(20):4558–4561, May 1998.

[309] Michele Casula, Claudio Attaccalite, and Sandro Sorella. Correlated geminal wave function for molecules:An efficient resonating valence bond approach. *The Journal of Chemical Physics*, 121(15):7110–7126, October 2004.